Experimental and Computational Study of the Aerodynamic Performance of a Formula Student Vehicle

Diogo Casaleiro Vitoriano dos Santos

Thesis to obtain the Master of Science Degree in

Aerospace Engineering

Supervisors: Prof. André Calado Marta
Prof. Luís Rego da Cunha Eça

Examination Committee

Chairperson: Prof. Filipe Szolnoky Ramos Pinto Cunha
Supervisor: Prof. André Calado Marta
Member of the Committee: Prof. José Manuel Da Silva Chaves Ribeiro Pereira

December 2025

Dedicated to my mother Mónica, father Pedro, siblings Mariana, Rita and Pedro, and girlfriend Leonor.

Declaration

I declare that this document is an original work of my own authorship and that it fulfills all the requirements of the Code of Conduct and Good Practices of the Universidade de Lisboa.

Acknowledgments

First and foremost, I would like to express my deepest gratitude to my supervisors, Professor André Marta and Professor Luís Eça, for their invaluable guidance, continuous support, and insightful feedback throughout this work. Their expertise and encouragement were fundamental to the successful completion of this thesis and to my development as an engineer.

I would also like to thank the FST Lisboa Formula Student team for providing the resources essential to this project and for their support during the assembly of the scaled model. In particular, I am grateful to the members of the aerodynamics department: Guilherme Soares, Guilherme Henriques, Rafael Cunha, Vítor Clara, Diogo Marques, and João Rodrigues, for their enthusiasm, teamwork, and commitment throughout this process, as well as for always making me feel slightly older.

My sincere appreciation goes to LNEC for granting access to their facilities, particularly the aeronautical wind tunnel. I am especially thankful to Fernando Oliveira and Susana Almeida for their patience, constant availability, and technical support, as well as to my fellow researchers Lucas Lopes and Francisco Vaz for their help and collaboration throughout the hard months of the experimental campaign.

I am also grateful to iStartLab for allowing the use of their 3D printing equipment over several months. A special thanks to Ricardo Febra and Pedro Monteiro for their valuable advice and continuous assistance in all aspects related to additive manufacturing.

To the IST football team, Técnico Futebol Clube, thank you for providing moments of distraction, camaraderie, and competition that helped balance the demanding months of this work.

To my closest friends, the Mati group: João Imaginário, Pedro Caçador, Duarte Ghira, João Santos, and Guilherme Costa, thank you for your friendship, joy, and constant support, always giving me something to smile about.

Finally, my deepest gratitude goes to my family: my mother, Mónica Casaleiro; my father, Pedro Santos; my sisters, Mariana and Rita Santos; my brother, Pedro Santos; and my girlfriend, Leonor Carvalho. Your love, patience, and unwavering support have been the foundation of everything I have accomplished. This work would not have been possible without you.

Resumo

Este trabalho apresenta o estudo aerodinâmico do FST14, o mais recente protótipo *Formula Student* desenvolvido pela FST Lisboa, com foco nos seus elementos aerodinâmicos laterais. O estudo teve como objetivo não só melhorar o desempenho aerodinâmico do veículo, mas também avaliar e consolidar a metodologia numérica utilizada no processo de conceção da equipa.

Foi estabelecido um modelo numérico de mecânica dos fluidos computacional (MFC), incluindo estudos de convergência de malha, estimativa de erro numérico e uma avaliação dos efeitos de bloqueamento, escala, movimento das rodas e do solo, e variações da altura ao solo nos resultados numéricos. A análise centrou-se em três configurações dos elementos laterais, com o objetivo de identificar a mais eficiente em termos aerodinâmicos e de contributo para o desempenho global do veículo.

Para avaliar a fiabilidade das simulações numéricas, foi concebido, fabricado e testado no túnel de vento de circuito fechado do LNEC um modelo à escala 1:3 do FST14. A balança aerodinâmica foi recalibrada, assegurando a medição de forças e momentos globais em simultâneo com a aquisição de pressões estáticas e a visualização do escoamento com fios de lã. Apesar das incertezas, os resultados experimentais revelaram tendências consistentes e boa concordância com os dados numéricos, reforçando a confiança na metodologia MFC.

Por fim, o modelo numérico foi estendido para reproduzir condições reais em pista, permitindo avaliar o comportamento aerodinâmico para além das limitações do túnel de vento. As condições de fronteira alteraram a hierarquia de desempenho entre configurações, afetando sustentação, arrasto e contribuição dos elementos laterais, conduzindo à seleção da configuração ótima para integração no protótipo FST14 em condições reais de operação.

Palavras-chave: Conceção Aerodinâmica, Validação, Mecânica dos Fluidos Computacional, Ensaios em Túnel de Vento, Aerodinâmica de Veículos de Competição, Formula Student.

Abstract

This work presents the aerodynamic study of the FST14, the latest Formula Student prototype developed by FST Lisboa, focusing on its side elements. The study aimed not only to improve the vehicle's aerodynamic performance but also to evaluate and consolidate the numerical methodology used in the team's design process.

A comprehensive computational fluid dynamics (CFD) framework was established, including mesh convergence studies, numerical error estimation, and a systematic assessment of the isolated effects of blockage, scaling, wheel and ground motion, and ground clearance variations on the numerical results. The analysis focused on three side element configurations to identify the most effective design in terms of aerodynamic efficiency and overall contribution to vehicle performance.

To evaluate the reliability of the numerical predictions, a 1:3 scale model of the FST14 was designed, manufactured, and tested in the closed circuit wind tunnel at LNEC. The aerodynamic force balance was recalibrated, enabling measurement of global forces and moments together with surface static pressures and flow visualization using wool tufts. Despite measurement uncertainties, the experimental results demonstrated consistent aerodynamic trends and agreement with the numerical data, reinforcing confidence in the CFD methodology.

Finally, the numerical framework was extended to replicate on-track conditions, enabling assessment of aerodynamic behavior beyond wind tunnel constraints. The modified boundary conditions altered the performance hierarchy among configurations, affecting downforce, drag, and side element contribution. These findings redefined the observed aerodynamic trends and guided the selection of the optimal configuration for integration into the FST14 prototype under real-world conditions.

Keywords: Aerodynamic Design, Experimental Validation, Computational Fluid Dynamics, Wind Tunnel Testing, Race Car Aerodynamics, Formula Student.

Contents

List of Tables

List of Figures

Nomenclature

Greek symbols

α	Angle of attack
β	Slip angle
δ	Boundary layer thickness
δ^*	Displacement thickness
Γ	Vortex intensity
μ	Dynamic viscosity
ϕ	Roll angle
ψ	Yaw angle
ρ	Density
τ_w	Wall shear stress
θ	Momentum thickness

Roman symbols

A	Reference area
AR	Aspect ratio
C	Sutherland's constant
c	Reference chord length
C_D	Coefficient of drag
C_L	Coefficient of lift
C_p	Coefficient of static pressure
C_f	Coefficient of skin friction
C_M	Coefficient of moment

C_{p_T}	Coefficient of total pressure
e	Efficiency factor
F	Aerodynamic force component
H	Boundary layer shape factor
L	Specific length
M	Aerodynamic moment component
p	Static pressure
q	Dynamic pressure
R	Specific gas constant
Re	Reynolds number
T	Temperature
TI	Turbulence intensity
U_∞	Free stream velocity
V	Velocity magnitude
w	Width

Subscripts

∞	Free stream condition
ref	Reference condition
t	Turbulent
target	Target condition for wind tunnel operation
x, y, z	Cartesian components

Superscripts

+	Non-dimensional in wall units
T	Transpose

Glossary

AoA	Angle of Attack
BC	Boundary Conditions
BH	Bullhorns
BSL	Baseline
CAD	Computer Aided Design
CF	Carbon Fiber
CFD	Computational Fluid Dynamics
CFL	Courant-Friedrichs-Lewy
CG	Center of Gravity
CoP	Center of Pressure
CPU	Central Processing Unit
CV	Combustion Vehicle
DAQ	Data Acquisition System
DES	Dettached Eddy Simulation
DF	Downforce
DNS	Direct Numerical Simulation
DRS	Drag Reduction System
DV	Driverless Vehicle
EFD	Experimental Fluid Dynamics
ESP	Electronic Scan Pressure
EV	Eletric Vehicle
F1	Formula 1
FS	Formula Student
FSG	Formula Student Germany
FST	Formula Student Técnico
FW	Front Wing
IST	Instituto Superior Técnico
LES	Large Eddy Simulation
LNEC	Laboratório Nacional de Engenharia Civil
LTO	Laboratório de Técnicas Oficinais

MFC	Mecanica dos Fluidos Computacional
NI	National Instruments
NS	Navier-Stokes
PAHT	Polyamide High-Temperature
PETG	Polyethylene Terephthalate Glycol
PLA	Polylactic Acid
RAM	Random Access Memory
RANS	Reynolds Averaged Navier-Stokes
RW	Rear Wing
SAE	Society of Automotive Engineers
SSL	Standard Sea Level
SST	Shear Stress Transport
VFD	Variable Frequency Drive
VG	Vortex Generator
WT	Wind Tunnel

Chapter 1

Introduction

This chapter provides an overview of the thesis by outlining the motivation behind the work, the context of the Formula Student competition, and the objectives and expected deliverables. Additionally, the thesis structure is presented to guide the reader through the subsequent chapters.

1.1 Motivation

Aerodynamics is a crucial factor in modern motorsports, where improving vehicle performance demands a careful balance between downforce and drag, as well as an even distribution of aerodynamic forces across the vehicle, particularly between the front and rear axles, to ensure optimal handling and stability at varying speeds. This is particularly true for Formula Student (FS) cars, which are open-wheel, single-seater vehicles designed and built by university teams to compete in international engineering competitions, as displayed in Figure 1.1. Unlike closed-wheel race cars, open-wheel vehicles have exposed tires and typically feature complex aerodynamic appendages, such as front and rear wings, diffusers, and side elements, that must work harmoniously to maximize performance.

Figure 1.1: FST13 competing at Formula Student Portugal 2024.

FS cars, operating at low Reynolds numbers, combined with their open wheel configuration, pose unique aerodynamic challenges. The exposed wheels generate significant turbulence and overall complex flow field phenomena that are difficult to predict using computational fluid dynamics (CFD) alone.

Despite recent advances in CFD, such simulations struggle to accurately capture these complex flow phenomena, particularly in scenarios involving separated flow, high turbulence, and high vorticity. Therefore, wind tunnel testing remains a crucial validation tool for refining numerical setups. Wind tunnel testing enables the analysis of the vehicle's aerodynamic performance by replicating on-track conditions as closely as possible within a controlled environment. However, the modeling accuracy of these tests depends on critical factors, such as whether the ground plane is moving or fixed, whether the wheels are rotating or stationary, and flow similarity.

This work is motivated by the desire to enhance the aerodynamics of the Formula Student Técnico (FST) vehicle using both numerical simulations and wind tunnel testing. A critical aspect of this thesis is the development of a 1:3 scale model of the FST vehicle to allow for affordable yet valuable experimentation. The focus will be on studying the side aerodynamic elements, which play a vital role in the vehicle's overall aerodynamic efficiency. Ultimately, this work aims to bridge the gap between numerical CFD simulations and real world aerodynamic performance. The approach adopted not only addresses the inherent limitations of CFD estimations but also seeks to quantify the effects of geometry scaling and changes in boundary conditions.

1.2 Formula Student

Formula Student is a global competition where university students design and build single seater, open wheel race cars. The competition comprises static events, that evaluate theoretical and business aspects, and dynamic events, that assess on-track performance [1].

Advanced aero packages, featuring multiple element wings, diffusers, and flow directing devices, are increasingly important. However, the constraints imposed by the regulations in [2] define the design envelopes shown in Figure 1.2, which limit wingspans and often lead to low aspect ratio wings.

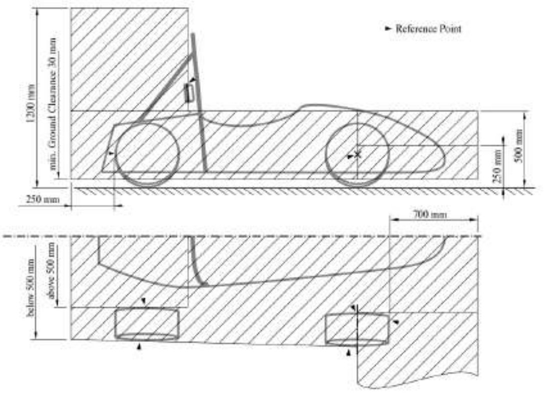

Figure 1.2: Maximum dimensions and positioning of aerodynamic devices [2].

Wordley and Saunders [3] showed that, even at low speeds, downforce improves traction and lowers lap times in autocross and endurance. Aerodynamics also aids performance in the skidpad by enhancing lateral grip. However, in the acceleration event, a low-drag setup with a drag reduction system (DRS) can be advantageous, even though traction continues to play an important role. Aerodynamics also contributes to the design event score, where justification and validation play a key role.

Over the years, several master's thesis have been completed within the Técnico's Formula Student team, particularly in aerodynamics. The earliest relevant work, chronologically, is that of Oliveira [4], which focused on the development of an aerodynamic force balance for wind tunnel testing, following the design methodology established by Ferreira [5]. This balance was designed and equipped with strain gauges and sensors to measure forces, moments, and environmental variables such as speed and temperature. A user friendly interface for real time data visualization was also implemented. To ensure accuracy, a static calibration was performed by applying known loads and using a least squares fitting method to generate a calibration matrix. The effectiveness of the balance was demonstrated through experimental testing on a rear wing model of a racing car. The endplates employed on the tested rear wing were designed and developed in the work of Rocha [6], which presented a comprehensive numerical and experimental investigation on airfoil shaped endplates for FS vehicles, demonstrating their ability to reduce induced drag while maintaining downforce compared to flat profiles. The force balance, originally designed for the Aerospace Engineering Laboratory at Instituto Superior Técnico [4], was employed for the experimental testing in this work at the LNEC wind tunnel.

Another significant contribution is the work by Carreira [7], which focused on analyzing how variations in vehicle attitude influence the aerodynamics of the FST10e prototype. This study utilized CFD simulations to develop an aerodynamic map that decomposed the vehicle's attitude into five key parameters: front and rear ride heights, roll, steering, and yaw angles. The results from these simulations were subsequently assessed through on-track tests, allowing the author to identify trends that aligned with the CFD predictions. Throughout this work, Carreira performed a model analysis on the full scale prototype and automated the setup process for CFD simulations on both straight and cornering conditions by developing a macro. Additionally, the author created a parametrized CAD model of the vehicle, enabling the adjustment of key parameters, such as ride heights and roll. For the present study, an updated version of this parametrized CAD model was employed, along with a refined macro, adapted for the latest *Siemens Star-CCM+*® versions.

Another pertinent work is that of Pacheco [8], which addresses the necessity for reliable experimental data to evaluate the accuracy of CFD simulations, often the primary tool used in aerodynamic design within FST Lisboa. Pacheco's research involved the design, manufacturing, and testing of a 1:3 scale model of the FST10e, equipped with static tires and appendices that allowed for adjustments to the vehicle's height and attitude. The main objective was to compare wind tunnel test results with CFD simulations to identify discrepancies and improve the reliability of numerical predictions. The study demonstrated that while CFD simulations effectively captured general aerodynamic trends, wind tunnel experiments were critical for identifying specific inaccuracies, particularly in complex flow regions. These findings led to refinements in the numerical models, thereby improving their accuracy and predictive power. This work laid the foundation for subsequent wind tunnel testing, including the present study, by establishing a rigorous experimental process. It also involved the use of the aforementioned aerodynamic force balance and provided key insights into building scaled models, some techniques from which were employed in this work.

The studies conducted by Afonso [9] and Morgado [10], undertaken within the same time frame, shared the common objective of enhancing the performance of the FST prototype through the redesign of different components of the aerodynamic package, utilizing both numerical simulations and wind tunnel testing. Afonso's research focused on the vehicle's rear end, while Morgado concentrated on the rear wing. Building on the methodology from these studies, the design phase in the present work followed a similar approach, involving an iterative design phase of the side elements of the prototype. Promising designs were selected, 3D printed, and incorporated into the scaled model, which was developed for wind tunnel testing.

Beyond the FST Lisboa team, access to publicly available research on aerodynamics in motorsports, particularly within the context of Formula Student, is limited. Nonetheless, there remains relevant studies that can be considered at this stage.

Wordley and Saunders [3] present the initial design of an aerodynamic package for a Formula SAE vehicle, focusing on maximizing downforce while balancing the trade offs of increased drag and reduced top speed. The research outlines the methodology for designing the wings and profiles through both CFD and empirical methods. The authors acknowledge the difficulty in accurately predicting and quantifying aerodynamic effects due to limited resources and testing opportunities. The follow up study [11] incorporates detailed CFD analysis, wind tunnel testing, and on-track validation to refine the high downforce aerodynamic package for the Monash University Formula SAE vehicle. Multiple element wing profiles are tested both isolated and integrated on the vehicle to assess the interaction between the wings and the car's body. The results show significant downforce reductions when the wings are mounted on the vehicle, highlighting the complexity of aerodynamic interactions. Wind tunnel experiments and on-track tests confirm that while CFD predictions are useful, experimental validation is essential to fine tune the aerodynamics for competitive performance.

Additional relevant research by Cole [12], investigates the aerodynamic design of the 2022 West Virginia University (WVU) Formula SAE car. The research aims to integrate aerodynamic features such as front and rear wings, an underwing, and sidepods into the vehicle and evaluate their impact on overall vehicle performance. Using CFD and dynamic vehicle simulation tools, the author assesses the effects of aerodynamic modifications on parameters like cornering speed, lateral acceleration, and yaw acceleration. Key findings show that the resultant aerodynamic package increased lateral acceleration and reduced skidpad time during experimental testing. These results closely correlated with the predictions from the dynamic simulations, which forecasted similar improvements in vehicle performance.

Lastly, Oxyzoglou [13] centers on the design of the aerodynamic package for the 2016 University of Thessaly Formula Student car. The key design challenges identified include balancing aerodynamic efficiency with regulatory constraints, optimizing the undertray to leverage ground effects, and achieving a well distributed aerodynamic force between the front and rear of the vehicle.

1.3 Objectives and Deliverables

One of the drivers of this work was the design of the side elements of the FST14 (Figure 1.3), the latest prototype developed by FST Lisboa, and enhance its aerodynamic performance. This segment of the aerodynamic package was selected mainly due to its efficiency in downforce generation, as illustrated in Figure 1.4, relative to the increase in drag. This efficiency arises from its positioning, which enables it to leverage from ground effect, making it possible to expect that the vehicle's overall aerodynamic potential can be better fulfilled through further refinement in this area.

Figure 1.3: FST14's main aerodynamic devices.

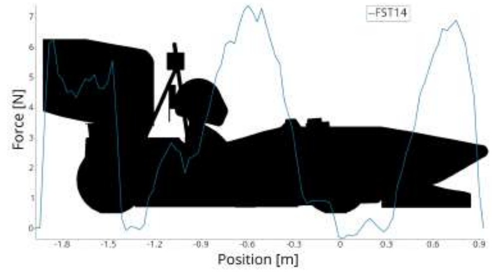

Figure 1.4: FST14's downforce distribution.

Another key driver is to reintroduce wind tunnel testing as a validation tool within the team's design methodology. Although some previous work in this area had been conducted, it was not systematically incorporated into the design process [8–10]. By integrating wind tunnel experimentation, this work aims to further bridge the gap between CFD simulations and real world performance. A 1:3 scale model of the FST14 was manufactured and tested across multiple configurations in the aeronautical wind tunnel at the Laboratório Nacional de Engenharia Civil (LNEC), using IST's aerodynamic force balance with the necessary modifications to facilitate these experiments [4].

This work focused on developing an efficient and repeatable numerical methodology capable of accurately predicting aerodynamic performance under both on-track and wind tunnel conditions. A sequence of simulation stages was carried out to isolate the effects of factors such as geometric scaling, boundary condition variations, and blockage. This systematic approach eventually allows for direct comparison between numerical and experimental results, ensuring confidence in the CFD setup before applying it to the performance assessment of the side elements. Notably, although the methodology developed in this work was applied specifically to a Formula Student car, the approach can be extended to any aerospace vehicle, highlighting the broader applicability of the techniques employed beyond automotive contexts.

To meet the goals, this work encompassed the following tasks:

- **Side Element Design:** Define the three side element designs for subsequent analysis;
- **Numerical Characterization:** Perform a mesh convergence study to estimate numerical error, define the reference simulation setup, and select the mesh refinement appropriate for later stages of the study;
- **Force Balance Calibration:** Calibrate the aerodynamic force balance to ensure the accuracy and reliability of the results obtained from the entire experimental setup in the LNEC wind tunnel;
- **Scaled Model Development:** Develop, manufacture, and assemble a 1:3 scale model of the latest

prototype for experimental evaluation;

- **Configuration Testing:** Execution of multiple wind tunnel tests across different configurations, comparing aerodynamic coefficients and surface pressure distributions with CFD results to assess performance trends;
- **Flow Visualization:** Apply wool tuft flow visualization to qualitatively assess the surface flow behavior and compare it with numerical predictions;
- **Condition Assessment:** Conduct numerical studies to isolate the effects of simulation parameters specific to the experimental campaigns, thereby enabling meaningful comparisons
- **Improved Design:** Establish the improved side element design based on the analysis of the numerical results under on-track conditions for the tested configurations, leaving it ready for implementation in the FST14 prototype.

1.4 Thesis Outline

This thesis is organized into seven chapters.

Chapter 1 introduces the research topic and outlines the specific objectives and expected deliverables of the work. A brief overview of the thesis structure is also provided alongside a summary of relevant previous work in the field.

Chapter 2 covers the fundamental principles of aerodynamics on a racing car. The methodologies and instruments employed for aerodynamic analysis, such as CFD and experimental testing, are also reviewed. The chapter concludes with an introduction of the working geometry of the FST14, highlighting the design and respective purpose of its side elements.

Chapter 3 details the numerical methodology adopted throughout this work. It begins with the definition of the computational domain, boundary conditions, and wall modeling strategy, followed by a mesh convergence study used to estimate the numerical error and select the desired mesh refinement.

Chapter 4 outlines the experimental setup used for the wind tunnel testing. It begins by describing the force balance system, including its calibration procedure and data acquisition. The chapter then details the characteristics of the wind tunnel employed in the present study. Finally, the testing procedure is explained, along with a discussion of the limitations encountered during the experiments.

Chapter 5 focuses on the wind tunnel testing campaign and its comparison with numerical simulations. It presents the design, manufacturing, and assembly of the 1:3 scale FST14 model, addressing flow similarity, and instrumentation setup. The experimental results, including aerodynamic coefficients, surface pressure distributions, and tuft based flow visualizations, are compared against the CFD simulations to evaluate the correlation between both approaches.

Chapter 6 extends the validated numerical methodology to on-track conditions. The influence of ride height, geometric scale, blockage, and varying boundary conditions is quantified, enabling the identification of the main aerodynamic trends of the side elements under real world conditions. The performance of the three side element configurations is then compared under representative vehicle conditions.

Chapter 7 summarizes the main achievements of the research, discussing the implications of the findings for future Formula Student designs. It also highlights potential areas for future work.

Chapter 2

Race Car Aerodynamics

2.1 Vehicle Performance

To fully comprehend the crucial role of aerodynamics in vehicle performance, it is essential to understand the fundamental dynamics experienced by a car on track. Aerodynamic loads directly influence performance through lift and drag forces and indirectly by modifying the tire friction coefficient as a result of variations in lift or downforce.

Since the tire contact patches constitute the only points of interaction between the race car and the track surface, maximizing the generated tire forces during acceleration, cornering, and braking is essential for optimal performance. There are primarily two methods for increasing the normal load on each tire. The first involves raising the vehicle's weight; however, this approach is undesirable, as it also increases the vehicle's inertia, thereby requiring additional power for acceleration, braking, and turning. The second, a much more efficient method, is to enhance aerodynamic loads, specifically downforce, by incorporating an aerodynamic package. This approach effectively increases vertical loads without significantly adding to the vehicle's mass [14].

Aerodynamics adds another layer of complexity, especially at higher speeds, when it comes to reach the desired balance while cornering. In order to obtain as close to a neutral handling as possible, each tire should experience approximately the same applied load. However, this condition is almost unattainable, mainly due to the vehicle's mass distribution combined with downforce generation. When a vehicle carries a greater load on the front axle, it tends to exhibit oversteer, as the increased front rotation may induce to sliding of the rear tires. Alternatively, if the load on the rear axle exceeds that on the front, understeer occurs [15].

Achieving a balanced handling response between oversteer and understeer requires a design that incorporates an appropriate aerodynamic load distribution, commonly referred to as aerobalance. Aerobalance is a critical parameter in the development of an aerodynamic package, as it significantly influences vehicle behavior during cornering. Nevertheless, a definitive target for aerodynamic balance remains elusive, and the preference for either understeer or oversteer in a race car is often contingent upon the individual characteristics of the respective driver, depending on personal driving styles.

2.2 Fundamental Aerodynamic Phenomena

General Aerodynamics

As race cars travel through the air, pressure gradients form around their surfaces, usually body work and wings, resulting in aerodynamic forces that ultimately act on the tires of the vehicle in motion [16–19]. In particular the components Lift, L, and drag, D, perpendicular and parallel to the incoming flow, respectively [20]. In addition, a side force, is also generated, mainly during cornering, and acts towards the center of the respective corner. These three force components also correspond to the axes of rotation for all moments generated, usually mentioned as yaw, roll, and pitch, illustrated in Figure 2.1.

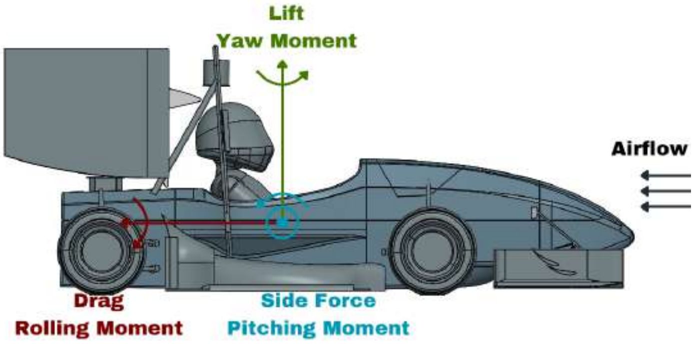

Figure 2.1: Representation of the force components along with the axes of rotation.

Within FST Lisboa, the primary objective in the design of aerodynamic devices is the generation of negative lift, commonly referred to as downforce, with drag minimization being a secondary consideration. To enable meaningful analysis, it is essential to express each of these force components in terms of dimensionless coefficients: the lift coefficient, C_L, defined as positive for a downward force component; the drag coefficient, C_D, defined as positive in the downstream direction, and the pitching moment coefficient, C_{M_y}, defined as positive for a nose-up rotation,

$$C_L = \frac{-L}{\frac{1}{2}\rho U_\infty^2 A} \qquad C_D = \frac{D}{\frac{1}{2}\rho U_\infty^2 A} \qquad C_{M_y} = \frac{M_y}{\frac{1}{2}\rho U_\infty^2 Ac}\,, \tag{2.1}$$

where ρ denotes the air density, A represents the reference area, typically the frontal area in motorsport applications, U_∞ is the uniform free stream speed, and c is the reference length, which in this study corresponds to the car's wheelbase.

Additionally, one further quantity of interest is the aerobalance, which describes the distribution of the total aerodynamic forces between the front and rear axles. In the present work, it is expressed as the percentage of the total load acting on the front axle, denoted as $\%\,Front$, and serves as a key parameter for tuning the vehicle's handling balance and stability. Later in this work, to calculate the aerobalance of the experimental model, the x-coordinate of the pressure center (CoP) was first determined relative to the model's attachment point to the force balance, using only the longitudinal loads F_z, F_x, and M_y, while neglecting F_y, M_z, and M_x due to symmetry [8]:

$$\sum M_{CoP} = 0 \Rightarrow M_y - F_x \Delta z - F_z \Delta x = 0 \Leftrightarrow \Delta x = \frac{M_y - F_x \Delta z}{F_z} \ . \tag{2.2}$$

In this calculation, the height of the CoP was assumed to coincide with that of the center of gravity (CoG), estimated at $z = 0.333 \text{ m}$ for the full scale vehicle, which scales to $z = 0.111 \text{ m}$ for the experimental model. With the x-coordinate of the CoP known, the aerobalance was then calculated using:

$$\text{Aerobalance (\% Front)} = \frac{x_{\text{CoP}} - x_{\text{Rear}}}{\text{Wheelbase}} \times 100. \tag{2.3}$$

Boundary Layer

Under realistic flow conditions, fluid elements in direct contact with a solid wall adhere to its surface. The region near a surface where the quantifiable effects of shear stresses induced by velocity gradients and viscosity manifest is known as the boundary layer [16]. A boundary layer can exist in three distinct regimes: laminar, transition or turbulent. In a laminar boundary layer, characterized by a low Reynolds number, the flow is organized in well defined layers. In contrast, at sufficiently high Reynolds numbers, the laminar boundary layer flow becomes unstable to small disturbances, triggering transition to turbulence. The resulting turbulent regime is characterized by velocity fluctuations about a mean value, encompassing a broad spectrum of frequencies [21]. The turbulent boundary layer exhibits much stronger momentum mixing due to turbulent eddies, which act as an effective diffusivity several orders of magnitude higher than molecular viscosity. As a result, turbulent boundary layers typically grow faster and become thicker than laminar ones under equivalent flow conditions. Nonetheless, due to the enhanced mixing and higher momentum near the wall, turbulent boundary layers exhibit more resistance to flow separation [16].

The phenomenon of boundary layer separation, illustrated in Figure 2.2, is of particular relevance to this study. The boundary layer significantly influences airflow characteristics around a body, not only due to the wall shear stresses that induce a friction force but also because, under adverse pressure gradients ($\frac{dp}{dx} > 0$), which often occur on the suction side of wings downstream of the suction peak, the airflow may separate from the surface. This separation can substantially alter the airflow configuration, leading to a significant increase of pressure drag and a potential loss of lift or downforce. The separation point is defined as the location where the limiting streamline detaches from the surface. In two-dimensional flow, this corresponds to the point where the wall shear stress becomes zero, i.e., $\tau_w = 0$ [16]. Given that a turbulent boundary layer is less prone to flow separation than a laminar one, with the onset of separation effectively delayed, certain aerodynamic surfaces, such as wings, often incorporate devices that promote transition to turbulent flow, even at the expense of increased friction drag, since the pressure drag associated with flow separation is considerably greater.

Performance Aerodynamics

Several key concepts are essential for analyzing the aerodynamic performance of the various design iterations developed in this study. The first is the concept of ground effect, which involves position-

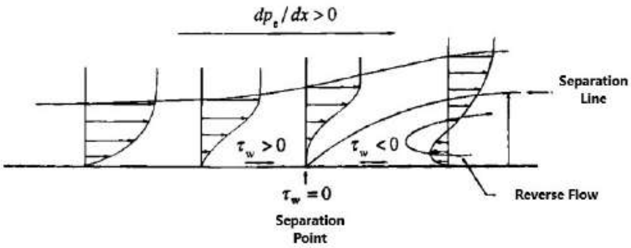

Figure 2.2: Airflow separation [16].

ing wings or other aerodynamic surfaces in close proximity to the ground [22]. This close proximity constrains the airflow, further decreasing the static pressure in this region and thereby increasing the downforce generated.

As the cross-sectional area decreases, the flow velocity must increase to conserve mass flow, resulting in a drop in static pressure within the narrow throat region, as described by Bernoulli's equation [16]. This localized reduction in static pressure effectively pulls the aerodynamic devices toward the ground, a phenomenon observable in Figure 2.3 [23].

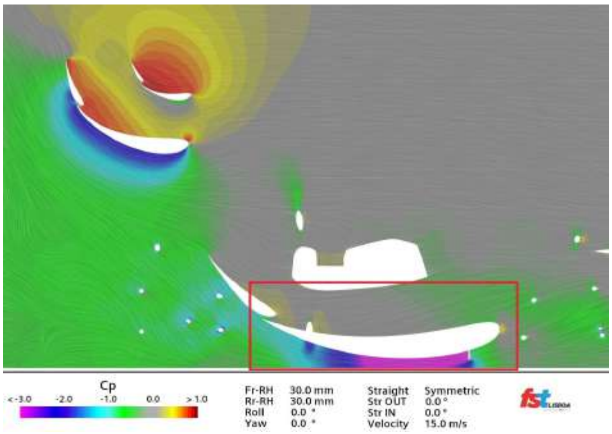

Figure 2.3: Static pressure on a section of FST13.

To provide additional physical insight into the effect of ground proximity, one can resort to the method of images. In the context of potential flow, this method allows the modeling of flows near solid boundaries by introducing an image system that mirrors the real flow on the opposite side of the boundary. For instance, a vortex of intensity $+\Gamma$ located at a distance d from a plane wall can be represented by introducing a symmetric image vortex of intensity $-\Gamma$ positioned at an equal distance on the opposite side of the boundary. As the vortex approaches the wall, i.e., as $d \to 0$, the interaction between the real and image vortices can be approximated by a single vortex of effective intensity 2Γ, as shown in Figure 2.4 [16].

While this principle is strictly valid for potential flow and fusiform bodies, it offers valuable qualitative insights even for more complex geometries such as competitive vehicles. In such cases, the image of the vehicle can be considered a mirrored version reflected across the ground plane, as illustrated in Figure 2.5. Since the vehicles under study feature aerodynamic surfaces, such as wings, placed close to the ground, a two dimensional analysis with a cross section, such as the one depicted in Figure 2.3

can be used to illustrate the effect. In this view, airfoils may be represented as bound vortices generating negative lift via the Kutta-Joukowski theorem. The presence of the image vortices beneath the airfoils modifies the surrounding velocity field, compressing the streamlines below the surface, thereby accelerating the flow and lowering the static pressure in accordance with Bernoulli's principle [16].

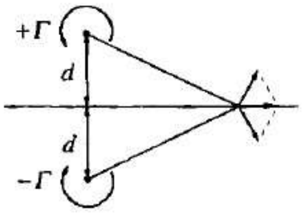

Figure 2.4: Modeling of a vortex on a flat wall [16].

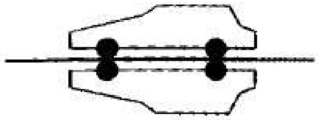

Figure 2.5: Modeling of a vehicle on a road [16].

Aerodynamicists seek to seal the vehicle's underbody flow as effectively as possible; any leakage compromises the suction effect, making ground effect less predictable and reducing its aerodynamic benefit [23]. However, the trend of decreasing ground clearance resulting in increased downforce reverses at a certain minimal distance due to viscous effects, specifically the flow separation that can occur in the adverse pressure gradient region if the suction at the throat becomes too intense. Regarding drag, it increases consistently as ground clearance decreases [15].

Another key concept essential to this study is the formation of vortices. A vortex tube represents a rotating motion of fluid around a central axis and is characterized by its circulation, which quantifies the flux of vorticity (twice the rotation speed of the fluid elements) trough the vortex tube section [24]. At first glance, vortices may seem undesirable, as they are often associated with flow separation, which is generally detrimental to a vehicle's aerodynamic performance. However, beneficial streamwise vortices can be generated at sharp edges due to three-dimensional transversal flow separation, occurring as the flow transitions from a high pressure region to a lower pressure one. As the air attempts to follow the sharp turn imposed by the geometry, transverse flow separation occurs and an angular velocity component is introduced, forming a vortex. The vorticity within the vortex core leads to a significant reduction in static pressure. When positioned downstream, such vortices can be strategically exploited in various ways. For instance, they can help reduce the static pressure under the vehicle, thereby increasing downforce, or they may beneficially modify the airflow direction, such as by redirecting tire wakes. Additionally, vortices can help sustain low pressure zones by effectively sealing flow regions. Despite these advantages, vortex generation is inherently accompanied by an increase in drag. This added drag, known as induced drag, arises due to the downforce generated and increases proportionally with it, as described by

$$C_{D_i} = \frac{C_L^2}{\pi A R e} \,, \tag{2.4}$$

where AR is the aspect ratio and e is an efficiency factor [22]. Manipulating vortices to improve pressure distribution around a vehicle carries inherent risks. A key phenomenon to consider is vortex bursting, which occurs as a vortex moves downstream and gradually weakens and expands due to viscous dissipation of its kinetic energy. Eventually, if the vorticity in the vortex core decreases sufficiently, its structure destabilizes and bursts, creating substantial wake regions. This effect can occur abruptly, leading not only to a loss of aerodynamic effectiveness but also to potential disruptions in downstream flow, compromising overall performance [25].

2.3 Main Aerodynamic Devices

In FS type vehicles, the aerodynamic devices are usually divided into three primary groups: front, side, and rear (Figure 1.3). Each component within these groups serves distinct functions to achieve optimal aerodynamic performance. The following sections will examine a typical Formula Student vehicle, progressing from front to rear aerodynamic devices.

Front Aerodynamic Devices

Starting with the front wing (FW), displayed in Figure 2.6, its primary characteristic is to be the first component to interact with incoming airflow, meeting it in a nearly undisturbed state. This allows it to encounter flow unaffected by viscosity, which, combined with its typically low position to exploit ground effect, enables it to generate downforce efficiently with relatively low drag. The second function is to direct airflow appropriately through the rest of the vehicle, aligning with the chosen aerodynamic concept. For instance, the front wing plays a critical role in directing sufficient airflow to the underbody, maximizing its effectiveness [26].

A typical front wing consists of a multiple element wing and endplates. The multi-element configuration primarily serves to generate downforce, though they also play a role in directing airflow by producing beneficial wingtip vortices or by adjusting the load distribution across its wing span. The endplates, in particular, mitigate wingtip vortex intensity, thereby reducing induced drag and effectively increasing the angle of attack, which enhances downforce generation. The trend toward wider front wings, which naturally increase downforce by providing more surface area, has also led to endplates capable of generating advantageous vortices that better control downstream airflow and minimize wheel wake interference. To amplify this effect, these endplates may be airfoil shaped to produce additional outwash, further redirecting airflow away from the tires.

Figure 2.6: Front wing of the FST14.

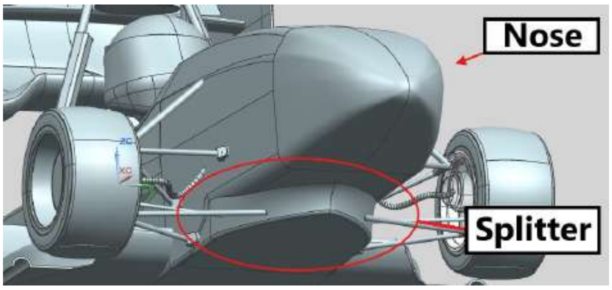

Figure 2.7: Example of a nose and a splitter on a FS car.

The nose, while potentially generating small amounts of lift, plays a crucial role in channeling air toward the car's underside. Meanwhile, the splitter assists in guiding air around the regulatory step in the chassis and also directs airflow toward the side of the vehicle. Despite their relatively simple shapes (see Figure 2.7), these components can significantly contribute to the vehicle's overall aerodynamic performance.

Side Aerodynamic Devices

Moving to the side elements on the vehicle, which are the focus of this work, the primary aerodynamic component in this region of a typical Formula Student car is the side diffuser (Figure 2.8), which consists of a main airfoil shaped plane with a relatively large chord that also leverages from ground effect [27]. Depending on the team's design concept, the diffuser may be the most aerodynamically efficient part of the car [28]. The performance of a diffuser is assessed by its pressure recovery, which is influenced by factors such as inlet and outlet areas, diffuser or ramp angles [29].

Many teams often add a smaller flap directly above the diffuser's outlet. This flap not only increases the downforce by naturally expanding the area of aerodynamic surfaces but also enhances airflow in the expanding section. By creating a low pressure region on its lower surface, the flap helps prevent flow separation on the diffuser by drawing in and accelerating the airflow attenuating the adverse pressure gradient close to the outlet region [30].

Furthermore, in an effort to maximize the design box space, teams commonly attach a component known as a footplate to the main diffuser plane. The footplate typically consists of a flat, horizontal plate positioned close to the ground and may incorporate additional vortex generators to isolate the side diffuser, a crucial factor for maximizing its performance [15]. These vortex generators can also draw disturbed air from within the diffuser, further enhancing its efficiency. Another form of vortex generator, often referred to as strakes, consists of thin plates attached to the lower of the side diffuser. Strakes generate vortices with low pressure cores that accelerate the surrounding airflow, intensifying the suction peak. Additionally, the increased turbulence in this region helps delay flow separation. Depending on the design concept, these vortices can also aid in redirecting airflow and generating additional outwash [31].

Figure 2.8: Example of the side diffuser assembly of a FS car (AMZ Racing).

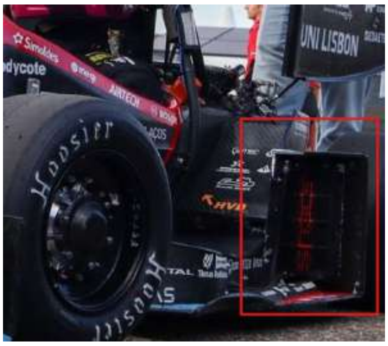

Figure 2.9: Radiator placement on the FST13.

Finally, many teams position their cooling devices in this region, where aerodynamic components can be designed to enhance cooling performance. In previous FST Lisboa prototypes, the radiators have been placed in front of the rear tires, mounted on a thin vertical flat plate, as seen in Figure 2.9. While this vertical plate may initially appear to be a drag inducing element, as it is perpendicular to the airflow, it actually provides beneficial effects by isolating the rear tire wake and preventing it from interfering with the side diffuser, thereby enhancing its efficiency. Additionally, some teams place side pods above the side diffuser to capture most of the cooling air, with air intake capture being their primary function. Although their main role is to provide airflow unaffected by viscosity to the cooling inlets, side pods also help prevent flow separation along the vehicle's side due to their airfoil like shape. They further guide airflow toward the rear components, improving overall aerodynamic efficiency. In fact, McBeath notes that the drag coefficient of a radiator simply mounted on the side of a vehicle can be 7 to 13 times higher than that of properly ducted systems [23].

Rear Aerodynamic Devices

The primary element in this region is the rear wing (RW), the most common aerodynamic appendage on any competition vehicle. It may consist of a single or multiple multi-element wings along with large endplates. For example, the FST13 featured two two-element configurations, each comprising a main element and a smaller flap (Figure 2.11). The operating conditions of a rear wing differ significantly from those of the front wing or side diffuser. Positioned higher on the vehicle, the rear wing is less able to leverage ground effect, and, being located at the rear, in the disrupted flow region, it is less efficient.

Ideally, a rear wing should be positioned as high as regulations allow to minimize the influence of upstream elements. Due to these airflow conditions, achieving substantial downforce, the rear wing's primary purpose, requires steeper camber lines and higher angles of attack. However, this design increases drag, as low pressure regions form behind the rear wing, and steep angles can even cause flow separations, a significant challenge in rear wing development [32]. To address the drag penalty, teams now often incorporate a DRS into their rear wings, which allows for adjustments to the angle of attack on certain elements of the multiple component wings [33].

Figure 2.10: Example of a rear diffuser on a FS car (KA Raceing).

Figure 2.11: FST13's rear wing with DRS open.

Additionally, teams often attach a thin perpendicular tab known as a Gurney flap to the trailing edge of the final flaps of their respective multi-component wings [34], although it can also be applied to front wings but less frequently. A Gurney flap promotes boundary layer separation near the trailing edge on the upper surface of the flap, leading to the formation of recirculation zones both fore and aft of the tab. This separation alters the streamline curvature and effectively increases the camber, thereby enhancing downforce generation, albeit with an associated drag penalty [35].

Regarding rear wing endplates, their geometries can become quite complex. While the primary function of any endplate is to mitigate the drag inducing wingtip vortex that would otherwise form, rear wing endplates in Formula Student cars serve multiple additional purposes. Due to their typically large dimensions and location, endplates are able to block the interference of rear tire wake with the rear wing. Endplates can further enhance downforce or reduce drag through features like louvers or cutouts [36]. Cutouts, often placed at the top of the endplate, help reduce drag by creating a counter rotating vortex that weakens the main wingtip vortex. Louvers, on the other hand, are small airfoil shaped openings that, when properly positioned, generate smaller vortices than those naturally formed at the endplate tip, thereby reducing the associated drag. These vortices can also be directed toward the lower surface of the wing, effectively decreasing the local static pressure and enhancing aerodynamic efficiency.

Finally, at the rear most section of a Formula Student car, some teams choose to incorporate a rear diffuser (see Figure 2.10). The primary distinction from the side diffuser lies in the location of the expanding section, with the rear diffuser's outlet positioned behind the rear tires. In terms of width, the rear diffuser may span the full track of the vehicle or only the monocoque portion. This makes it essential to design a monocoque underbody that effectively utilizes the Venturi principle, ensuring the rear diffuser's aerodynamic efficiency and overall viability of the part.

2.4 Methodologies for Aerodynamic Analysis

Aerodynamic analysis typically encompasses three main components: numerical simulations using CFD, wind tunnel testing, and on-track testing. On-track testing falls outside the scope of the study.

2.4.1 Computational Fluid Dynamics

Computational fluid dynamics uses numerical methods and computer codes to obtain solutions of the equations that govern fluid flows. In the past, aerodynamic designs could only be tested through physical prototypes. However, with advancements in computational power and numerical algorithms, CFD has introduced numerous advantages to the aerodynamic design process. Today, CFD is a widely used and highly effective tool. In the motorsport industry, for example, it allows engineers to simulate the airflow behavior around a car without needing to build prototypes of new designs for track or wind tunnel testing. This makes CFD a more cost effective and time efficient solution.

The governing equations that describe airflow behavior are the Navier-Stokes equations, which are a set of partial differential equations. These equations represent the most comprehensive model currently available for fluid motion, capturing the relationships between velocity, pressure, temperature, and density in a moving fluid while accounting for viscous effects. However, solving these complex and non-linear equations for complex geometries and high Reynolds numbers, is incredibly challenging and would require significant computational resources.

Solving the Navier–Stokes equations directly through Direct Numerical Simulation (DNS) requires resolving the full spectrum of turbulent scales, from the largest energy containing eddies to the smallest dissipative structures. This demands extremely fine spatial and temporal resolutions, rendering the approach computationally prohibitive for most practical applications [37, 38].

Large Eddy Simulation (LES) was proposed as a less expensive and more approximate method, where the flow equations are solved numerically, but only the larger turbulent structures (or eddies) are directly calculated. This approach provides an approximation of the actual flow, where smaller details are not included. To address this gap, subgrid scale models are added to represent the smaller eddies and their role in energy dissipation [38]. This allows for a coarser computational grid compared to DNS [39]. However, even with these simplifications, LES still requires significant computational resources for analyzing most real world flow scenarios.

Lastly, there is the Reynolds Averaged Navier-Stokes (RANS) approach, especially used in wall bounded flows, which introduces Reynolds decomposition and averages the Navier-Stokes equations over space and time. In the Reynolds decomposition, the dependent variables in the N-S equations are split into mean and fluctuating components. This statistical procedure generates the Reynolds stress tensor that accounts for the effects of turbulent motions on the mean flow [40]. While this method is less computationally demanding compared to the previously discussed approaches, it models all turbulent scales (see Figure 2.13) and so it looses modeling accuracy, as displayed in Figure 2.12. Nevertheless, RANS remains the most widely used method for analyzing complex flows at high Reynolds numbers, as it allows for the evaluation of nearly any geometry [41].

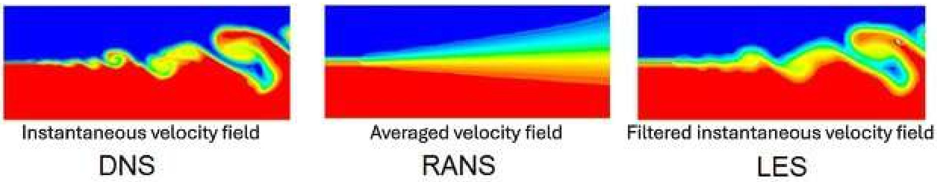

Figure 2.12: Comparison of DNS, LES and RANS on an interfacial flow. [42].

Since turbulence is present in nearly all flows, it must be modeled when using the RANS approach. Commonly used two-equation models solve two separate transport equations for independent turbulence quantities that are directly related to turbulence length and time scales. Among the most popular models are the $k - \epsilon$ model, which derives length and time scales from the turbulent kinetic energy, k, and the turbulent dissipation rate, ϵ, and the $k - \omega$ model [43], which solves two transport equations: one for k and another for the reciprocal turbulent time scale, $\omega = \epsilon/k$. These models differ in how they handle flows, particularly near walls. The $k - \omega$ model excels in predicting boundary layer behavior, while the $k - \epsilon$ model performs better outside the boundary layer, where $k - \omega$ tends to be too sensitive to outer flow boundary conditions [44].

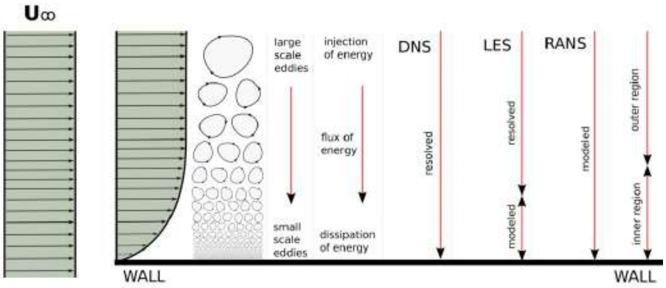

Figure 2.13: Turbulence modeling approaches [45].

To combine the strengths of both models, Menter [46] introduced two improved versions of the $k-\omega$ model. The Baseline (BSL) model provides results similar to the original $k-\omega$ but reduces its sensitivity to arbitrary free stream values. This model matches the $k-\omega$ formulation in the inner 50% of the boundary layer and transitions to the $k-\epsilon$ model towards the outer edge, achieving good performance in free shear layers. The second version, the Shear Stress Transport (SST) model, builds on the BSL approach by incorporating the transport of principal turbulent shear stresses, particularly in adverse pressure gradient boundary layers. The SST model retains independence from free stream values while delivering better agreement with experimental data in these scenarios, highlighting its importance in the context of the present study.

Additionally, many other approaches and turbulence models can be used, such as the Detached Eddy Simulation (DES), which is essentially a hybrid method combining RANS and LES techniques. Another example is the $k-\epsilon-C_{as}$ turbulence model introduced in [47], which aims to improve the accuracy of the RANS approach specifically for motorsport applications.

Assessment of the Numerical Quality of Results

To determine the numerical accuracy of CFD results, it is key to quantify the numerical error associated with the simulations. The numerical error $e(\phi)$ of any variable is given by the difference between the approximated solution ϕ_i and the exact solution ϕ_{exact} [48],

$$e(\phi) = \phi_i - \phi_{exact} \ . \tag{2.5}$$

As the numerical problems to be solved in this work are highly non-linear, it is impossible to obtain ϕ_{exact}. Nevertheless, some methods may be employed to obtain an estimation of the numerical error as adopted in Section 3.2.2. First, it is necessary to split the numerical error into its components [49]:

- **Round-off Error**: arises from the finite precision of computer arithmetic and the limited number of significant digits that can be retained during calculations. Accurately quantifying this type of error would require knowledge of the numerical solution computed with infinite precision, which is not feasible.

- **Iterative Error**: arises from several factors, including the non-linear nature of the equations, the deferred corrections applied in the discretization schemes to achieve second-order accuracy, the iterative methods employed to solve the resulting system of linear equations, and the segregated solution approach, in which equations are solved sequentially rather than simultaneously. However, in the present work, a coupled solving method was applied to the RANS equations in the numerical simulations. Be that as it may, the solution of the turbulence model remained segregated.

- **Discretization Error**: arises from the transformation of the differential equations in the governing mathematical models into a system of algebraic equations, which are then solved numerically. This source of error is typically the dominant component of the overall numerical error, especially when the geometry involves high curvature. Unlike round-off and iterative errors, discretization error tends to decrease as the number of degrees of freedom increases. However, estimating the discretization error requires knowledge of the exact solution, ϕ_{exact}, which is not available in the present case. Consequently, discretization error is often estimated using mesh convergence studies.

2.4.2 Experimental Testing

While CFD serves as a powerful tool for aerodynamic design, the experimental validation of computational models remains an essential part of the development process. Such validation, however, requires wind tunnel facilities capable of reproducing a highly specific set of conditions relevant to the application. Experimental Fluid Dynamics (EFD) generally comprises two primary approaches: wind tunnel testing and on-track testing. On-track testing is difficult to control, whereas wind tunnel testing offers a controlled environment but severally modified relative to real on-track conditions. In this study, wind tunnel testing is employed as the chosen EFD method.

In wind tunnel testing, typically a scaled model of the desired geometry is positioned in the test section of the tunnel, where large fans generate a controlled airflow around the model [50]. This setup keeps the model stationary while simulating the airflow it would experience on the track. The resulting data can then be evaluated and compared to the predictions obtained from CFD simulations.

Wind tunnels can be classified based on their test section configuration, which can be either open or closed. Additionally, they can be categorized by their tunnel geometry: an open return tunnel draws air from the surrounding room into the test section and exhausts it back into the room, while a closed return tunnel recirculates the air within the system [51]. The wind tunnel used in this study was the aeronautical wind tunnel at LNEC. It is a closed return tunnel with a closed test section, though it can also be configured as an open section if needed (see Section 4.3).

For gathering results, three main methods will be employed in this study. First, aerodynamic forces and moments can be directly measured by placing the model on a force balance [4]. It is crucial to ensure proper calibration of the balance for accurate results. This process will be discussed in Section 4.1. Additionally, if the model is equipped with pressure taps in specific areas, pressure measurements can be taken, allowing for the static pressure distribution along key surfaces to be obtained [23]. Lastly, flow visualization techniques can be applied, such as attaching wool tufts to the model's surface, using an oil mixture to capture the airflow pattern, or employing smoke to visualize the free stream flow through the model [23]. All of these techniques assume that the flow visualization medium moves in sync with the airflow, enabling a qualitative comparison between CFD simulations and real world conditions by observing streamlines and separation zones.

While wind tunnel testing is a valuable tool, it does have its flaws and limitations. These tests often use scaled models, which can make it difficult to match the Reynolds number to that of the full sized vehicle. To achieve similar Reynolds numbers under incompressible flow, the airflow speed must be increased. However, this can cause the Mach number to exceed that of real world conditions, making it nearly impossible to achieve full flow similarity. Such differences can lead to variations between the experimental data, the numerical results and the performance of the actual full scale vehicle. In many cases of partial similarity, especially at lower Mach numbers, which is the case in this work, aerodynamic behavior is more affected by the Reynolds number. As a result, matching the Reynolds number alone can often provide a reasonable level of dynamic flow similarity [52].

Another limitation is the use of closed test sections, which can lead to blockage effects. The boundary layers on the walls of the test section can interfere with the airflow around the model and disturb wake development, leading to inaccurate estimates of aerodynamic forces and moments [53]. Using larger test sections can help reduce these blockage effects, but this would also increases the cost of the experiments.

Additionally, model geometries in wind tunnel tests are often simplified. Small features are usually left out because they are considered to have less impact on the results compared to errors caused by flow similarity issues and blockage effects.

Wind tunnel testing, compared to on-track testing, has the primary advantage of being significantly less expensive. It removes the need to book track time or transport a fully manufactured and functional prototype. This experimental method is typically employed during the design phase, where underperforming regions can be identified and improved. On the other hand, on-track testing is more commonly conducted during the final design stages, allowing for minor adjustments.

2.5 Car Geometry and Side Elements Design

2.5.1 Geometry Preparation

Before performing a numerical analysis, it is essential to have a prepared geometry suitable for testing. In this work, all 3D modeling was carried out using *Siemens NX* ®, which enabled a more seamless and efficient integration with the CFD software *Siemens Star CCM+* ®. The geometry employed in the simulations corresponds to a simplified CAD model of the FST14 prototype, presented in Figure 2.14a. Here, ”simplified” refers to deliberate modifications made to the original model to reduce complexity while preserving the essential aerodynamic characteristics. These modifications include the removal of minor details that do not significantly affect the external aerodynamic behavior of the car, such as internal components, fasteners (bolts, nuts, washers), various lids or covers, suspension bellcranks, and the headrest. Furthermore, certain components were geometrically simplified and smoothed to reduce the total cell count. Examples include a fully enclosed chassis, simplified wheel assemblies, which include the rims and uprights, the anti-roll hoop, and suspension brackets. An additional modification was the inclusion of a driver model, which plays a critical role in influencing the airflow around the vehicle.

The tires were also modified to include individual contact patches. As vertical aerodynamic loads are applied to the tires, their shapes deform accordingly, leading to the formation of these contact patches. To prevent issues during mesh generation, an extrusion was added extending downward from each contact patch, as illustrated in Figure 2.14b.

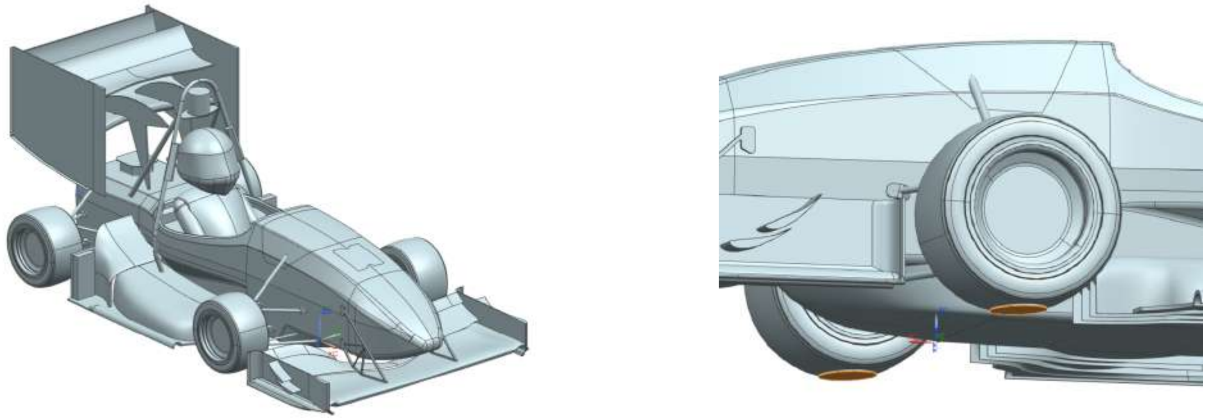

(a) Complete FST14 vehicle.

(b) Detail of tire contact patches.

Figure 2.14: Overview of the simplified CAD Model.

Finally, regarding the aerodynamic components, the trailing edges of the wings were thickened to values between $1\ \mathrm{mm}$ and $2\ \mathrm{mm}$, depending on the chord length. This modification improves the quality of the local mesh, as extremely thin trailing edges (approaching zero thickness) pose challenges for mesh generation, often resulting in poor mesh quality in those regions.

2.5.2 Side Element Geometry Description

Each geometry was designed and numerically tested under on-track conditions with the goal of maximizing the overall downforce generated by the car, that is, maximizing C_L, without significantly increasing C_D.

The design process began by analyzing the configuration of the lateral diffuser used in the previous car, the FST13 prototype, shown in Figure 1.1. This setup incorporated a high chord, low angle of attack, custom airfoil shaped main wing designed to take advantage of ground effect aerodynamics. Additionally, it featured a flap with the Selig S1223 airfoil and an endplate that extended perpendicularly from the tip of the main wing, following its contour before enclosing the flap. Further outboard, a horizontal flat plate, the footplate, houses a diagonal tubular vortex generator. Finally, three strakes located on the lower surface of the main wing were employed.

Over 80 design iterations were conducted to arrive at the final configuration implemented in the 2025 FST Lisboa prototype, the FST14, with a selection of 25 iterations and some of their results summarized in Table A.1. Among these, three representative designs were selected for detailed discussion in this work. Their respective design rationales are presented alongside their geometrical characteristics to enable performance comparisons and, more importantly, to identify aerodynamic trends relevant to this study.

The first design presented, configuration A, shown in Figure 2.15, follows the core principles of the FST13 design philosophy. It features a large airfoil shaped main wing integrated into the chassis, inspired by the Lotus 79 Formula 1 side diffuser, serving as the primary element of the lateral diffuser. This is combined with a custom designed flap derived from the Selig S1223 airfoil. The key innovation in this configuration is the implementation of a continuous surface along the upper surface of the main wing, extending seamlessly onto the footplate. This approach is intended to eliminate sharp junctions between perpendicular surfaces, thereby reducing the likelihood of flow separation, decreasing drag, and mitigating the formation of adverse vortices at transition regions. In addition, the continuous geometry promotes smoother pressure gradients, enhancing overall aerodynamic efficiency. Furthermore, the integrated surface enables enhanced passive flow control, generating a more coherent downstream flow and contributing to increased overall aerodynamic efficiency. As a result of this design, a dedicated endplate was introduced to enclose only the flap. This endplate is mounted on the footplate, which occupies the remaining allowable space defined by the design box. It is strategically shaped to follow the contour of the main wing's trailing edge, maximize the flap dimensions within the regulatory limits [2], and to be aligned with the expected local airflow to avoid the risk of flow separation. In this iteration, the tubular vortex generator was simplified into a straight configuration to facilitate manufacturing and enhance vortex generation efficiency. No additional strakes were included on the lower surface of the main wing in this initial version.

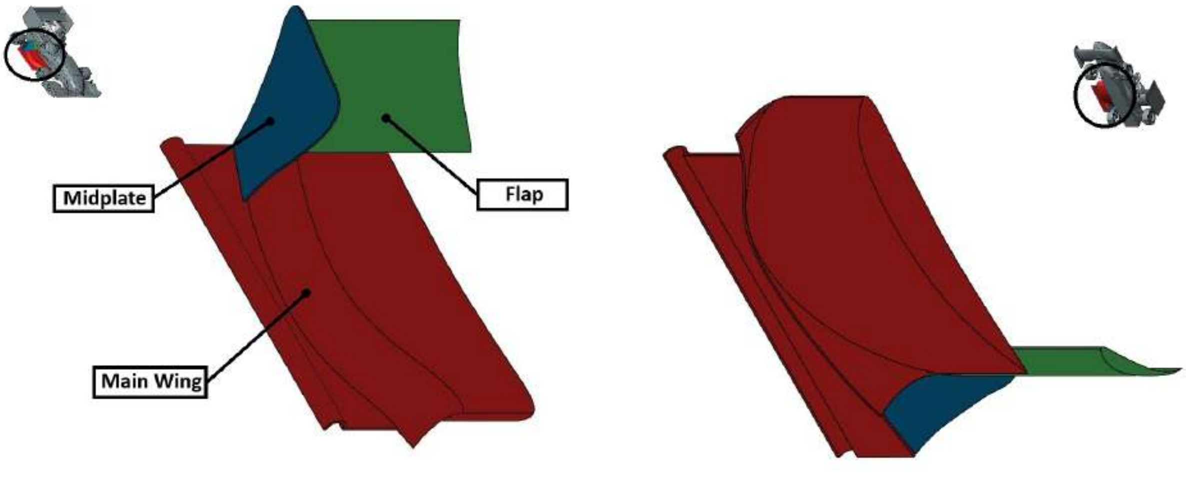

(a) Top view.

(b) Bottom view.

Figure 2.15: Configuration A - First design of side elements.

The second iteration, configuration B, shown in Figure 2.16, retains the same lateral diffuser general concept as the first, but introduces several refinements aimed at improving aerodynamic performance. First, the wingspan of the main element was increased, thereby expanding the surface area of the downforce generating wing and enhancing its overall contribution to downforce. In addition, the leading edge of the footplate was reshaped to more effectively manage the wake generated by the front tires, reducing the amount of disturbed flow entering the underside of the lateral diffuser and minimizing associated losses.

The tubular vortex generator was shortened and no longer spans the entire length of the horizontal flat plate. This adjustment was made because downstream of a certain point, the vortex generator ceased to produce coherently and instead introduced detrimental vortex bursting. Furthermore, the main wing was modified by slightly decreasing its angle of attack, and two strakes were added to introduce the ”tunnel” concept. This approach leverages the surrounding surfaces and ground to confine and sustain the vortices generated by the strakes, delaying or ideally preventing their breakdown, thereby maximizing vortex induced downforce.

However, the most significant modification in this configuration lies in the flap geometry. While it still consists of a custom airfoil emerging from the chassis, it now transitions smoothly into the footplate with a continuous airfoil shape, whose leading edge conforms to the trailing edge of the main wing. This change was initially motivated by persistent flow separation issues observed near the previously mounted endplate, which the new design successfully addresses. Additionally, the new configuration offers several aerodynamic advantages. The continuous geometry eliminates sharp edges and surface discontinuities that typically promote flow separation and vortex shedding. Moreover, this design enhances flow acceleration along its entire lower surface, further reducing local static pressure. This intensified suction promotes upstream flow acceleration, namely beneath the main wing, resulting in a significant increase in downforce generation capability. Finally, a smaller continuous flap geometry was added outboard to house the cooling radiators, similar to Figure 2.9, with the aim of integrating them in an aerodynamically efficient manner.

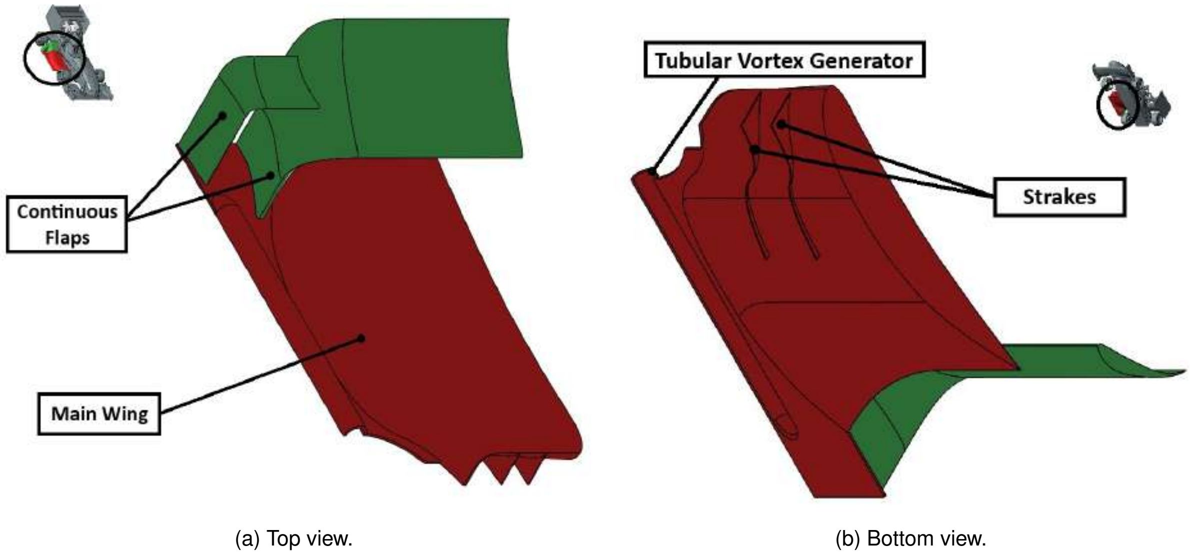

(a) Top view.

(b) Bottom view.

Figure 2.16: Configuration B - Second design of side elements.

The final design, configuration C, presented in Figure 2.17, builds upon the previous iteration, introducing several key modifications. First, the airfoil profile guiding the main wing was rotated slightly nose-up at the leading edge to better align with the incoming airflow. Additionally, the leading edge was thickened and rounded to prevent sudden flow separation on either side of the wing near this region. The 3D modeling of each main wing surface was also improved to eliminate small concavities and unintended inflection points that may have existed, ensuring seamless manufacturability.

The smaller, continuous flap introduced in the previous design was removed, as its impact on aerodynamic performance was negligible. Eliminating this component allowed for resource savings. The continuous flap geometry was further refined: its horizontal portion had its angle of attack, gap, and overlap explored, while the vertical portion was treated as a separate airfoil, with its position also analyzed. This vertical element leveraged an existing in-house mold already owned by the team, again contributing to reduced manufacturing effort and cost.

The most significant modifications were implemented on the lower surface of the main wing. Firstly, the number and configuration of strakes were adjusted. Previous numerical simulations indicated that three strakes provided the optimal balance between performance and complexity. Once this number was established, their lengths and shapes were carefully analyzed. The longer strakes were designed with the aim of generating vortices with lower pressure cores that persist over a longer distance, thereby promoting flow attachment. Notably, although three strakes are employed, only two distinct shapes are used, a deliberate decision to streamline manufacturing by minimizing the need for mold machining.

Lastly, a small yet impactful addition was made: a blend surface between the lower surface of the main wing and the monocoque, displayed in Figure 2.17c. This blend was applied only in the expansion region of the wing, an area that previously exhibited sizable separation zones, which limited downforce production. The blended surface aims to eliminate these separations, thereby increasing downforce generation.

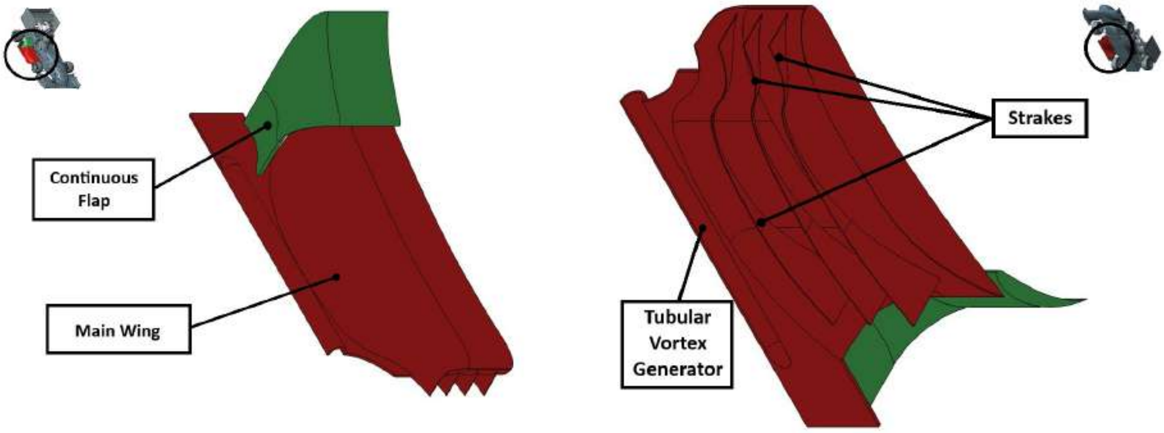

(a) Top view.

(b) Bottom view.

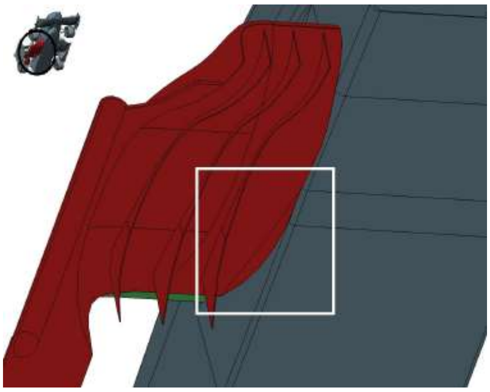

(c) Close up of the monocoque blend on the lower surface.

Figure 2.17: Configuration C - Final design of side elements.

Chapter 3

Numerical Aerodynamic Model

This chapter begins by presenting the base parameters and models that will be constant across most simulated scenarios. Then, the CFD simulations under different conditions are described and the respective mesh convergence study showcased and the numerical error estimated.

3.1 Numerical Modeling and Computational Domain

To accurately represent the physical phenomena involved, it is necessary to select appropriate mathematical models, boundary conditions, numerical solution methods, and discretization procedures for the specific type of study being conducted. A number of choices made for the CFD simulations in this work followed what was introduced in [7]. The model parameters selected in *Siemens Star CCM+*®[54] were as follows:

- Mathematical Models

  Steady: Time averaging technique is applied to define the mean flow, resulting in a three dimensional flow that is considered as steady state.

  Turbulent: A fully turbulent free stream condition was initially selected. This assumption will be further evaluated in later stages to determine whether incorporating laminar flow modeling and its transition to turbulence is necessary or beneficial in any of the scenarios analyzed in this study.

  RANS $k-\omega$ SST: To model the flow, the RANS equations were chosen. To provide closure to these equations, the two equation $k-\omega$ SST turbulence model, introduced in Section 2.4.1, was used.

- Boundary Conditions

  All y+ Wall Treatment: The all y+ wall treatment employs blended wall functions that adapt based on the local mesh resolution. It replicates low y+ wall treatment behavior when a fine layered mesh is used to resolve the boundary layer, and transitions to high y+ wall treatment in regions a with coarser mesh, providing flexibility across varying mesh densities. A deeper insight on this topic is presented later in this section.

Wall Distance: This parameter represents the distance from a cell centroid to the nearest wall surface subject to a no-slip boundary condition. It is essential for physical models that account for near wall effects. The **Implicit Tree** method was selected to compute this distance, as it performs an exact projection in real space based on a triangulation of the surface mesh.

- Material Properties

  Air with constant density and viscosity: Since the FST car operates regularly at Standard Sea Level (SSL) conditions and at relatively low speed, an incompressible gas was assumed, characterized by a constant density of $\rho = 1.225\,\mathrm{kg/m^3}$ and a dynamic viscosity of $\mu = 1.8 \times 10^{-5}\,\mathrm{Pa \cdot s}$.

- Solution Techniques

  Coupled Flow: This model simultaneously solves the conservation equations for mass and momentum, resulting in faster convergence compared to the segregated flow model, which handles these equations sequentially. However, this improved convergence comes at the cost of higher computational demand per iteration. When modeling coupled flow phenomena, it is also relevant to note the Courant-Friedrichs-Lewy number (CFL) being used, which is a dimensionless parameter that plays a critical role in ensuring the stability and accuracy of numerical simulations. It may be defined as

$$\text{CFL} = \frac{U \Delta t}{\Delta x}, \tag{3.1}$$

  With U being the flow speed, Δt the time step and Δx the spatial step (mesh cell size) [55].

  In steady state simulations, such as those presented throughout this work, although the flow field remains temporally invariant, the numerical solver typically employs a pseudo-time stepping approach to iteratively advance the solution toward convergence. Within this context, the CFL number governs the extent to which the solution is updated in each iteration. While increasing this dimensionless number can accelerate convergence, excessively high values may introduce oscillations or even lead to divergence. Consequently, the CFL number effectively acts in a similar manner to an under-relaxation factor, serving as a critical tuning parameter within the solver. In the present study, it is gradually increased over the initial 100 iterations to strike a balance between convergence rate and solution stability, as illustrated in Figure 3.1.

- Discretization Techniques

  Gradients: This model allows the user to specify both the gradient computation method and the limiter method. The Venkatakrishnan limiter [56] was selected, as it offers a good balance between numerical stability and accuracy, particularly in regions with strong gradients.

  Cell Quality Remediation: This model identifies poor quality cells based on predefined criteria, such as a Skewness Angle exceeding a specified threshold. Once these cells and their neighboring

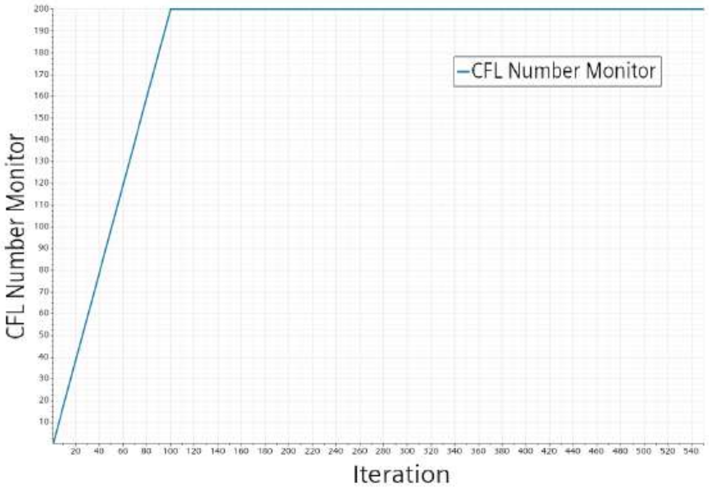

Figure 3.1: CFL number along the solver iterations.

cells are flagged, the computed gradients within them are adjusted to enhance the robustness and stability of the solution.

Numerical methods require the definition of a computational domain and a set of boundary conditions where the governing equations can be solved. The computational domain is modeled as a parallelepiped, with varying dimensions according to the specific scenario being simulated. For the on-track condition simulations, the computational domain was defined as a $50 \times 7 \times 10\ \mathrm{m}$ volume, as illustrated in Figure 3.2a, together with the corresponding reference coordinate system, where the x-axis is oriented downstream, the y-axis directed to the right of the model, the z-axis pointing upwards, and the origin located at the intersection of the front axle with the vehicle's longitudinal symmetry plane, coincident with the ground plane. To accurately model the airflow within this domain, it is essential to specify the behavior of the flow at its boundaries. This is achieved by assigning appropriate boundary conditions to each surface. In this work, only straight line simulations are considered. This allows for the assumption of symmetrical airflow behavior, enabling the computational domain to be halved. Consequently, only the right-hand side of the car is simulated, as shown in Figure 3.2b and the results are subsequently mirrored to represent the full vehicle.

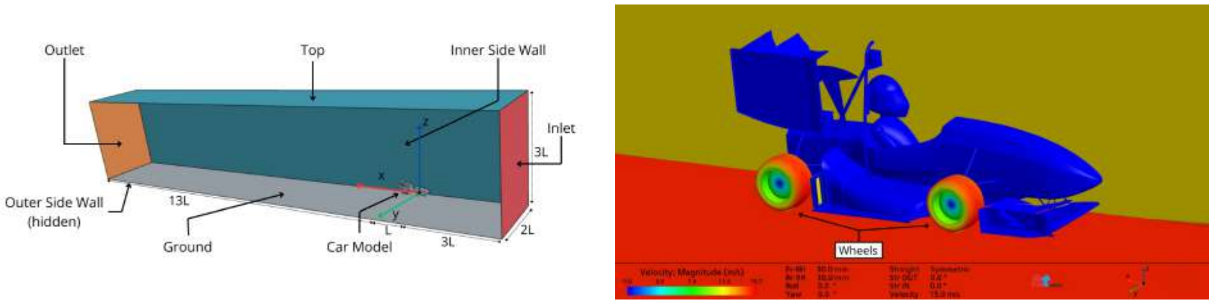

(a) On-Track simulation domain.

(b) Rotating wheels boundary condition.

Figure 3.2: Domain boundaries defined in the simulations.

The boundary conditions applied in the simulations conducted were defined as follows:

- **Inlet**: The domain inlet boundary is defined as a `Velocity Inlet`, allowing the specification of the inflow conditions. In this setup, the velocity is given by $U = U_x = U_{\text{inlet}}$, with its value varying depending on the specific simulation scenario performed. For both the on-track and the wind tunnel (WT) simulations, the inlet velocity was set to $U_{\text{inlet}} = 15\,\mathrm{m/s}$.
- **Outlet**: The domain outlet boundary was defined as a `Pressure Outlet`, where a constant static pressure was imposed to represent the outflow condition. This pressure was set to $P = 0\ \mathrm{Pa}$, defined relative to atmospheric pressure, for both on-track and wind tunnel simulations. The outlet boundary was positioned approximately 13 car lengths downstream of the model for both simulation sets, ensuring sufficient distance for the wake to stabilize before reaching it and approach the prescribed conditions, thereby reducing residuals and enhancing convergence stability.
- **Ground**: For track reproduction, the domain's bottom boundary is defined as a `Wall`, imposing a no slip condition. To replicate the moving ground effect encountered on track, this surface is assigned a velocity equal to the inlet velocity, U_{inlet}. This boundary condition is modified in simulations replicating wind tunnel conditions, in which, the wall velocity is set to zero, allowing a boundary layer to develop and mimick the actual WT experimental setup.
- **Side and Top Walls**: The remaining walls, namely, both side walls of the domain (including the one corresponding to the car's symmetry plane) and the top wall, are defined as `Symmetry Plane` boundaries for on-track conditions. This configuration prevents the development of non-physical boundary layers in these regions and more accurately reflects real-world conditions, where the car is not confined by physical walls. A `Symmetry Plane` boundary enforces zero normal gradients for all flow variables of interest, effectively functioning as a slip wall. To simulate the wind tunnel conditions, some boundaries, specifically the outer and top surfaces, were redefined as `Wall`, imposing a no-slip condition. This adjustment leads to the development of additional boundary layers, thereby providing a closer replication of the experimental environment.
- **Car**: All surfaces of the car are defined as `Wall` boundaries, enforcing a no-slip condition with a fixed wall velocity of $U = 0$ m/s. This configuration therefore ensures an accurate representation of viscous flow effects, enabling the development of boundary layers along the vehicle's surfaces. This approach is critical for accurately capturing the flow dynamics necessary for a comprehensive aerodynamic performance assessment.
- **Wheels**: For on-track conditions, the wheel surfaces are defined as `Wall` boundaries with a rotational wall motion for real-world conditions, as introduced by Carreira [7]. Each wheel is assigned an individual coordinate system with its origin located at the respective wheel center, enabling precise specification of the rotation axis. The angular velocity of each wheel is determined based on its center height and the inlet velocity specified as an input, which effectively represents the vehicle's velocity within the simulation framework. However, to accurately replicate the conditions encountered experimentally, the wheels were defined as fixed surfaces for the WT simulations, as the scale model does not incorporate rotating wheels.

Additionally, whenever required, the turbulence intensity was set to $TI = 0.01$, and the turbulence viscosity ratio was defined as $\mu_t/\mu = 10$. Furthermore, an initial condition prescribing a uniform velocity of 80% of U_{inlet} is applied throughout the entire domain to accelerate convergence.

Wall Modeling

Walls are a significant source of vorticity in most practical flow problems. Consequently, an accurate prediction of the flow and turbulence parameters across the wall boundary layer (BL) is essential. This is particularly relevant in the context of this work, where the behavior of the airflow is strongly influenced by viscous phenomena in near wall regions, such as transition and flow separation, which can have a major impact on the car's overall performance.

To accurately resolve the entire boundary layer flow, a prism layer mesh was applied to the car's surfaces, enabling the discretization of the small scale dimensions characteristic of the BL inner region [54]. This approach complements the polyhedral meshing employed throughout the remainder of the domain (further details regarding the mesh used are provided in Section 3.2). As the addition of a prism layer significantly increases the total cell count, both the prism layer height and the number of layers were adjusted based on the available computational resources and the boundary layer development along the car's length. A target y^+ value close to unity was set for these surfaces to ensure that the first prism layer lies within the viscous sublayer.

In certain regions, however, the prism layer meshing was deliberately disabled, as the boundary layers of these components were assessed to have a limited impact on the overall aerodynamic performance of the car. The separation zones associated with these parts were not expected to vary significantly, thereby justifying the reduction in cell count. The components where prism layers were omitted include the suspension arms, the wheel assemblies, the anti-roll hoop and the rear wing supports. In these areas, a traditional wall function approach, known as a high y^+ treatment, is consequently employed. Conversely, for the remaining components, a more accurate boundary layer resolution was achieved through a low y^+ treatment, made possible by the finer mesh provided by the prism layers. As a result of employing both high and low y^+ approaches, an All y^+ treatment was implemented, as shown in Figure 3.3a. The resulting wall y^+ distribution across the vehicle surfaces is shown in 3.3b, indicating an average value below 1 for the majority of the geometry, which lies within the recommended range for the wall functions employed [54].

Transition Model Assessment

At this stage, it was important to evaluate whether the implementation of a transition model was justified, particularly in the wind tunnel scenario, where the Reynolds number is considerably lower than that encountered under on-track conditions, typically in the order of 10^6.

The transition from laminar to turbulent flow is a key phenomenon in aerodynamic simulations, particularly at low Reynolds numbers, as it strongly influences boundary layer development and overall aerodynamic performance. Standard turbulence models, such as the k-ω SST, are calibrated for fully

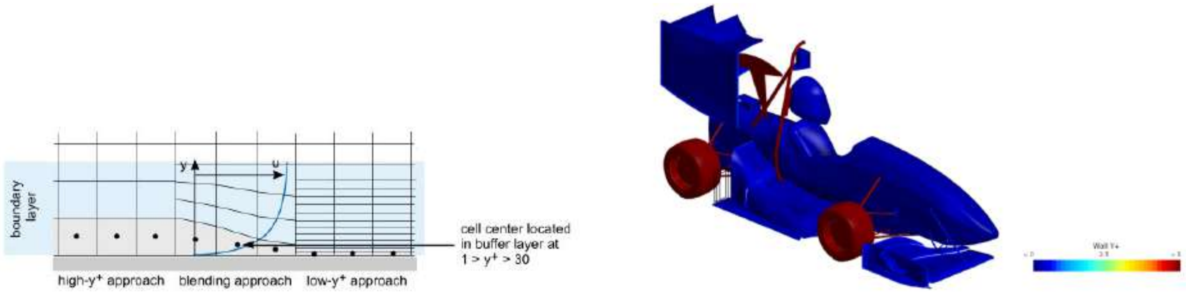

(a) All y^+ approach [54].

(b) Wall y^+.

Figure 3.3: Chosen wall modeling approach and resulting wall y^+.

turbulent flows and therefore fail to predict the onset and progression of transition without dedicated models. Neglecting this process can lead to significant inaccuracies in quantities such as skin friction and pressure distribution where transition occurs [57]. Incorporating a transition model can thus enhance modeling accuracy [58].

However, as demonstrated in [8], simulations performed under wind tunnel conditions comparable to those of the present study achieved better agreement with experimental data when no transition model was employed. Considering this, together with the characteristics of the current setup, particularly the relatively large inlet-to-model distance that promotes a thicker boundary layer, it was deemed appropriate to rely solely on the baseline turbulence model. This decision reduced both computational cost and simulation time while maintaining sufficient accuracy for the objectives of this work.

3.2 Mesh Convergence Analysis

3.2.1 Grid Generation

Despite using a simplified model, the prototype still presents a highly complex geometry. To ensure a clean and simulation-ready geometry and to avoid geometric inconsistencies, the surface wrapper feature was employed. This tool is part of the geometry preparation suite and is capable of generating clean, manifold, and watertight surfaces from a non ideal input CAD model, thereby eliminating the need for additional Boolean operations [54].

The *Star-CCM+*® software provides three primary meshers: Polyhedral, Trimmed, and Tetrahedral. In this study, the Polyhedral mesher was selected due to its ability to handle complex geometries effectively while offering high refinement capabilities when required [54]. Polyhedral meshes are relatively easy to construct and require no more surface preparation than tetrahedral meshes, while also reducing the total cell count (typically by a factor of five) compared to an equivalent tetrahedral mesh. Although the generation of polyhedral meshes can be more time-consuming, especially when compared to trimmed meshes, they often require fewer iterations to reach a converged solution [59]. This strategy produced the surface mesh illustrated in Figure 3.4.

To improve the mesh quality around the car model, several refinement regions were defined using volumetric control boxes of varying shapes and sizes. Three volumetric controls were dedicated to

Figure 3.4: Example of surface mesh on the half-domain FST car.

refining the mesh around each of the main aerodynamic components: the front wing, the side elements, and the rear wing, as shown in Figure 3.5b. These components are expected to exhibit strong adverse pressure gradients and significant vorticity, particularly on their lower surfaces; refining these areas is therefore essential to accurately resolve small scale flow features. Additionally, three more volumetric controls were introduced to gradually increase the mesh size from the car surface outward to the domain boundaries, as illustrated in Figure 3.5a.

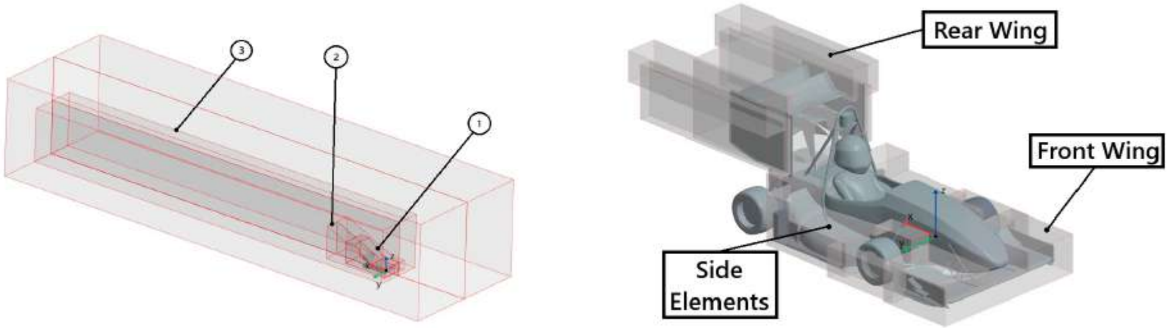

(a) Boxes around the whole car.

(b) Boxes around the aerodynamic package.

Figure 3.5: Grid refinement boxes.

3.2.2 Numerical Error

Round-off Error

The simulations in this study were conducted using a version of *Star CCM+* ® with double precision arithmetic. This implies that all variables and functions are computed using 64-bit floating point numbers, offering 14 significant digits of accuracy. As a result, it is reasonable to assume that round-off error is negligible, particularly when compared to other sources of numerical error.

Iterative Error

To ensure that the estimation of the overall numerical error, typically assumed to be dominated by the discretization error, is not compromised, the iterative error should be considerably smaller than the discretization error [60]. In this study, a total of 550 iterations were performed for the mesh convergence study and all subsequent simulations. Convergence of the solver was evaluated by monitoring the decay of the non-normalized residuals to values below at least 10^{-4}, as illustrated in Figure 3.6, together with the stabilization of the integrated aerodynamic loads, including the generated downforce and drag, whose evolution across iterations for both the total vehicle and the right side element is shown in Figures 3.7a and 3.7b, respectively.

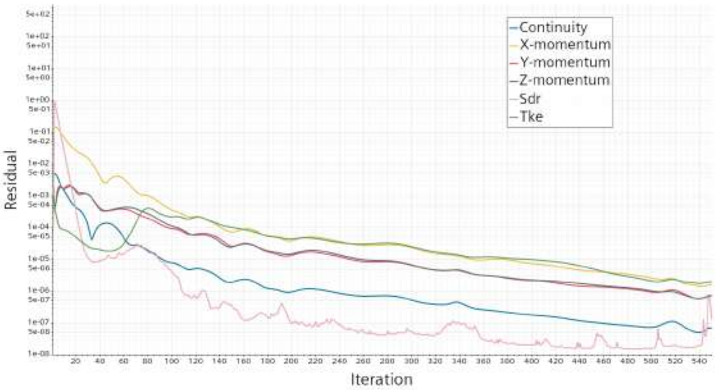

Figure 3.6: Residuals monitor.

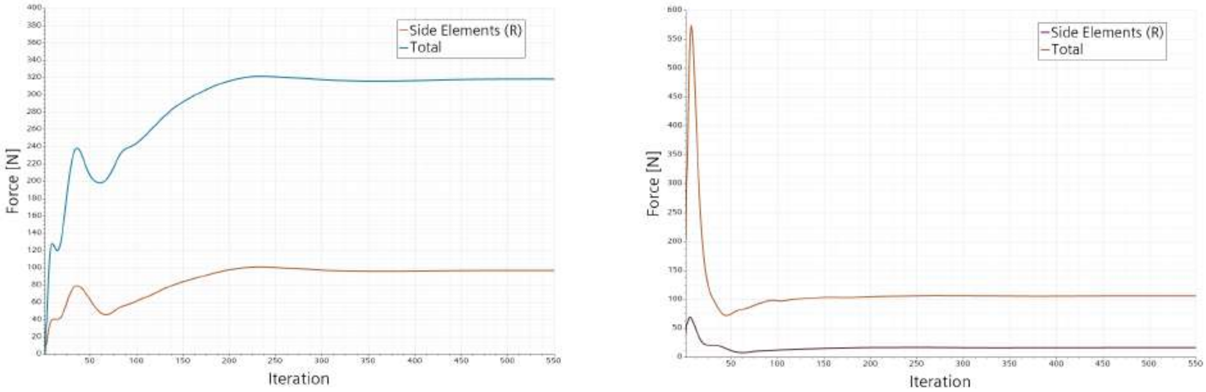

(a) Downforce.

(b) Drag.

Figure 3.7: Integrated aerodynamic load monitors for the total vehicle and for the right side element.

The results were then averaged over the final 40 iterations, and the iterative error was initially monitored by computing the standard deviation of three key variables over these same iterations: C_L, the lift coefficient; C_D, the drag coefficient; and the downforce generated by the side elements. The standard deviation values obtained were on the order of 10^{-3} in the worst case scenarios.

Naturally, iterative error can only be reduced to the level of round-off error. However, a fully converged solution up to machine precision is generally sufficient to approximate ϕ_{exact} when estimating iterative error. To facilitate this estimation, the methodology proposed in [61] was employed, allowing for a more straightforward evaluation and direct comparison with the previously computed standard deviation values. This method requires input from at least five levels of residuals, ideally equally spaced, as well as the corresponding values of the selected key variables. The output consists of power series expansions to estimate ϕ_{exact} for each variable, providing an estimate of the iterative error along with the solution down at machine-level accuracy. The resulting plots for the selected variables of interest are presented in Figure 3.8, where the five grids employed are identified by their respective typical cell size, h_i.

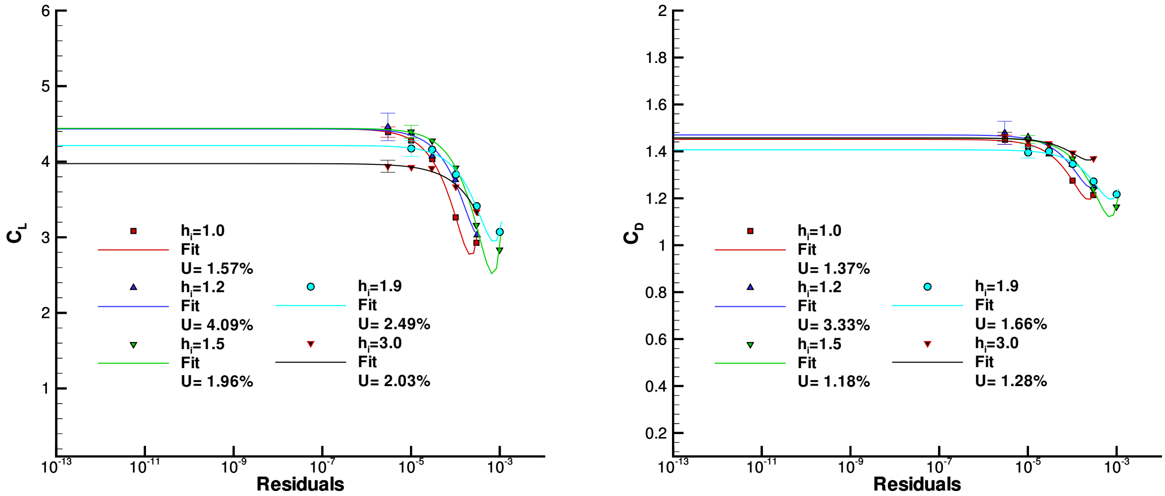

(a) Lift coefficient.

(b) Drag coefficient.

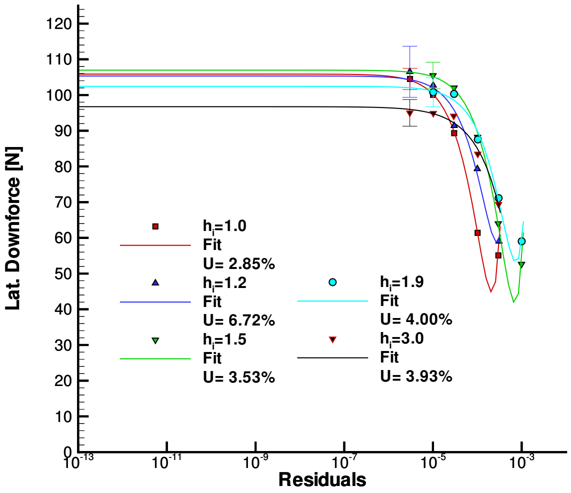

(c) Downforce from side elements.

Figure 3.8: Iterative error estimation for the five distinct geometrically similar meshes for the selected variables of interest.

As the observed standard deviation values are considerably lower than the corresponding estimated iterative errors, the latter are deemed reliable and will be used in subsequent comparisons and analyses.

Discretization Error

In this work, the discretization error was estimated using a power series expansion, following the methodology described in [60]. The approach first estimates the exact solution and then evaluates the associated error and corresponding uncertainties, which are derived from the standard deviation of each data point at high confidence levels. This approach relies on a mesh convergence study involving at least three geometrically similar grids. Five such grids were employed in the present study. To ensure geometric similarity across grids while working with unstructured meshes in a commercial meshing environment, a scaling parameter, Ri, was used across all relevant mesh controls, such as surface and volume mesh sizes, and prism layer thicknesses, allowing consistent refinement levels to be achieved efficiently [7]. The behavior of the discretization error can be described as

$$e(\phi_i) = \phi_i - \phi_{exact} = \alpha h_i^p \ , \tag{3.2}$$

where α is the error constant, p the convergence order and h_i is the typical cell size, defined by $h_i = \sqrt{\frac{N_1}{N_i}}$, where N_i represents the number of faces on the car's surface of each mesh and N_1 is the number of faces of the finest mesh.

The key variables selected for monitoring during the mesh refinement study were, again, the overall C_L, C_D, and the downforce generated by the side elements. The first two were chosen as they characterize the global aerodynamic forces acting on the vehicle and will later be used for comparison with wind tunnel test results. The side element downforce was included due to the emphasis placed on these components throughout the work. Tracking this variable across the five geometrically similar meshes provides greater confidence in the results obtained in this region and supports more reliable comparisons between different geometrical configurations.

The results obtained for the three monitored variables are summarized in Table 3.1. In addition to the aerodynamic performance indicators, the table also includes the total solver time, the memory usage of each simulation, and the number of surface mesh faces on the car model, as these parameters were considered relevant for evaluating the computational cost and mesh resolution. All simulations were performed on two different workstations: one equipped with a quad-core *Intel® Xeon® W-2123* CPU and 128 GB of RAM, and another featuring an *Intel® Core™ i7-6700K* CPU with four total cores and 64 GB of RAM, both providing sufficient computational capacity to ensure numerical stability and convergence within reasonable runtime.

Table 3.1: Mesh convergence results.

Mesh h_i	**Setup and Solver**			**Results**		
	N_i ($\times 10^5$)	Total Time (h)	Memory Required (GB)	C_L	C_D	Lat. Downforce (N)
$h_i = 3.0$	1.52	2.57	17.00	3.942	1.471	95.064
$h_i = 1.9$	3.87	3.81	27.98	4.180	1.397	100.699
$h_i = 1.5$	5.79	5.04	45.23	4.399	1.447	105.404
$h_i = 1.2$	8.98	9.24	75.33	4.455	1.475	106.387
$h_i = 1.0$	13.28	22.88	124.06	4.398	1.449	105.054

The plots generated using the previously described methodology couple the least squares error estimation method with the Richardson extrapolation to estimate the values of the selected key variables at $h_i = 0$. These extrapolated values are thus treated as the exact solutions for each variable. The estimated exact values for C_L, C_D, and the downforce generated by the side elements are 4.5836, 1.4430, and 108.33 N, respectively, as shown in Figure 3.9.

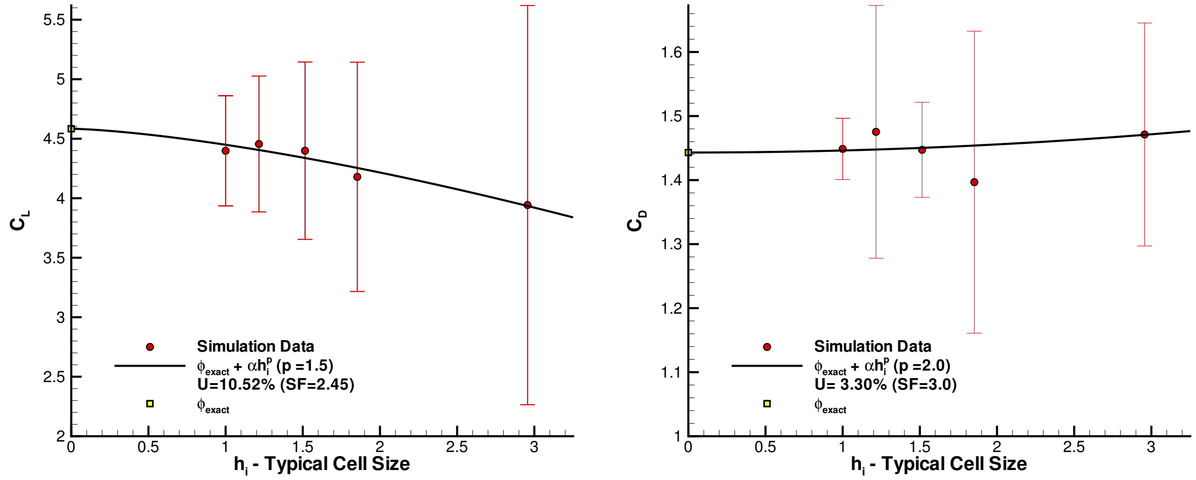

(a) Lift Coefficient.

(b) Drag Coefficient.

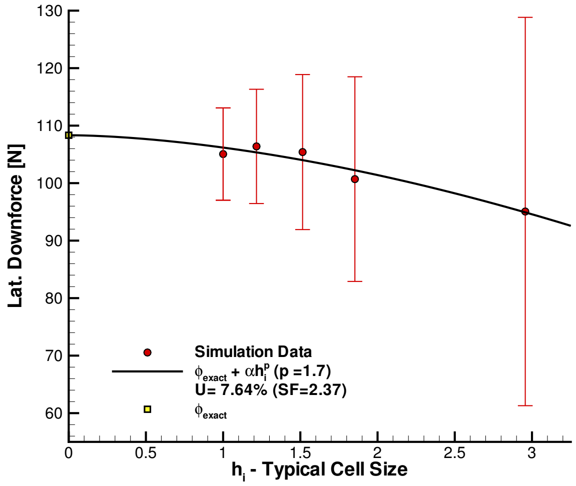

(c) Lateral downforce.

Figure 3.9: Estimated discretization error and associated uncertainties.

As expected, the most refined mesh ($h_i = 1.0$) exhibits the lowest error and uncertainty. However, both the total solver time and memory requirements for this mesh are prohibitively high, rendering it impractical for routine use. For this reason, the third mesh level, corresponding to a refinement ratio of $h_i = 1.5$, offers a good compromise between computational cost and solution accuracy. This mesh maintains adequate grid resolution around the car, enabling the capture of small scale flow phenomena that may be missed by coarser meshes.

Lastly, the uncertainties presented in the plots of Figure 3.9 result from the estimated discretization errors, which were approximately 4.29% and 1.1% for the lift and drag coefficients, respectively, and 3.2% for the downforce generated by the side elements. These uncertainties were estimated conservatively, as indicated by the high safety factors, primarily due to the data scatter observed in the results, which was expected given the geometric complexity of the problem. When comparing the iterative and discretization components, both uncertainty values were found to be calculated with high safety factors, hence, the discretization component was identified as the dominant contributor and its corresponding values are henceforth considered as the numerical error estimates. Moreover, any further attempt to reduce the discretization error to approach the iterative component would require an unreasonably fine mesh, rendering additional refinement unjustifiable in terms of computational cost.

This verification process ensured that the aerodynamic trends analyzed in the subsequent stages of this work could be confidently attributed to physical effects, such as boundary condition variations and geometric modifications, rather than numerical error. The established CFD setup therefore provided a reliable foundation for the comparative analyses presented in the following sections.

Chapter 4

Wind Tunnel Experimental Setup

4.1 Force Balance Calibration

Before initiating the calibration procedure, certain adjustments were necessary to ensure the proper functioning of the force balance. Upon installation at the work site, one of the sensing bars on the force balance was observed to be significantly bent, as illustrated in Figure B.1. This required replacing and individual calibration of the sensing bar to ensure accurate measurements, as described in Appendix B.

To estimate the aerodynamic loads acting on the force balance during the wind tunnel campaign, CFD simulations (Section 5.2) were performed under flow conditions designed to match those expected in the experimental test. The aerodynamic forces and moments obtained from the CFD simulation were rescaled to match the expected values for the $1{:}3$ model. Since aerodynamic forces such as lift and drag scale with the square of the characteristic length, they were converted as

$$F_{\mathrm{WT}} = \frac{F_{\mathrm{CFD}}}{3^2} = \frac{F_{\mathrm{CFD}}}{9} \ , \tag{4.1}$$

while moments, being the product of force and distance, scale with the cube of the characteristic length, thus

$$M_{\mathrm{WT}} = \frac{M_{\mathrm{CFD}}}{3^3} = \frac{M_{\mathrm{CFD}}}{27} \ . \tag{4.2}$$

These scaling relationships were applied to the lift, drag, and side forces, as well as to the pitch, roll, and yaw moments. The resulting estimates provide a reference for calibrating the aerodynamic balance and verifying the measurement ranges prior to the wind tunnel tests. Table 4.1 presents the numerically obtained values of the quantities of interest, namely lift, drag, and pitching moment, calculated for the vehicle configuration featuring the final side element design, configuration C. To these values, the actual weight of the scaled prototype (see Section 5.1.2) was added to the z-force component, and a safety factor of 1.5 was applied to each quantity.

Table 4.1: Expected force and moment component magnitudes.

	F_z (N)	F_x (N)	M_y (N·m)
Aerodynamic loads	-69.48	29.46	0.17
W/ model weight and safety factor	-220.94	44.20	0.26

In preparation for the wind tunnel testing phase, a complete calibration of the six-component aerodynamic balance was conducted to ensure accurate and reliable measurement of aerodynamic forces and moments acting on the 1:3 scale vehicle model. The balance consists of six aluminum bars instrumented with strain gauges, arranged to measure three orthogonal forces (F_x, F_y, F_z) and three moments (M_x, M_y, M_z). The strain signals are acquired via two *NI*™ 9237 modules, processed in real time through a *LabVIEW*™ interface, and post-processed in *MATLAB*®.

The calibration procedure was conducted in two distinct stages, following the methodology originally developed by Oliveira [4] and later refined by Pacheco [8] through the use of a new calibration apparatus. In the first stage, previously outlined, each bar was individually calibrated to determine the relationship between its strain output and the axial force it experiences. A linear regression was then used to obtain a unique calibration equation for each bar, which translates the raw strain readings into physical force units (N). This step ensures that the response of each structural element is independently characterized before they are considered as part of the full balance system.

On the second stage, a global calibration of the balance was performed to link the individual bar forces to the total aerodynamic loads acting on the model. A dedicated calibration rig, originally built by Ferreira [5] and adapted for the LNEC working environment, employed a cable and pulley system to apply known forces and moments to the support structure. By adjusting the cable routing and application points, the setup allowed precise directional control of the loads. Vertical weights generated horizontal or vertical forces as well as pure moments or combined loading conditions, depending on their attachment relative to the balance center.

To minimize hysteresis and eliminate slack in the cables, a small preload was applied before each load case, maintaining constant tension throughout the measurements. Gaps between pulley brackets and axle bars were filled to prevent unintended movement under load. The weight sets ranged from 1 N to 20 N, covering the expected aerodynamic forces and moments during wind tunnel tests. Each weight was verified on a high-precision scale (accuracy of 10^{-5} kg) and numbered before use.

Loads were applied for approximately 30 seconds while strain, and consequently axial force data, were continuously recorded. Only the most stable 15-second interval was used to compute mean values, minimizing the influence of transient effects and manual weight handling. The calibration procedure followed the methodology described by Pacheco [8]. During the initial 30 seconds, no loads were applied; all weight supports were then loaded in the subsequent 30 seconds, followed by the sequential application of each additional load case at 30-second intervals until completing the full load combination. Figure 4.1 illustrates two representative load cases.

The load cases were defined to match the aerodynamic conditions expected during testing, ensuring

(a) $-F_z$ load case with approximately 290 N in negative z direction. No moment created due to symmetrical loading.

(b) $-F_x$ with $-M_z$ composed load case with approximately 30 N employed.

Figure 4.1: Examples of load cases.

calibration under representative operating scenarios. Each sequence was repeated three times. In total, 24 combinations produced 221 individual load cases, as summarized in Figures B.10 and B.11. The resulting calibration coefficient matrix C, obtained using a relative strain approach, is provided in Figure B.12.

Unlike the original approach proposed by Oliveira [4], this work used relative strain values rather than absolute strain measurements. For each load combination, the initial zero load case served as the reference, and all subsequent strain values were offset accordingly. This adjustment compensated for baseline inconsistencies observed during initial calibrations, likely caused by temperature variations and day-to-day conditions. The same procedure was later applied during experimental testing: the zero load strain was recorded, absolute strain values converted to relative strains, then transformed into axial forces in each bar and finally resolved into resultant forces in the working coordinate system.

The calibration matrix was derived using a weighted least squares fit between the known applied loads and the measured bar forces obtained through the relative strain measurements. The load matrix emphasized the dominant test components: drag (F_x), downforce ($-F_z$), and pitch moment (M_y), while including off-axis load cases to capture cross sensitivities. These cases comprised pure forces, pure moments, and combined force-moment scenarios.

Finally, to evaluate the force balance calibration model and enable accurate interpretation of the experimental results, the model uncertainty was estimated through the propagation of the main error sources, namely the uncertainties associated with the applied masses and the balance resolution, together with the repeatability uncertainty derived from the three repetitions performed for each loading sequence. These components were combined to construct a covariance matrix of the model parameters, from which the overall uncertainty of the calibration model was obtained. The resulting expanded uncertainty, encompassing all contributing components at a 95% confidence level, was estimated at approximately $1\ \mathrm{N}$. The detailed characterization of the calibration model for the force balance used was conducted by Lopes [62] following the described methodology.

4.2 Data Acquisition

The experimental measurements relied on two dedicated data acquisition systems to record the aerodynamic loads and surface pressures on the scaled model. The aerodynamic forces and moments from the balance were acquired using two *National Instruments®* *NI* 9237 modules (Figure 4.2a), known for their high precision in strain gauge and bridge based measurements. Each module provides simultaneous, high resolution input channels with integrated excitation, which minimizes wiring complexity and ensures stable and low-noise signal capture. For this test campaign, the bridge signals were sampled at an actual frequency of $1613\ \mathrm{Hz}$ and averaged in blocks of 100 samples, yielding an effective output rate of $16.13\ \mathrm{Hz}$ with no additional digital filtering applied. Time averaging of these $16.13\ \mathrm{Hz}$ records was then performed to obtain the desired data values.

Surface pressure data were obtained using a *Pressure Systems®* ESP 64HD pressure scanner (Figure 4.2b), a 64-channel electronic pressure scanning system widely employed in wind tunnel testing. This device integrates on-board temperature compensation, reference calibration, and fast multiplexing, allowing reliable sampling of all taps with minimal drift. In the present work, pressure channels were sampled at $5\ \mathrm{Hz}$ and averaged at each operating condition to obtain mean pressures.

(a) *NI* 9237 strain gauge meter.

(b) Pressure Systems™ ESP 64HD pressure scanner.

Figure 4.2: Data acquisition hardware.

4.3 Wind Tunnel Characterization

All experiments were performed in the low speed, closed circuit wind tunnel at LNEC, shown in Figure 4.3. The WT is $L = 3.0\mathrm{m}$ long and it has a rectangular test section with $W \times H = 1.2 \times 1.0\mathrm{m}$. [63]. Flow speed is continuously variable; acceptance tests reported a nominal top speed $\approx 49\ \mathrm{m\,s^{-1}}$ with an empty tunnel [64], while the current facility note specifies operation up to $45\ \mathrm{m\,s^{-1}}$. During the experimental campaigns, airspeeds ranged from $U_\infty = 15$ to $17\ \mathrm{m\,s^{-1}}$..

Starting upstream of the test section, the WT comprises four turning corners, two diffusers, a settling section with flow straightening screens, and a $4{:}1$ contraction leading into the test section. After passing through the test section, the flow is gently decelerated in a two-stage diffuser and routed through two guide-vane corners. An axial fan then accelerates the stream, after which a conical diffuser conditions the discharge before the remaining corners steer the flow back toward the settling section. As illustrated

Figure 4.3: Aeronautical wind tunnel at LNEC.

in Figure 4.4, each corner is equipped with a bank of 21 sheet steel guide vanes. The central vanes in corners 3 and 4 are braced, and corner 2 contains a streamlined strut. Immediately downstream of the final corner, the duct expands to its maximum diameter, where two screens are installed: a protective electro welded steel grill with square mesh and a fine brass turbulence reducing screen. A short quieting section then transitions into the sheet metal contraction, delivering a uniform, low turbulence core into the test section. Only the closed wall configuration was used in the present study, although the facility allows side window removal to operate as an open test section [63].

The test section incorporates radiused wall fillets that progressively increase in thickness downstream to accommodate boundary layer growth. A controlled circumferential gap of approximately $20\ \mathrm{mm}$ at the downstream end of the test section helps maintain the flow near ambient static pressure during operation. Integrated lighting and large removable observation windows provide full optical access to the test section. Additionally, the balance support arm enters the test section approximately $2.2\ \mathrm{m}$ downstream of the inlet [63].

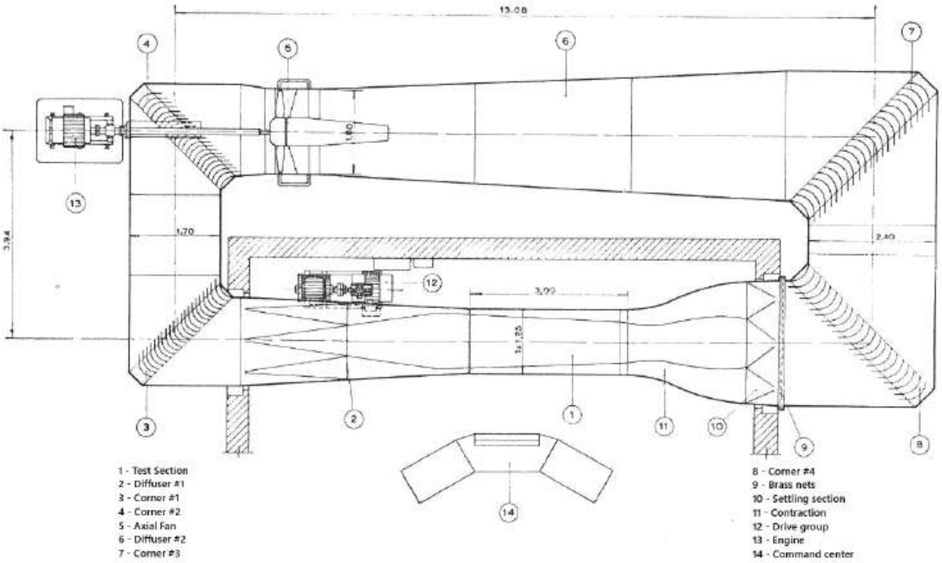

Figure 4.4: Schematic of the LNEC aeronautical wind tunnel [63].

The test section area is $W \times H = 1.20\ \mathrm{m}^2$. With the scaled model giving a frontal area of approximately $A_f = 0.126\ \mathrm{m}^2$, the blockage ratio is

$$\beta = \frac{A_f}{WH} = \frac{0.126}{1.20} = 10.5\%. \tag{4.3}$$

Classical closed wall corrections were not applied in this work. Instead, interpretation relied on CFD performed in a domain reproducing the tunnel's closed wall environment and model ride height, so the reported results are specific to the WT configuration used.

The WT drive group consists of an axial fan with twelve individually adjustable blades followed by a nine vane straightener designed to remove swirl and recover static pressure. The facility employs variable frequency drive (VFD) control for the fan, enabling smooth, continuous frequency adjustment and gentle acceleration/deceleration ramps. During this campaign, the blade pitch was kept fixed, and test speeds were set by commanding the fan rpm via the VFD and verifying the resulting free stream speed against the facility's Pitot tube at the test section centerline [64]. The test section exhibits a baseline turbulence intensity below 1%; in fact, acceptance measurements reported $TI \approx 0.78\%$ at the centerline ($x \approx 2\ \mathrm{m}$) [65].

The relationship between fan frequency and test section speed is essentially linear at fixed blade pitch, which allows repeatable set pointing of U_∞ [64]. In practice, fan frequency as rpm served as the primary control variable, while the Pitot reading provided the reference for logging and fine trim near each target speed.

4.4 Testing Procedure and Limitations

The experimental procedure adopted in this study followed the sequence illustrated in Figure 4.5. Initially, the force balance was secured in place and the support arm adjusted to the prescribed yaw angle and nominal ground clearance. The model, already configured with the intended geometry, was then installed in the test section and attached to the balance. Ground clearance was measured and documented. If any aspect of the setup, such as attachment points, ride height, or yaw angle, deviated from the intended configuration, the model was removed, the discrepancies corrected, and the installation repeated.

Once the mechanical setup was verified, the data acquisition chain was activated, comprising two NI modules interfacing with the six-component balance, the pressure scanner, and the pre-existing thermometer within the test section. The wind tunnel was then gradually accelerated to approximately $15\ \mathrm{m\,s^{-1}}$. Under this condition, it was essential to confirm that the wheels did not contact the floor and that the configuration remained stable.

Before defining the final operating point, temperature stability in the test section was verified. If thermal equilibrium had not yet been achieved, the tunnel was allowed to run until the temperature stabilized. Once stable, the target free stream velocity was calculated based on the desired Reynolds number, Re_{CFD}, matching that used in the numerical simulations under SSL conditions, and using the instantaneous air properties:

$$U_{\text{target}}(T) = \frac{Re_{\mathrm{CFD}}\, \mu(T)}{\rho(T)\, L}, \tag{4.4}$$

and the fan frequency was iteratively adjusted until the Pitot-measured speed matched U_{target}.

The instantaneous air properties were computed as functions of the measured temperature. First, the air density ($\mathrm{kg\,m^{-3}}$) was determined from the ideal gas law,

$$\rho = \frac{p}{RT}\ , \tag{4.5}$$

where p corresponds to the atmospheric pressure ($\approx 101325\ \mathrm{Pa}$) and R is the specific gas constant for air ($\approx 287.05\ \mathrm{J\,kg^{-1}K^{-1}}$) [19]. Second, the dynamic viscosity ($\mathrm{Pa\,s^{-1}}$) for the given temperature was obtained from the Sutherland's formula:

$$\mu(T) = \mu_{\mathrm{ref}} \left(\frac{T}{T_{\mathrm{ref}}}\right)^{3/2} \frac{T_{\mathrm{ref}} + C}{T + C}, \tag{4.6}$$

where μ_{ref} is the reference dynamic viscosity ($1.8{\cdot}10^{-5}\ \mathrm{Pa\,s}$) at the reference temperature $T_{\mathrm{ref}} = 293.15\,\mathrm{K}$ (20°C), and C is Sutherland's constant ($110.4\ \mathrm{K}$) [19, 66].

Data acquisition proceeded in a fixed sequence. Forces and moments were recorded first to establish the zero offset during post-processing. After a 1 min stabilization period to allow the balance to stabilize, pressure measurements were initiated. Each run lasted 5 min under steady conditions, enabling five one-minute data sets per run. For each configuration, three consecutive runs at the target condition were conducted to assess repeatability and to provide sufficient raw data for reliable statistical averages. Runs were repeated whenever the desired speed could not be reached or maintained, sensor errors were detected, or the operator observed anomalies.

The balance support arm and the wind tunnel floor attachments can locally disturb the flow and introduce unwanted effects, particularly near the ground, an area critical to capturing the aerodynamic behavior of interest. Since the geometry, model incidence, and yaw were held constant throughout the entire test matrix, the influence of the balance arm support exposed to the incoming airflow largely cancels when comparing differences between configurations.

To reduce hysteresis in the multi-component balance, the model was removed from the balance at the end of each tested configuration. As balance zero offsets may drift over long campaigns, zero aerodynamic load readings were verified between run groups to monitor measurement accuracy.

Ambient temperature also posed a significant challenge during the experimental campaign. Conducted in summer, the campaign was subject to room and test section temperatures considerably higher than the numerical reference conditions. Exactly for this reason was the temperature logging approach employed for each run and used to compute the corresponding target free stream speed, ensuring that the intended Reynolds number was maintained despite variations in air properties.

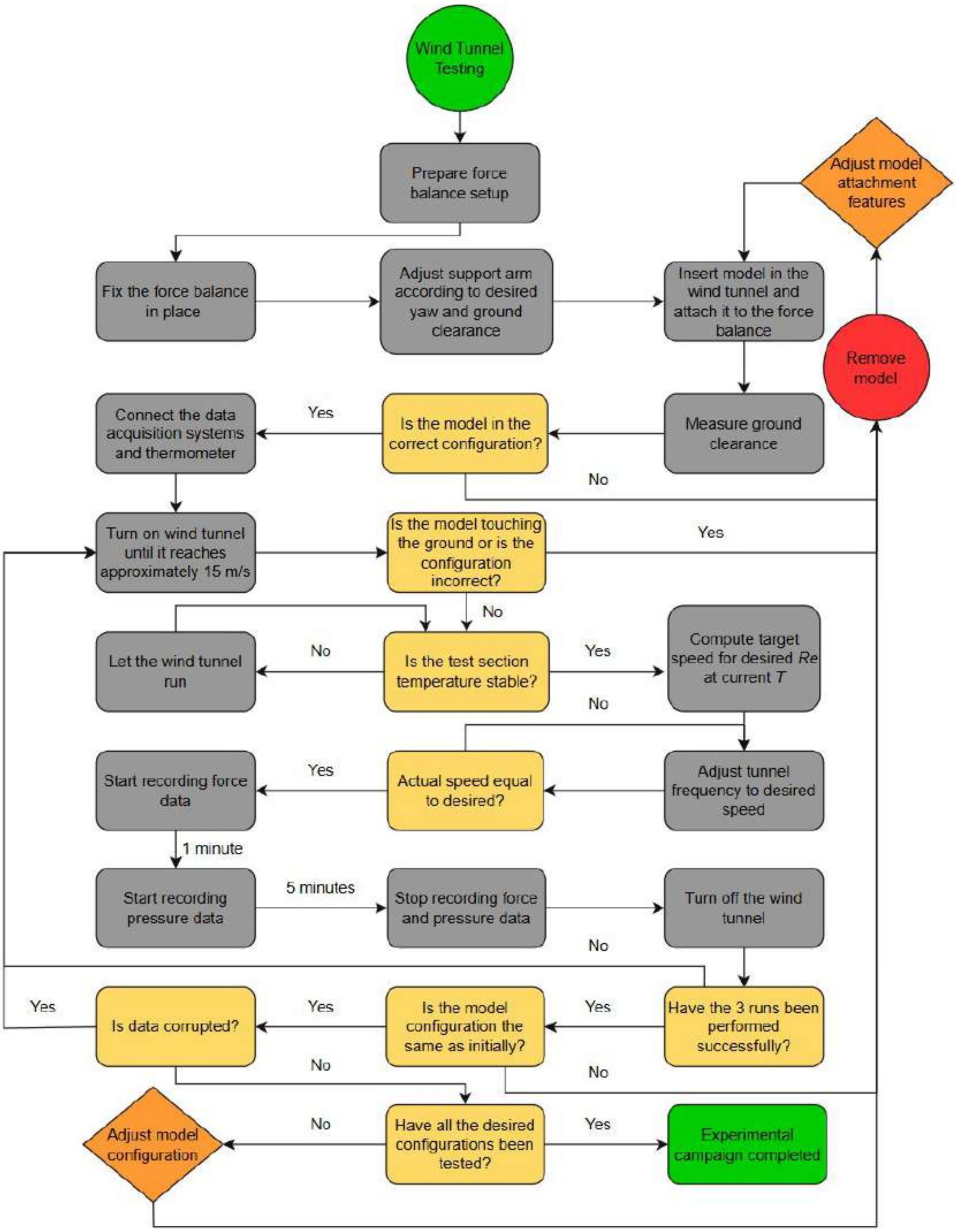

Figure 4.5: Wind tunnel testing procedure.

Chapter 5

Wind Tunnel Testing and Comparison with CFD Simulations

5.1 Formula Student Scaled Model

This section outlines the key decisions made in developing the scaled FST car model for the experimental campaigns, including the definition of its scale, its manufacturing process, and its attachment to the force balance.

5.1.1 Flow Similarity and Scale Definition

Reynolds Similarity

In WT experiments, the presence of a model within the airstream perturbs the surrounding flow field, generating measurable aerodynamic forces. The magnitude and distribution of these forces depend on both the geometry of the model and the properties of the airflow, including velocity, density, and viscosity. To ensure that WT measurements provide a representative approximation of full scale vehicle behavior, dimensionless similarity parameters that capture the fundamental characteristics of the flow must be guaranteed [17]. Among these parameters, the Reynolds number,

$$Re = \frac{\rho V L}{\mu} \ , \tag{5.1}$$

where V and L are the reference speed and length, respectively. Re quantifies the relative influence of inertial and viscous effects and it is one of the fundamental parameters that determines the flow regime, whether laminar, transitional, or turbulent. Achieving Reynolds similarity between the model and the full scale vehicle requires adjusting the free stream velocity in accordance with the characteristic length of the model, under the assumption of constant fluid properties: $V \propto \frac{1}{L}$. Proper scaling in this manner ensures that the dimensionless aerodynamic forces measured in the WT are representative of those experienced by the vehicle under real operating conditions [67].

Scale Definition

The scale of the WT model was determined through an evaluation of the competing constraints of aerodynamic similarity, WT capabilities, manufacturability, and measurement quality. In principle, a full scale Formula Student car would provide the closest similarity; however, such a model cannot physically fit within the LNEC closed section wind tunnel [63]. This immediately rules out full scale testing and motivates the use of a reduced model.

At the opposite extreme, very small scales, such as 1:4 or 1:5, would easily fit into the test section with minimal blockage, but the resulting Reynolds numbers would be much lower than that of the real car, even at the tunnel's maximum operating speed of $45\ \mathrm{m/s}$. Consequently, the flow regime obtained in the WT would differ from that on-track, potentially leading, for example, to laminar separation on the front wing of the model. Furthermore, the aerodynamic forces scale with L^2 so, at smaller scales, they would approach the resolution limits of the aerodynamic balance, amplifying relative uncertainty and measuring errors. These drawbacks make very small scales unsuitable for meaningful comparisons between experiments and simulations.

The 1:3 scale emerges as the most balanced solution. At this size, the projected frontal area corresponds to an acceptable blockage ratio, as shown in Figure 5.1 and estimated in Section 4.3. The Reynolds number achievable at the tunnel's operating limit is significantly higher than for smaller scales, placing the flow in a regime where key aerodynamic mechanisms are preserved with reasonably good fidelity. The forces generated by the model are expected to be above the sensitivity threshold of the balance, reducing measurement uncertainty and enabling reliable coefficient determination. Simultaneously, the model is compact enough to be manufactured within the project's available time and resources, yet large enough to reproduce fine geometric features such as cascade profiles, diffuser strakes, and inlet details without requiring further unrealistic thickening or simplification. Besides aerodynamic and facility considerations, the 1:3 scale also offers practical advantages for instrumentation and modularity. Pressure taps and tubing remain feasible to be installed given the available volume inside the parts, while structural stiffness is sufficient to suppress aeroelastic deformation under tunnel loads. The scale is compatible with the mounting hardware and balance system already available, which reduces rigging complexity and allows interchangeable modules to be tested efficiently.

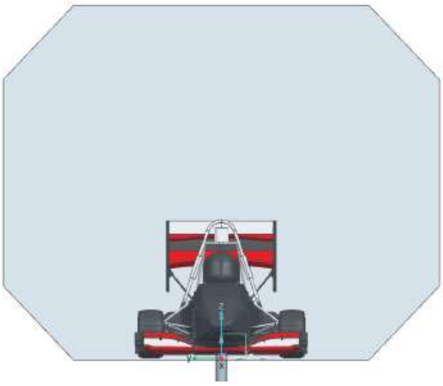

Figure 5.1: Scaled FS model inside the WT test section (frontal view).

Wind Tunnel Free Stream Speed

As previously noted, the maximum speed of the wind tunnel is $45\ \mathrm{m/s}$, which would, in theory, allow for Reynolds number similarity with on-track conditions, given that the FST14 averages a speed of $15\ \mathrm{m/s}$ during competition. However, for the experimental campaigns, the airspeed was lowered to $15\,\mathrm{m/s}$. This choice was motivated by several factors: preliminary tests revealed that the WT was unable to maintain stable temperatures throughout extended operation, and, as reported in [8], higher velocities could induce vibrations that would compromise the accuracy of the force balance measurements. Operating at a lower velocity would mitigate both vibration and temperature fluctuations while ensuring that the scaled model could safely withstand the generated loads, which would have been almost one order of magnitude (9 times) higher at $45\ \mathrm{m/s}$. Given that the model scale was already determined, Reynolds similarity with full scale on-track conditions could not be achieved. Nevertheless, similarity of Reynolds number between the wind tunnel experiments and the CFD simulations is maintained to allow meaningful comparisons.

Model Position in the Wind Tunnel

The placement of the scaled model inside the WT is constrained by its geometry. The balance support arm could only be installed at a predefined location, approximately $2.2\,\mathrm{m}$ downstream of the test section inlet, as seen in Figure 5.2. Although this distance had to be respected, positioning the model closer to the inlet would have been preferable. A shorter upstream distance would limit the growth of the wind tunnel wall boundary layers before reaching the model, thereby preserving a larger region of uniform core flow in the test section. On the other hand, the existence of a turbulent boundary layer on the bottom wall upstream of the model guarantees that the flow around the front wing is mainly turbulent, helping to maintain consistent flow conditions between simulations and experiments. Thus, the model was mounted at the fixed longitudinal location. In order to ensure consistency with numerical simulations, the car was positioned transversely at the centerline of the test section, thus maintaining symmetry, as displayed in Figure 5.1.

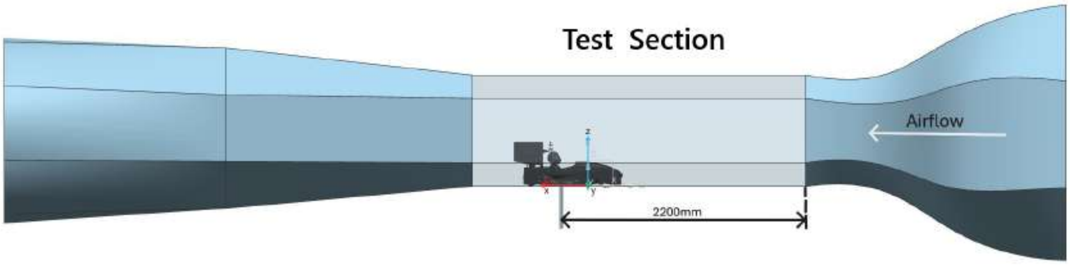

Figure 5.2: Scaled FS model inside the WT test section (side view).

Regarding vertical positioning, the objective was to place the model at the lowest possible height, constrained by the requirement that the wheel contact patches must not touch the wind tunnel floor to ensure that the aerodynamic forces were only transmitted to the force balance rather than dissipated through ground contact. This setup ensures that both the wheels and the aerodynamic components remain as close as possible to the ground, reproducing the proximity effects observed under real track conditions. To meet these requirements while preventing physical contact, the model wheels were initially set to be elevated by $5\ \mathrm{mm}$ above the WT ground. Ultimately, the experiments and simulations are compared under conditions that differ from actual race track operation in several aspects: Reynolds number (scale effects), ground clearance, non-rotating wheels, stationary ground, and the boundary conditions at the lateral and top walls of the wind tunnel (blockage effects). The influence of all these factors is analyzed using CFD in Chapter 6.

5.1.2 Modeling and Manufacturing

Geometry Preparation

The preparation of the scaled model geometry began with the simplified representation of the FST14 previously introduced in Section 2.5. From this baseline, the geometry was adapted to ensure both manufacturability and proper assembly. This process involved splitting the vehicle into several separate components, further splitting larger elements where necessary, and designing appropriate mounting systems, the outcome of which is shown in Figure 5.3a. Additional modifications included the incorporation of fastener holes and small fixation elements (highlighted in cyan in Figure 5.3b), the design of fitting mechanisms, and the addition of auxiliary parts to reinforce critical joints (highlighted in yellow in Figure 5.3b), ensuring that the model could withstand the loads expected near connection points. All modifications were designed to minimize their impact on the airflow around the model.

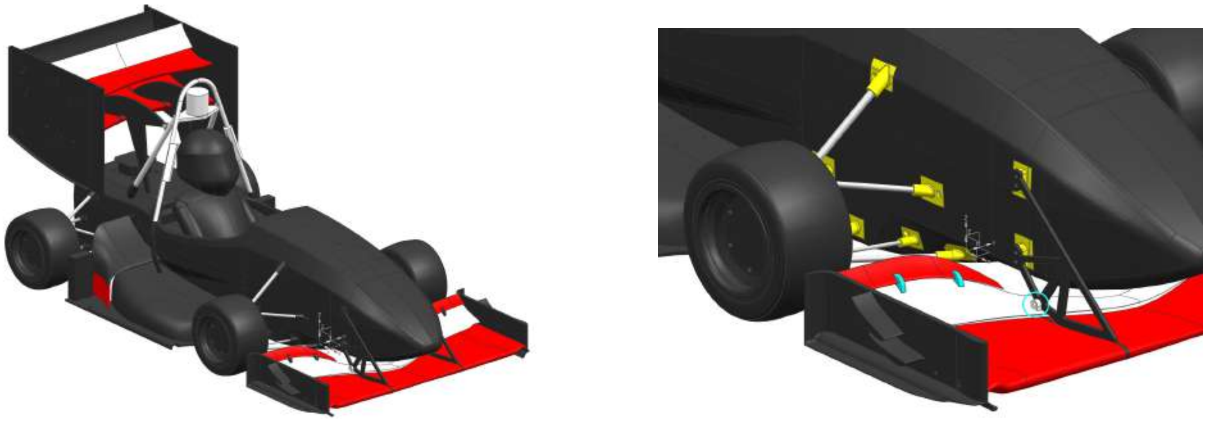

(a) Overall view.

(b) Highlights of some geometry modifications.

Figure 5.3: WT Scaled FS car model geometry preparation.

Compatibility for Pressure Readings

Surface pressure measurements provide insight into the airflow around aerodynamic appendages, enabling direct comparisons with numerical simulations and thus validating the numerical models. In the present study, pressure taps were installed on the main wing of the side elements. To accommodate these taps and route the associated silicone tubing, these elements were manufactured as hollow structures. Additionally, the chassis, divided into five separate parts, was designed as a hollow structure to accommodate the pressure scanner (Section 4.2), which can be accessed both through the removable driver cockpit and through a detachable rear lid. This design also facilitates overall model assembly and accessibility by enabling easier access to attachment points and also allows the mounting interface with the force balance arm to be housed inside the model.

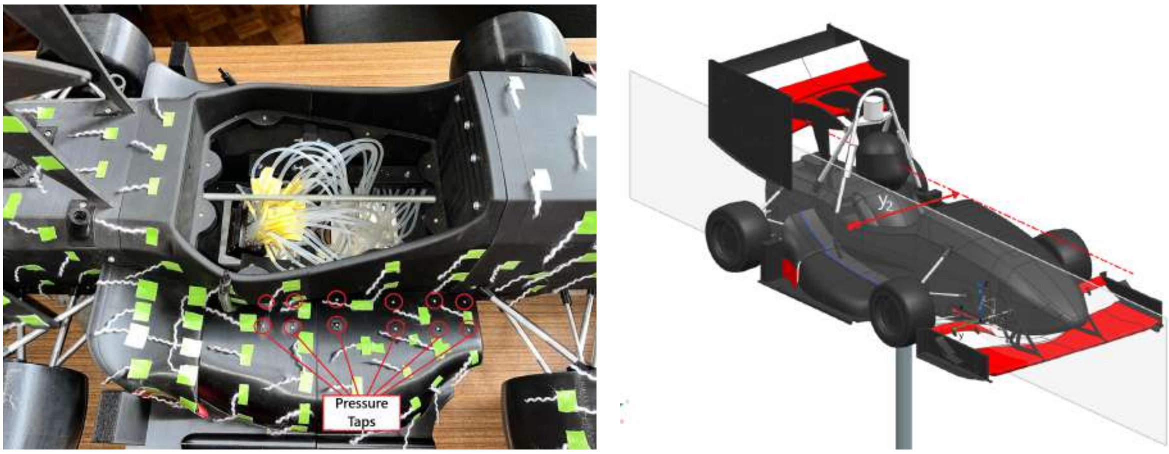

(a) View of upper surface taps on right side element.

(b) Example of spanwise pressure tap section plane ($|y_2|/(w/2) = 49\%$).

Figure 5.4: Pressure taps on WT model.

Concerning the placement of the pressure taps, it was chosen to instrument both left and right wings of the prototype, covering both the upper and lower surfaces, where a subset can be observed in Figure 5.4a. Two chordwise planes were instrumented per wing, with the spanwise coordinates differing between the left and right sides, resulting in a total of four measurement planes. This configuration takes advantage of the symmetry of the straight line condition being tested, with each side occupying half of the measurement space. Positioning the pressure taps along chordwise planes allows the pressure distribution along the wing chords to be captured in 2D plots, enabling direct comparisons with the corresponding planes in the numerical simulations. By sampling pressure at multiple spanwise locations, it is possible to reconstruct the pressure gradient at various key points along the surfaces, providing critical insight into the local aerodynamic behavior.

The four measurement planes were positioned at $y_1 = 89$ mm and $y_2 = 117$ mm on the right wing, and at $y_3 = -102$ mm and $y_4 = -129$ mm on the left wing. These spanwise coordinates represent the distances from the scaled model's symmetry plane and correspond to approximately 38%, 49%, 43%, and 55% of the car's half width, $w/2$, respectively. The selected locations ensure a balanced distribution of pressure measurements across the constant airfoil region of the wing. For reference, the main wing extends laterally from about 33% to 97% of the car's half width. For all planes considered, pressure taps were installed on both surfaces of the wing at 5%, 15%, 30%, 50%, 65%, and 80% of the chord length in each of the three configurations under study, resulting in a total of 48 pressure readings per configuration. The chordwise distribution was defined based on insights from the numerical simulations.

A higher resolution of taps was applied in the compression region to better capture the suction peak behavior, while the remaining taps were spaced more evenly to capture the subsequent expansion phase of the flow. A summary of the pressure tap positioning is presented in Appendix C.

Design Features

The design of the scaled model followed a modular approach, aiming to maximize flexibility. The model is divided into several assemblies, each composed of multiple parts, as illustrated in Figure 5.5. While this increases the overall complexity of both the design and manufacturing process, it allows individual components to be replaced or reassembled without the need to rebuild entire sections. An illustrative example of the benefits of this modular approach is found in the region of the side elements. In this area, the monocoque features a dedicated slot designed to accommodate the main wing of each configuration, which is then fastened to an internal tab. For the corresponding flaps, the monocoque incorporates an oversized rectangular cavity. This solution allows the flaps to be manufactured with this standardized rectangular base, enabling different wing geometries to be inserted into the cavity and subsequently fastened in place.

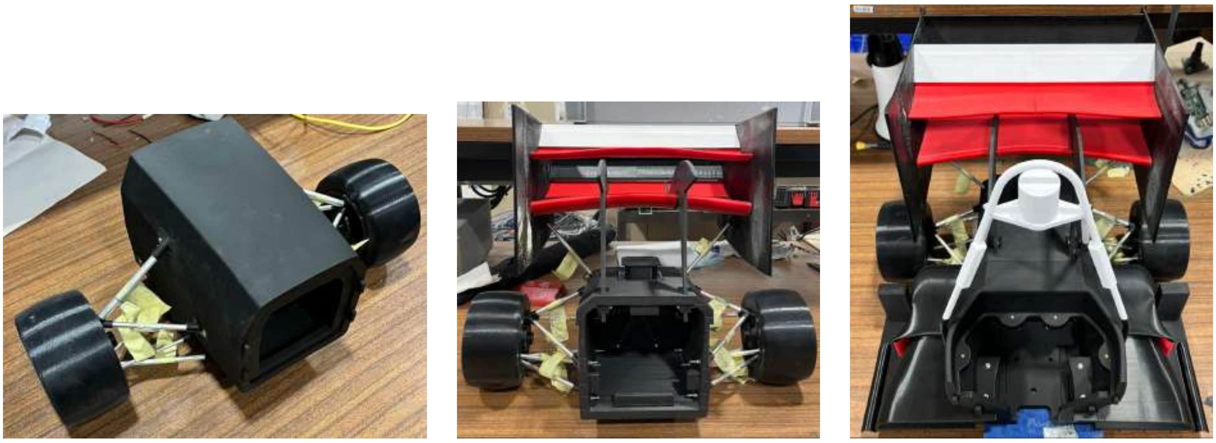

(a) Front axle section.

(b) Rear axle section with rear wing.

(c) Rear end of the model.

Figure 5.5: Model modular features.

Next, the CFD estimated pressure center of the model was selected for the attachment point to minimize moments (pitching, rolling, or yawing), thereby preventing undesired changes in the model's attitude and avoiding the measurement of erroneous force components. Under on-track conditions, the pressure center continuously shifts with changes in vehicle attitude and flow conditions. However, for the purposes of this study, the CoP was assumed to remain approximately fixed and not undergo significant variations under steady state WT conditions.

The pressure center of the model was determined using the numerical simulations performed, specifically from the final side element configuration. The CFD software includes a feature for calculating the center of loads, which identifies the point where the resultant of the aerodynamic forces is expected to act. This calculation requires reference planes or input surfaces that intersect the line of action of the resultant force. With at least two such references, it is possible to define the line of action of the aerodynamic resultant force. Considering the geometric constraints of both the wind tunnel and the model's desired height, and in an effort to minimize the flow disturbance caused by the force balance mounting, the attachment point was sought to be located inside the model. While this choice increases the complexity of the model and the number of additional components required for the experimental campaign, it provides a more representative setup. To compute the resultant force line of action, two reference planes were used: $z = 0$, corresponding to the ground plane, and $z = 111\ \mathrm{mm}$, which was selected as it approximates the center of gravity of the FST14 prototype based on the team's mass distribution data. These two planes were chosen as they define the limiting positions of the anticipated attachment point.

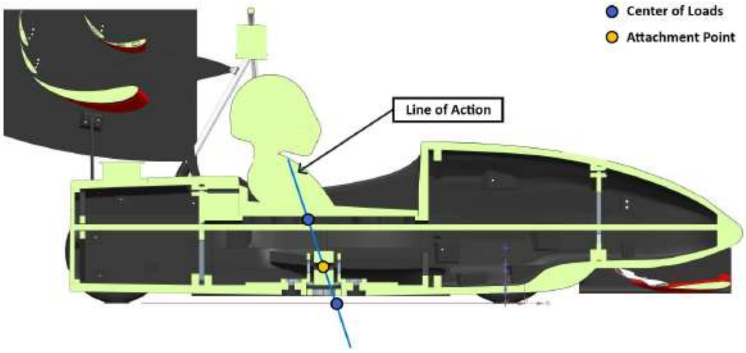

Figure 5.6: Attachment point of FS model to force balance.

Figure 5.6 illustrates the obtained resultant force line of action. This line is drawn along the symmetry plane of the car, taking advantage of the experimental symmetry. Together with this symmetry consideration, the line enables the precise definition of the attachment point, set with the desired elevation of the model of $5\ \mathrm{mm}$ above the wind tunnel floor. Once the attachment point was defined, the actual mounting system was designed. A more detailed description of the mounting system used in this study is provided in Appendix C.

Regarding the adjustability of the scaled model, modifications are possible both in its geometry and in its overall attitude. Geometrically, the angle of attack of the rear wing flaps can be adjusted analogously as in the full scale prototype, functioning as a DRS for the model if a low drag configuration is desired. Concerning model attitude, both the ground clearance and the pitch of the car can be slightly adjusted by using washers to improve correlation with the numerical results (further information in Appendix C). With respect to yaw control, the balance itself enables rotation of the support arm, thus allowing the entire prototype to rotate and enabling side wind experiments. Finally, components such as the suspension arms and the front wing supports can be indirectly adjusted by replacing the intermediate fitting elements (highlighted in yellow in Figure 5.3b), which are easily and quickly manufactured. This approach enables modifications to both the suspension geometry and the front wing height.

Manufacturing Process

The predominant manufacturing process was 3D printing, which accounted for approximately 75% of the components. Several materials were employed, including Polylactic Acid (PLA), Polyethylene Terephthalate Glycol (PETG), PETG reinforced with carbon fiber, and Polyamide High-Temperature

(PAHT) filament reinforced with carbon fiber. The aerodynamic package was entirely produced using 3D printing, primarily due to its complex geometries and the time constraints of the present work, while still achieving acceptable surface finish levels. The overall printing process required 583 hours, corresponding to roughly 24 days in total.

To ensure both quality and time efficiency, as well as maximize consistency across components, most of the parts directly exposed to the incoming airflow, such as the aerodynamic elements and the monocoque sections, were printed using *Bambu Lab*® printers [68]. The remaining components, typically smaller or supporting parts where surface finish was less critical and longer print durations were acceptable, were manufactured on *Prusa Research*® machines [69]. Specifically, the *Bambu X1 Carbon*™ and the *Original Prusa*™ *MK3S+* from the *iStart Lab* Técnico were employed for these purposes. In addition, the rear wing endplates were printed on a *Raise 3D Pro3*™, as their size exceeded the build volume of the aforementioned printers [70]. Each of the printers was operated using its dedicated open source slicing software, which converted the geometries into layers and generated the corresponding *g-code*: *Bambu Studio*™ (v2.1.1), *Prusa Slicer*™ (v2.9.2), and *ideaMaker*® (v5.3.1 Beta). Each printed component was manufactured with specific settings according to its purpose; further details are provided in Appendix C.

In total, more than 700 hours of printing time were dedicated to the model's manufacture, including both finished parts and unsuccessful or incomplete prints. This process consumed approximately $10\ \mathrm{kg}$ of PLA, $1\ \mathrm{kg}$ of PAHT-CF, $1\ \mathrm{kg}$ of PETG, and $0.5\ \mathrm{kg}$ of PETG-CF. In the end, the completed prints were sanded to further improve surface quality where necessary, particularly for components exposed to the incoming airflow.

The remaining components consisted of steel threaded rods and aluminum rods. The steel rods were cut to size and inserted into some of the model wings to increase robustness, while the aluminum rods were trimmed and sanded to fit their designated locations, serving mainly as suspension arms. The use of aluminum in this area provided the necessary strength while limiting the additional weight introduced by metallic components.

Final FST14 Model

The final FST14 WT 1:3 scaled model had a total weight of $7.93\ \mathrm{kg}$ and was composed of 138 components, excluding fasteners and accessories such as nuts and washers. Figure 5.7 illustrates the fully assembled model without the pilot lid component, providing an overview of the components used in its assembling.

5.2 Comparison of Pressure Distributions on the Side Diffuser

Following the procedure described in Section 4.4, the WT campaign comprised nine runs in total, three for each side element configuration. Apart from the side element changes, no other modifications were made to the vehicle to enable direct comparisons between configurations. The intended attitude of the car was set to yaw, pitch, and roll angles of 0°, with the tire contact patches positioned at a height

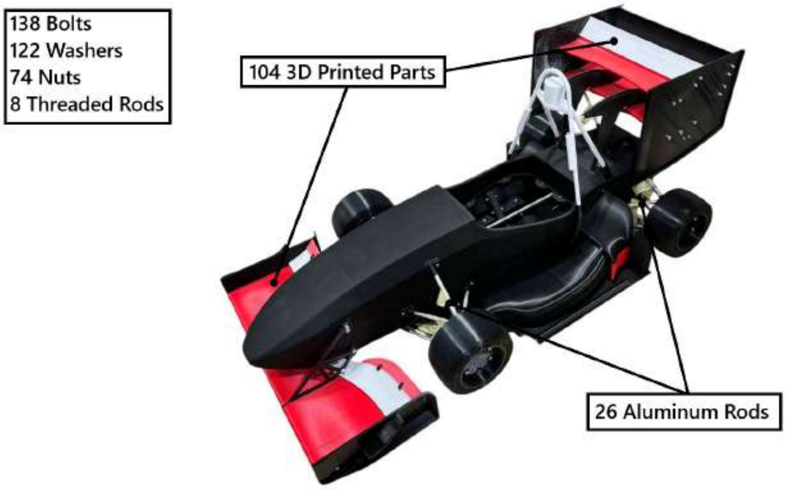

Figure 5.7: Final FST14 model.

of $5\ \mathrm{mm}$. The incoming airflow Reynolds number was maintained as closely as possible by controlling the tunnel airspeed, targeting the conditions encountered at a reference velocity of $15\ \mathrm{m\,s^{-1}}$ and a temperature of $15°C$.

As a starting point, the pressure readings were compared with the corresponding numerical results in Figure 5.8, which illustrates the pressure distribution on the upper and lower surfaces of the main wing of the side elements for configuration A at the section plane $|y_2|/(w/2) = 49\%$ of the scaled model. This comparison provides an initial assessment of the flow features that are successfully captured during the experimental campaign and those that are absent relative to the numerical conditions simulated.

These plots show that, on the upper surface, the measured static pressure values fall well within acceptable agreement with the numerically obtained results. This agreement is further reinforced by the observation that the pressure distributions on this surface, under the different conditions tested, exhibit approximately the same behavior, which was consistently captured during the experimental campaigns. On the lower surface, however, the agreement is weaker: the measured values exhibit a suction peak located further downstream than in the as-designed numerical predictions, with a considerably lower intensity.

To investigate these discrepancies, additional numerical simulations were performed. First, the model height was increased from $5\ \mathrm{mm}$ to $8\ \mathrm{mm}$ to assess whether the suction peak intensity would decrease; indeed, it rose from approximately $C_p \approx -1.9$ to $C_p \approx -1.6$ (comparing the blue and green data sets in Figure 5.8b). Subsequently, a realistic pitch variation of the car was introduced numerically by setting the axle height difference to $8\ \mathrm{mm}$ instead of the previous $0\ \mathrm{mm}$, corresponding to a nose-up rotation of $\theta = 0.893°$. Under this condition, the suction peak shifted downstream from $x/c \approx 36\%$ to $x/c \approx 45\%$.

These findings suggest that the car's attitude during testing was likely not maintained constant, and that accurately quantifying such effects would require active and precise measurement at each corner of the model. Moreover, differences in transition control between the numerical simulations and the wind tunnel setup, together with the presence of an imperfect stationary ground and the resulting mismatch between the experimental and simulated boundary layer profiles at the vehicle's front, may have con-

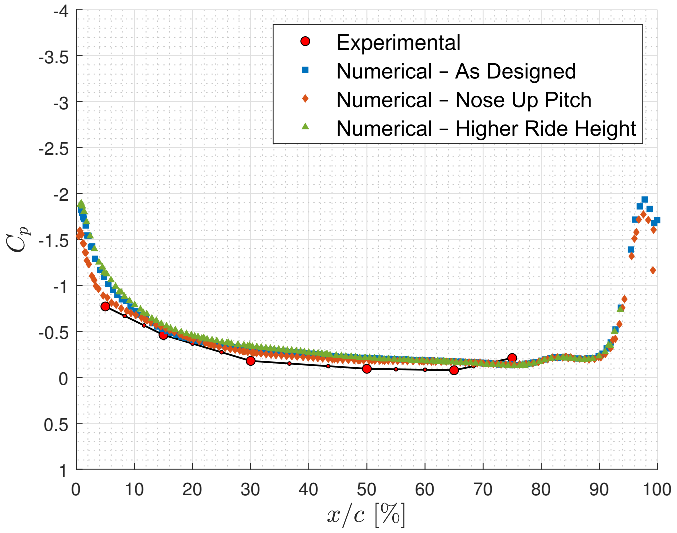

(a) Upper surface at $|y_2|/(w/2) = 49\%$.

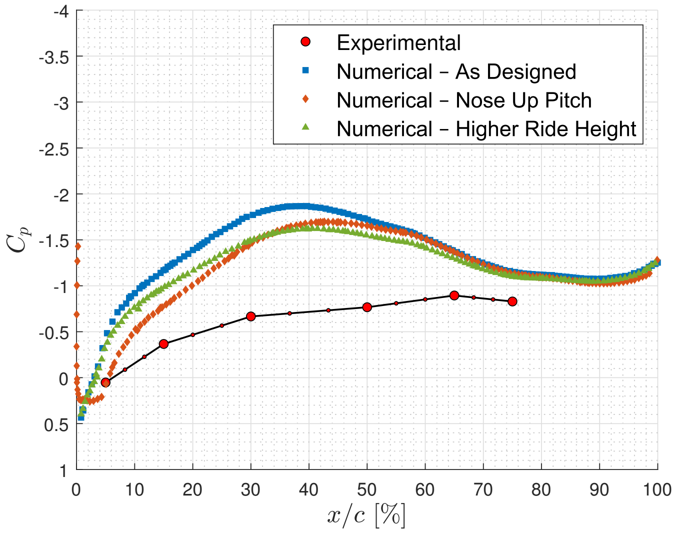

(b) Lower surface at $|y_2|/(w/2) = 49\%$.

Figure 5.8: Pressure distributions obtained experimentally and numerically for configuration A.

tributed to the attenuation and downstream displacement of the suction peak on the lower surface. In addition, the small portion of the force balance arm exposed to the incoming airflow beneath the car model, along with the corresponding slot on the wind tunnel floor, may have further disturbed the flow behavior in this region. Nonetheless, the observed trends with the geometric modifications help explain the differences between the as-designed numerical static pressure predictions and the experimental results, increasing confidence that the numerical simulations capture the essential performance trends and aerodynamic behavior. Similar conclusions were drawn from the pressure distributions of the remaining configurations B and C and spanwise sections (y_1,y_3,y_4), further corroborating these observations.

To further assess the influence of dynamic attitude changes in the results, the experimentally observed trends between configurations were compared with those predicted at the nominal as-designed neutral attitude, as well as with cases in which the model attitude was deliberately varied. The objective was to assess whether such changes would significantly alter the values expected experimentally, thereby reducing confidence in the predicted results. Since the exact model attitude during WT testing could be guaranteed, this comparison also serves to evaluate whether deviations can be reconciled with the as-designed numerical predictions. Accordingly, Figure 5.9 presents the key aerodynamic coefficient ratios for configuration B relative to configuration A, allowing a direct comparison of whether the trends vary significantly. The ratios are shown for the experimental results, the as-designed numerical simulations, and the numerical cases with increased ride height and with a nose-up pitch rotation.

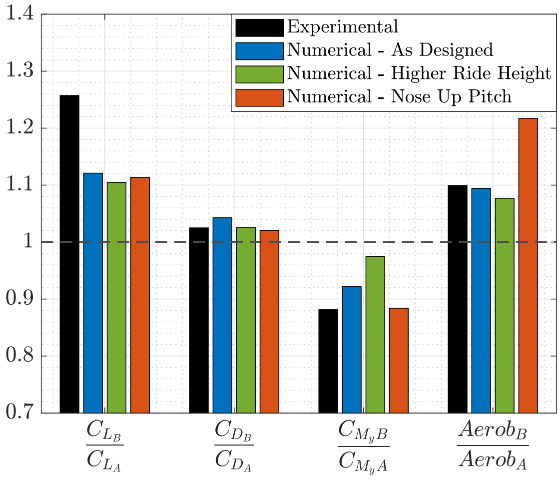

Figure 5.9: Sensitivity of aerodynamic coefficients of configuration B relative to configuration A with ride height and pitch angle.

Across the different numerical conditions, the largest variations within a given aerodynamic coefficient remained below 15%, while the overall trends were preserved within an acceptable range. This indicates that attitude changes within the tested intervals do not severely compromise the results. The main exception was observed for the aerobalance, which exhibited a noticeable shift under pitch variation, a result that is expected, since pitching directly alters the longitudinal position of the model's pressure center. Nevertheless, the consistent behavior observed across these comparisons reinforces confidence in the robustness of the as-designed numerical data and its alignment with the experimental measurements.

Overall, the comparison between the experimental and numerical results demonstrates that the simulations capture the dominant aerodynamic trends with reasonable accuracy, particularly for drag, where confidence is highest given the minimal sensitivity to attitude changes. Lift predictions, while systematically lower in magnitude, remain consistent in trend and thus still provide reliable comparative insight. The most attitude sensitive quantities were the pitching moment and the resulting aerobalance, where small deviations in ride height or pitch can significantly alter the load distribution. The fact that the height-modified case produced the closest agreement to the experimental balance strongly suggests that minor installation effects in the wind tunnel, rather than fundamental modeling limitations, are responsible for most of the observed discrepancies. Taken together, these results certify the use of the as-designed numerical setup as a robust baseline, while also highlighting the importance of considering realistic platform variations when comparing with experimental data.

5.3 Comparison of Aerodynamic Coefficients

The evolution of the aerodynamic coefficients across the three side element configurations are illustrated in Figures 5.10a and 5.10b for the absolute and relative values of C_L and C_D, and Figures 5.11a and 5.11b for C_{M_y} and the aerobalance. Normalization with respect to configuration A not only simplifies the interpretation of performance differences but also provides a clearer basis for assessing the consistency between numerical predictions and experimental measurements.

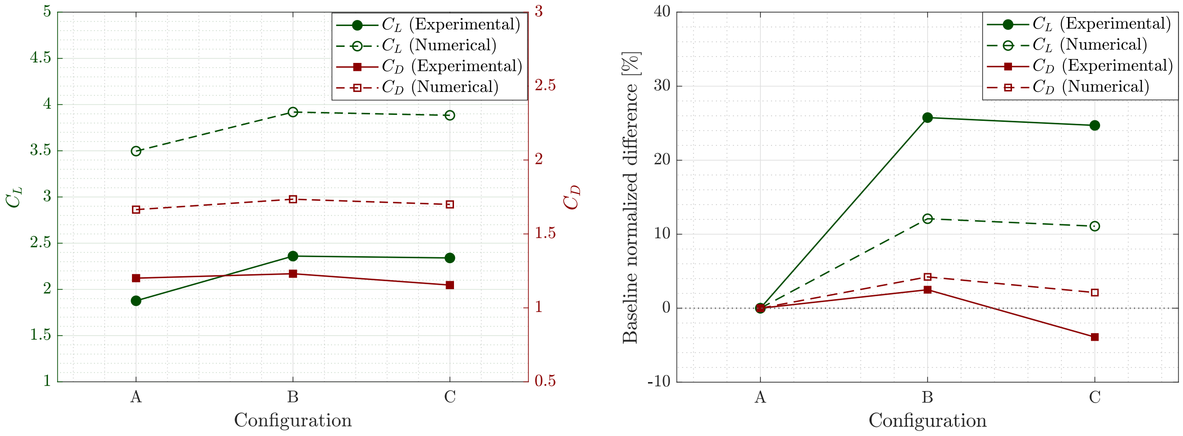

(a) Absolute values.

(b) Normalized values.

Figure 5.10: Lift and drag for the three tested configurations.

The lift and drag coefficients for the three tested configurations, shown in Figure 5.10, exhibit consistent tendencies between numerical and experimental results. From configuration A to B, both datasets indicate a marked increase in C_L, hinting that the side wing modifications indeed enhance downforce generation under the tested conditions. This improvement is accompanied by a moderate rise in C_D. For configuration C, the downforce seems to slightly decrease relative to B while still exceeding the baseline, with a partial recovery of the drag penalty. These trends are consistently captured in both datasets, and despite some discrepancies in absolute values, the simulations demonstrate strong reliability in reproducing the experimental tendencies.

The pitching moment coefficient and the aerodynamic balance, presented in Figure 5.11, exhibit analogous tendencies. Experimentally, the progression from configuration A to C reveals a reduction in the nose-up pitching moment, indicating that the side element modifications redistribute loads in a manner that alleviates rear axle demand. The numerical results reproduce this trend with only minor deviations in magnitude. Likewise, both approaches capture the forward shift in load distribution introduced by configuration B, which becomes slightly more pronounced in configuration C.

Overall, these findings show that the relative aerodynamic behavior observed experimentally across configurations is consistently reproduced numerically. Under the controlled conditions of the wind tunnel, the agreement in trends identifies the numerical setup as a reliable tool to inform guide subsequent aerodynamic development.

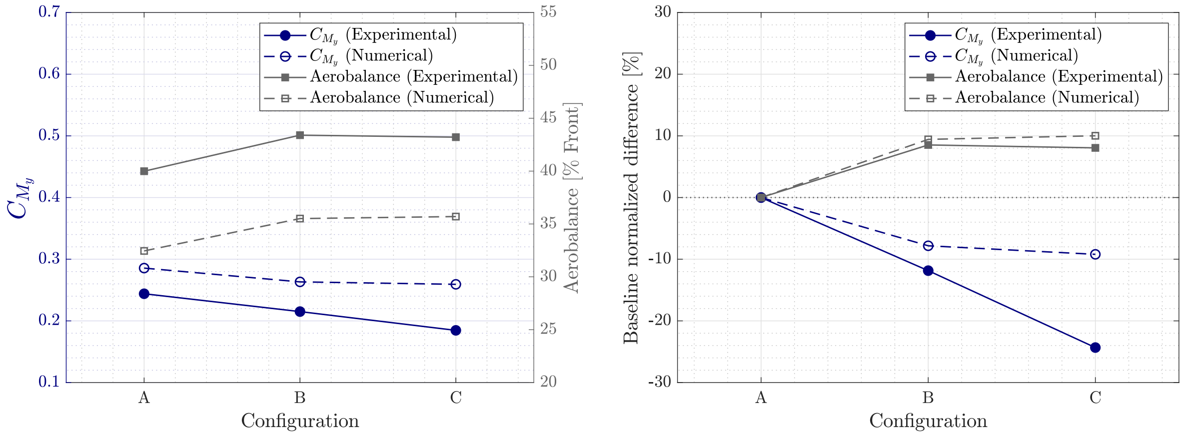

(a) Absolute values.

(b) Normalized values.

Figure 5.11: Pitching moment and aerobalance for the three tested configurations.

5.4 Flow Visualization

At this stage, the focus was on establishing correlation and building confidence in the numerical methodology, which forms the basis for later quantitative comparisons between configurations. In addition to the experimental analysis presented so far, wool tuft visualization was employed to qualitatively assess the aerodynamic behavior of individual components, thereby complementing the global force and moment measurements. Tufts were attached to the right side of the model, and the flow was recorded using two complementary devices: an action camera placed inside the test section downstream of the model to capture its rear, and a high-resolution digital camera positioned outside the test section for close up surface views. Visualizations were carried out for all three configurations simultaneously with the force and pressure measurements. Although the overall aerodynamic behavior of the vehicle was qualitatively assessed, particular attention was directed toward the side elements, as these were the focus of the development, while the global flow behavior served to further evaluate the reliability of the numerical predictions.

The comparison between EFD and numerical predictions rely mainly on the x-axis skin friction coefficient, C_{f_x}, with surface streamlines overlaid. In these plots, red regions ($C_{f_x} > 0$) represent attached flow, while blue regions ($C_{f_x} < 0$) indicate separation. It should be noted that, as turbulence is highly non-linear, evaluating single frames from the recordings requires caution, some transient effects visible in video sequences may not appear in still images. In contrast, the numerical results represent a time-averaged solution.

5.4.1 Side Element Configurations

In Figures 5.12a and 5.12b, region 1 highlights the region near the leading edge of the main wing, where the flow remains attached on the inboard section close to the monocoque but appears separated further outboard. This behavior is consistent with the numerical predictions. Region 2 also indicates a notable correlation: on the footplate surface the flow is separated, whereas above the tubular vortex generator it appears attached to the model surface. In Figures 5.12c and 5.12d, considerably smaller separation zones are predicted numerically in this region, and this behavior is well captured experimentally, with the surface streamlines appearing coherent as well. A direct comparison between configurations A and B in the region displayed in Figure 5.12 further highlights that the later configuration exhibits noticeably reduced separation, suggesting a more stable flow field, improved load consistency across the surface, and potentially lower drag, thereby indicating a more effective aerodynamic performance of configuration B.

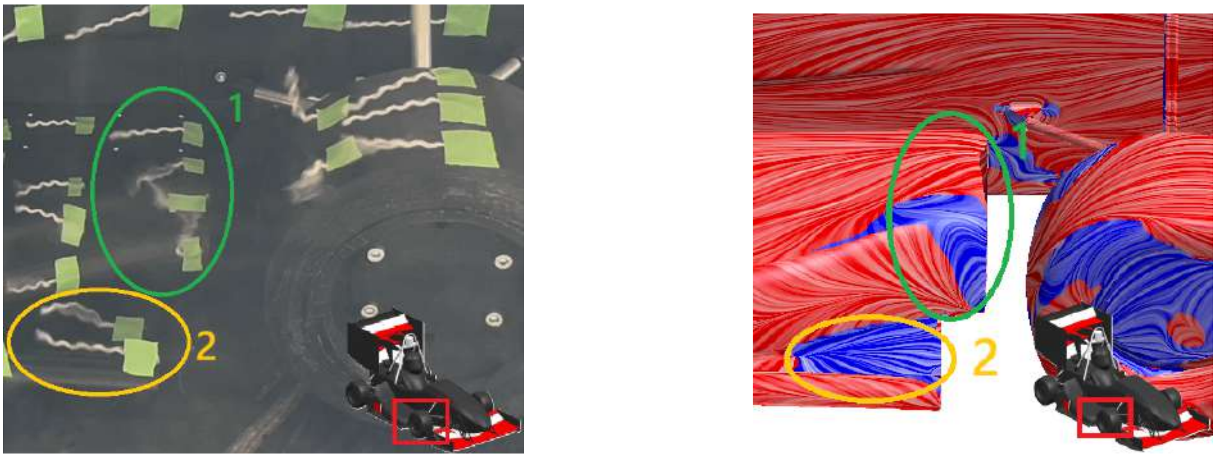

(a) EFD - Configuration A.

(b) CFD - Configuration A.

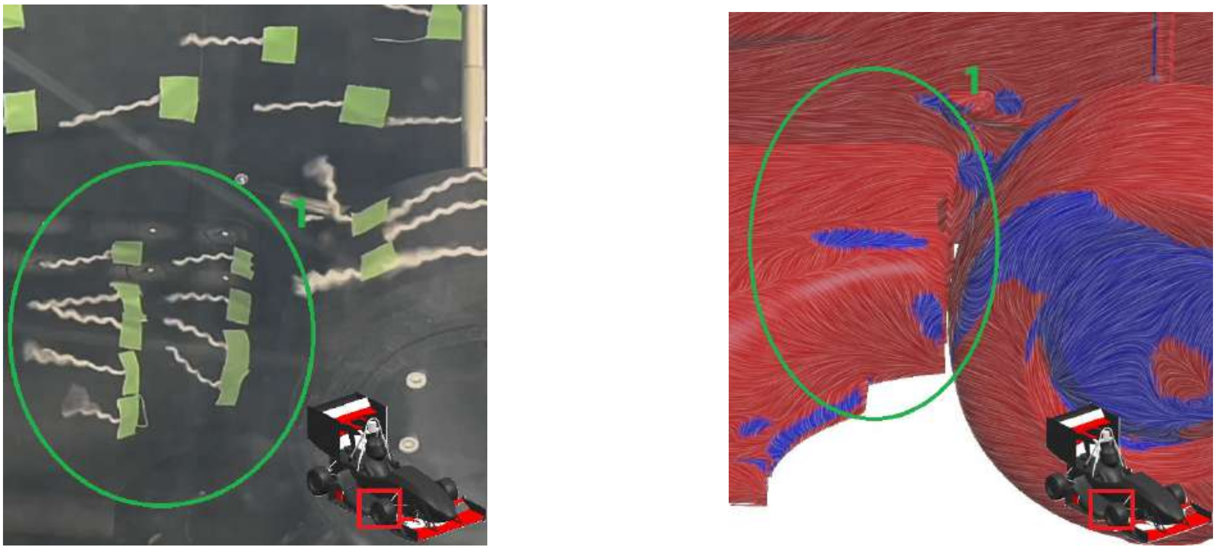

(c) EFD - Configuration B.

(d) CFD - Configuration B.

Figure 5.12: Flow visualization on main wing leading edge upper surface - Configurations A and B.

In Figures 5.13a and 5.13b, region 1 corresponds to the leading edge of the midplate, where both experimental and numerical results consistently indicate a clear separation zone. Notably, close to the footplate, the tuft orientation even suggests local flow reversal, with a tuft pointing upstream. Region 2 shows strong agreement between surface streamlines, capturing the outwash generated by the front wing upstream. The intensity of the outwash diminishes closer to the monocoque, a trend also reproduced in the numerical simulations. Furthermore, region 3 highlights the trailing edge of the midplate, where the flow exhibits a clear upwash motion. This behavior is consistently observed in both the experimental tuft visualization and the numerical simulations.

For configuration B in Figures 5.13c and 5.13d, no significant longitudinal separation zones were obtained numerically in this area, and this was consistently observed experimentally, with no major separation regions developing. The surface streamlines also exhibited strong agreement between the two approaches. Region 1 highlights a divergent streamline pattern on the upper surface of the continuous flap, which is similarly captured in both CFD and EFD. Conversely, region 3 shows a convergent flow behavior on the upper surface of the smaller continuous flap around the radiator, once again well reproduced by the experimental tuft visualization. On the main wing upper surface, region 2 illustrates outwash behavior as the flow develops downstream, a tendency evident in both methods.

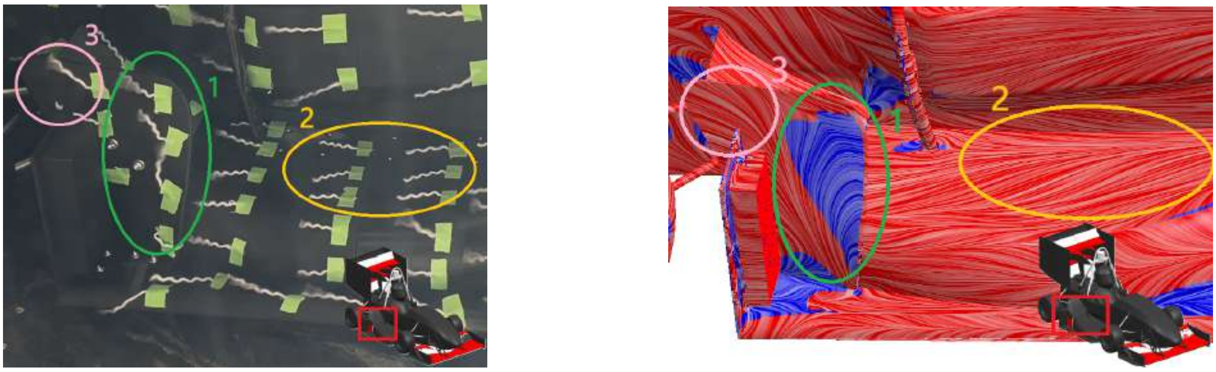

(a) EFD - Configuration A.

(b) CFD - Configuration A.

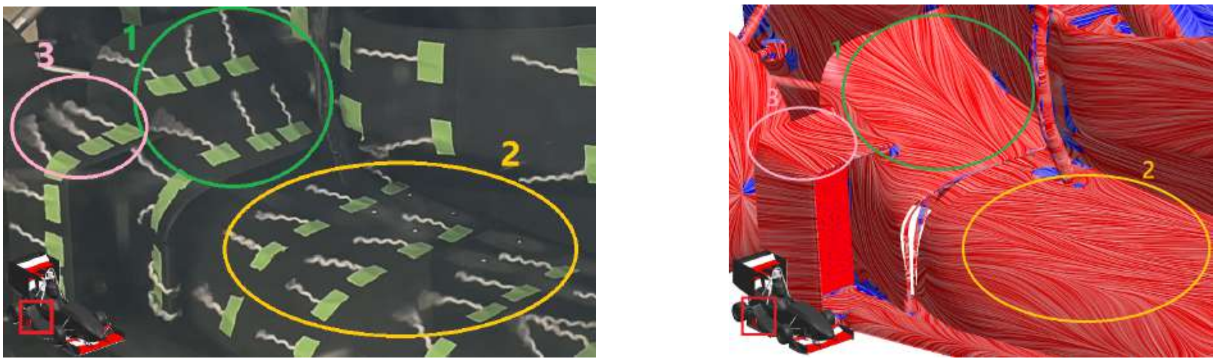

(c) EFD - Configuration B.

(d) CFD - Configuration B.

Figure 5.13: Flow visualization on main wing upper surface, midplate and flaps - Configurations A and B.

Altogether, the streamline patterns on the upper surfaces for all configurations are reproduced with good accuracy across all observable surfaces, in line with the pressure measurements discussed in Section 5.2, where numerical and experimental pressure coefficients showed agreement in this area. Configuration C exhibited comparable flow behavior throughout, with streamline patterns matching between experimental and numerical results, leading to the same conclusions.

When comparing the configurations, a clear distinction emerges between configuration A and configurations B and C in the present analysis. Configuration A exhibited pronounced separation zones, particularly on the midplate, footplate, and at the leading edge of the main wing, whereas configurations B and C showed no significant separation in either the numerical or experimental analyses. This contrast highlights a clear aerodynamic improvement, as the evolution from configurations A to B/C effectively suppressed large scale separation and promoted more coherent surface flow structures. These differences emphasize the design advantage of the later configurations in stabilizing the flow around the side elements and enhancing overall aerodynamic efficiency.

However, it is important to note that the side elements of the car are positioned immediately downstream of the front tires and are therefore directly influenced by their turbulent wake, which is inherently unsteady. In contrast, the numerical results are obtained from time-averaged solutions of the Navier-Stokes equations, which do not capture the full instantaneous behavior of the flow. Moreover, the wool tufts themselves filter out high-frequency perturbations due to their length, meaning that small-scale separation zones may not even be observable during the experimental campaigns. These aspects represent some of the inherent limitations of the present analysis and highlight the need for caution when drawing conclusions based solely on this data.

5.4.2 Other Elements

Besides the main focus of the present study, flow visualization was also performed on other aerodynamic elements of the car.

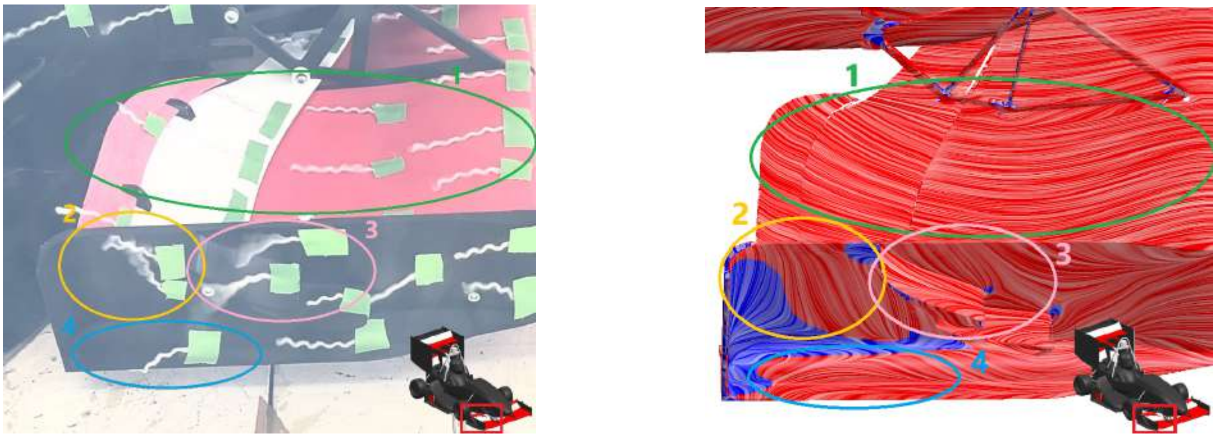

(a) EFD.

(b) CFD.

Figure 5.14: Flow visualization on front wing upper surfaces and endplate.

On the upper surface of the main element of the front wing, region 1 of Figure 5.14 shows that the flow remains attached along its entirety, a behavior corroborated by the experimental results. Some relevant discrepancies arise on the endplate area: in region 2, the experiments reveal local separation zones, whereas the numerical results predict separation slightly further downstream. This offset is aerodynamically relevant, as endplate separation strongly affects the strength and positioning of the outboard vortex structures responsible for managing the front tire wake, making this region particularly sensitive to small positional shifts. Region 3 highlights vorticity around the canards in the experiments. While this feature cannot be directly compared with Figure 5.14b, since it does not capture three-dimensional behavior alone, the absence of separation in the numerical results suggests a further discrepancy in this area. Finally, in region 4 of 5.14a, the tufts are observed rotating into the tubular vortex generator, confirming its ingestion of the local flow and showing agreement with the surface streamlines predicted numerically in Figure 5.14b.

In addition, tuft vibrations were observed during the WT experiments, most notably in the front wing region. As the front wing is the first component to interact with the incoming airflow, this observation indicates that the flow had already transitioned to turbulent before reaching the scaled model, thereby supporting the decision not to implement a transition model in the numerical setup. However, it should be emphasized that the front wing is the component most affected by discrepancies between the experimental and simulated boundary layer development along the bottom wall upstream of the car model.

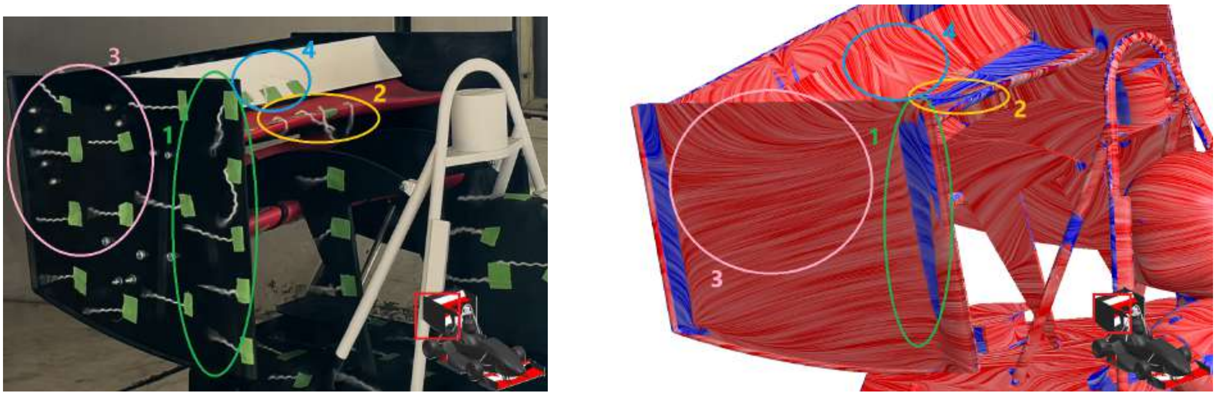

(a) EFD.

(b) CFD.

Figure 5.15: Flow visualization on rear wing upper surfaces and endplate.

On the outer surface of the rear wing endplate, at its leading edge, highlighted as region 1 in Figure 5.15 shows good agreement in the upper portion, where clear separation is observed both experimentally and numerically. In the lower portion, however, some disagreement arises: the numerical results predict a smaller but existent separation zone, whereas the experiments suggest attached flow. On the upper surface of the flap (region 2), a central separation zone on the wing is consistently captured by both approaches. Further downstream on the endplate, region 3 also indicates acceptable agreement between the experimentally and numerically obtained surface streamlines, showing that the global outboard flow behavior is reproduced numerically. Finally, on the upper surface of the flap in region 4, discrepancies emerge once again: the experimental results reveal separations and a clear recirculation zone, while the numerical predictions indicate fully attached flow. Such differences may be relevant, as they highlight the sensitivity of this area to specific local flow conditions.

Overall, the flow visualization, together with the previous force and pressure comparisons discussed in Sections 5.2 and 5.3, reveals that the numerical setup is capable of capturing the essential aerodynamic phenomena and performance trends. This establishes the confidence needed in the numerical approach, allowing the simulation conditions to now be adapted to represent on-track scenarios and thereby assess the behavior of each configuration under those conditions.

Chapter 6

Numerical Assessment of Differences between WT and On-Track Conditions

Building upon the results presented in the preceding chapter, this chapter aims to assess the influence of the main discrepancies between the WT setup and the actual on-track operating conditions on the aerodynamic performance of the vehicle. The parameters considered include the Reynolds number associated with the reduced car model scale, the increased ground clearance, the absence of wheel rotation, the stationary ground, and the boundary conditions imposed at the lateral and upper walls of the test section, which give rise to blockage effects. A series of numerical simulations is conducted to isolate the contribution of each factor, enabling a systematic transition toward conditions representative of real race track operation.

6.1 Ride Height

To initiate the transition from the wind tunnel numerical setup to the real on-track conditions, the model ground clearance was first reduced from $5\ \mathrm{mm}$ to $0\ \mathrm{mm}$, corresponding to the tires being in direct contact with the ground. To isolate the effect of ride height on the results, a dedicated set of simulations was performed with this single modification in the setup, applied across all three side element configurations.

As shown in Figure 6.1, which depicts configuration C, the reduction in ground clearance leads to a clear intensification of the low pressure regions beneath the floor, particularly along the main wing of the side elements. This expansion of the suction footprint reflects a higher mass flow acceleration and more effective pressure recovery within the diffuser, ultimately resulting in a net increase in the overall downforce generated by the car.

Quantitatively, in Figure 6.2, this behavior is reflected in a consistent rise in the lift coefficient across all configurations, with ΔC_L values ranging approximately between 0.15 and 0.25 (about 5%), while the drag coefficient increases only marginally. Consequently, the aerodynamic efficiency slightly improves, suggesting that the floor operates closer to its optimal sealing condition without entering a regime of

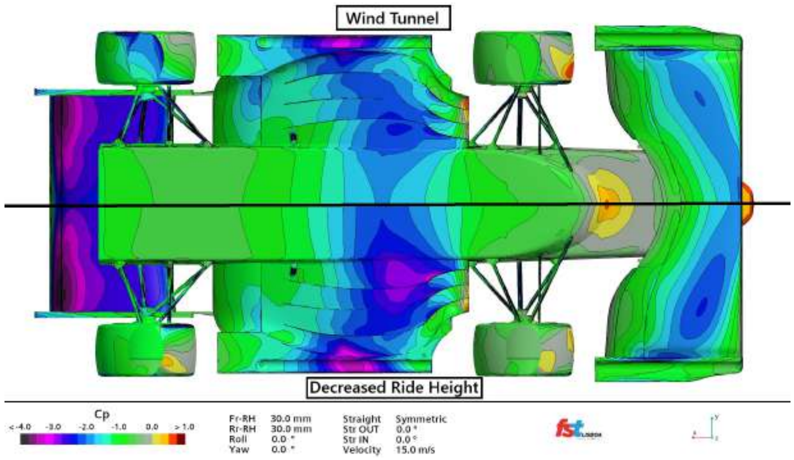

Figure 6.1: Ride height effect on pressure coefficient at the bottom of the model for configuration C.

diffuser choking or flow separation. The enhanced suction near the floor throat and front wing also contributes to a forward redistribution of aerodynamic loads, resulting in a modest but consistent increase in the aerodynamic balance towards the front axle. This effect is particularly evident for configuration B, which exhibits the highest front end sensitivity and benefits most from the improved ground effect while maintaining stable rear flow behavior.

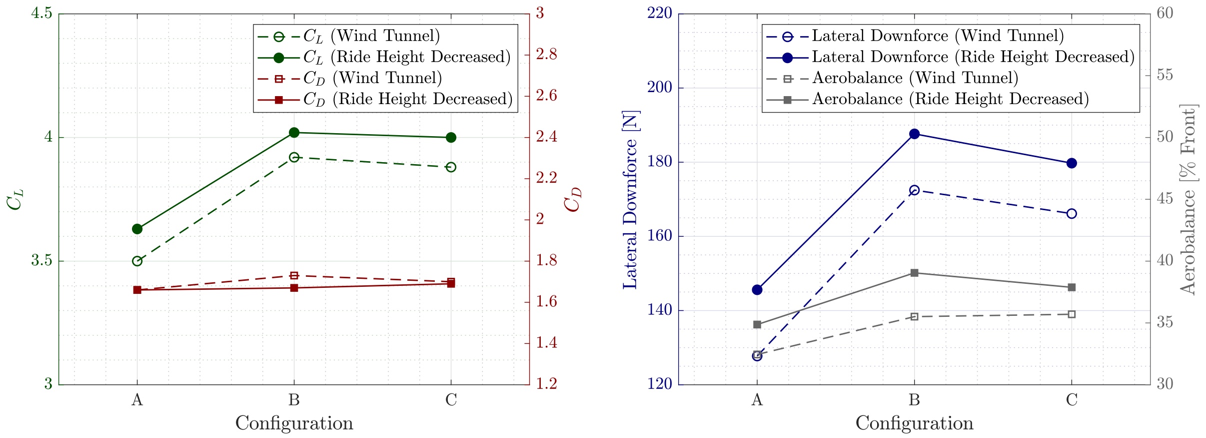

(a) Lift and drag coefficients.

(b) Lateral downforce and aerobalance.

Figure 6.2: Influence of ride height on key aerodynamic parameters for the three configurations.

The relative performance ranking among configurations remains unchanged when the model height is reduced, indicating that the aerodynamic trends previously observed under wind tunnel conditions are consistent through this first step toward on-track operation. The downforce generated by the components that were modified (lateral downforce) follows the same tendency, increasing by approximately $10-15\%$. Overall, reducing the ride height to $0\ \mathrm{mm}$ enhances the underbody effectiveness and slightly shifts the aerodynamic balance forward, while preserving the relative hierarchy between configurations.

6.2 Reynolds Number

The second step toward on-track conditions involves restoring the fluid properties to their real scale values, reversing the wind tunnel scaling applied in the previous section. Up to this point, the 1:3 scale model had been represented numerically by tripling the dynamic viscosity corresponding to the reference conditions. This approach allowed the geometry, and consequently the mesh, to remain consistent across all scenarios, as presented in Figure 6.3. Restoring the viscosity to its nominal value isolates the pure Reynolds number effects, ensuring that the simulated flow matches the conditions expected during on-track operation.

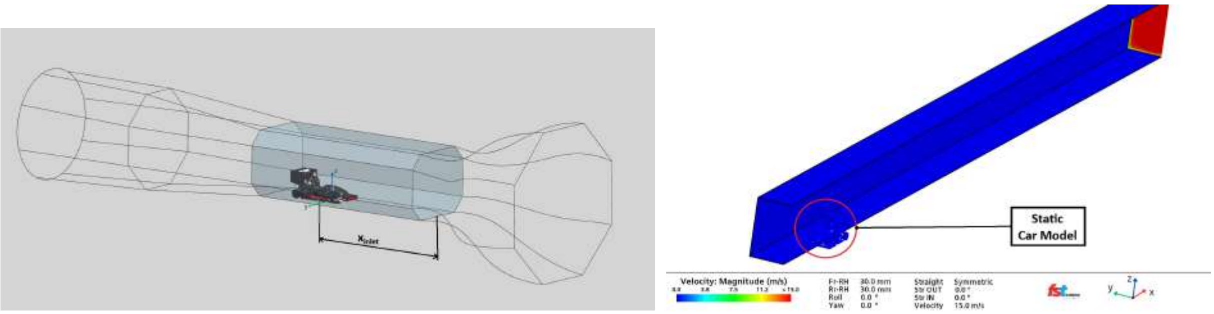

(a) Scaled model in the test section geometry.

(b) CFD boundary setup.

Figure 6.3: Simulation overview for the isolation of the scale effect.

The bottom view C_p field for configuration C, shown in Figure 6.4, exhibits a deeper and more continuous low pressure footprint across the monocoque and main side wings, with sharper gradients near the throat and a smoother pressure recovery within the diffuser section. This behavior is consistent with thinner boundary layers and reduced viscous diffusion at higher Re, which enhance underfloor pumping and delay incipient separation without any evidence of flow choking.

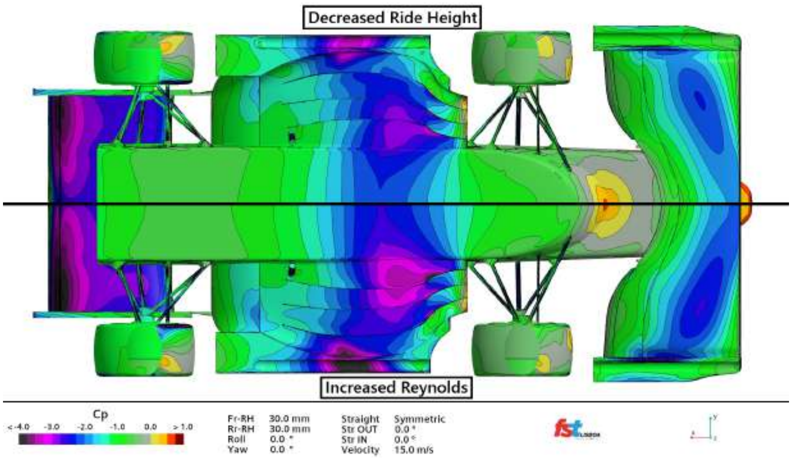

Figure 6.4: Reynolds number effect on pressure coefficient at the bottom of the model for configuration C.

The aerodynamic coefficients presented in Figure 6.5 confirm the field level observations discussed previously. Relative to the preceding case, the lift coefficient increases across all configurations, while the drag coefficient remains nearly constant, resulting in a net gain in aerodynamic efficiency. The downforce generated by the side elements increases significantly for all configurations, reflecting more coherent and less diffusive vortex structures along the strakes and stronger suction within the tubular vortex generators. In contrast to the global C_L, the configuration hierarchy for this metric remains unchanged from the previous scenario, with configuration B still producing the highest lateral load. Finally, the aerodynamic balance shifts only slightly toward the front, and by a smaller margin than in the ride height reduction step, indicating that the higher Re effects are distributed relatively evenly between both axles.

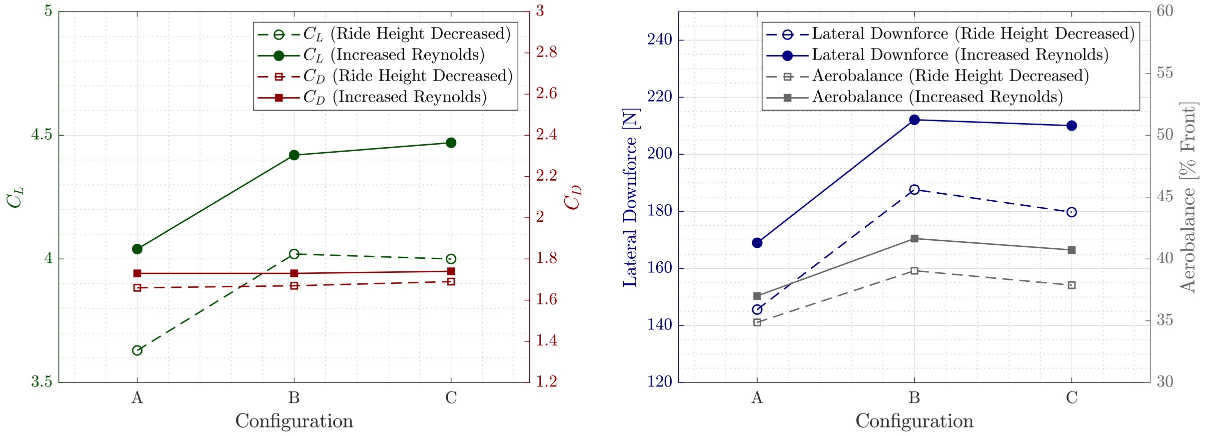

(a) Lift and drag coefficients.

(b) Lateral downforce and aerobalance.

Figure 6.5: Influence of Reynolds number on key parameters for the three tested configurations.

Up to this point, the main observation is that the variations primarily result in an almost uniform shift in the magnitude of the key aerodynamic parameters across configurations. Consequently, the relative trends previously established under wind tunnel conditions remain consistent, as shown in Figure 6.6, which presents the normalized differences of the main coefficients with respect to configuration A, confirming that the comparative behavior between configurations is largely preserved.

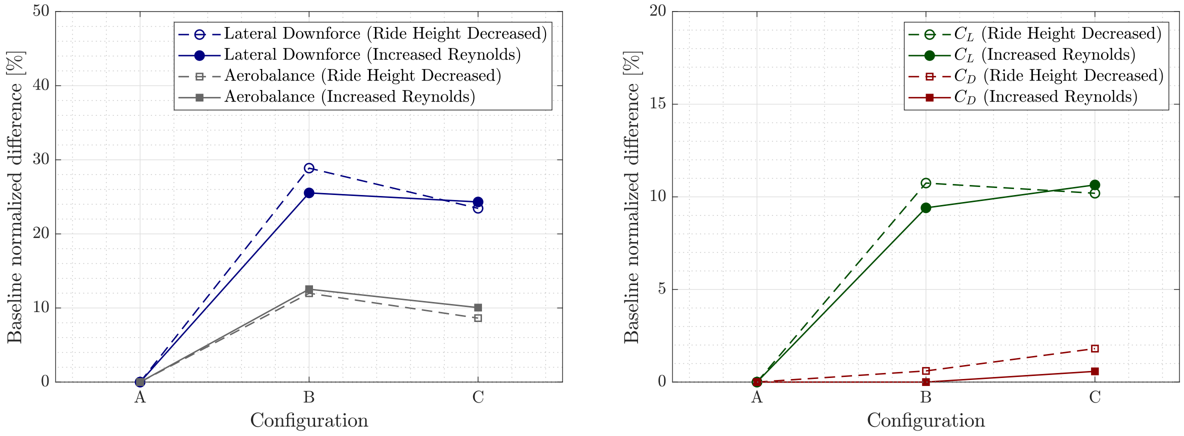

(a) Lift and drag coefficients.

(b) Lateral downforce and aerobalance.

Figure 6.6: Influence of Reynolds number on normalized key parameters for the three tested configurations.

6.3 Moving Ground and Wheel Rotation

The next step toward on-track conditions introduces the motion of both the ground and wheels within the wind tunnel domain, while maintaining the increased Reynolds number. For this purpose, the ground boundary was set to a speed equaling the airspeed to mimick the exact relative motion of the car while on road in real life conditions and also the wheel rotation was enabled by turning on the angular velocity of each wheel based on the inlet speed specified. Prism layers were disabled on the ground surface. This setup is shown in Figure 6.7 and enforces the correct kinematic conditions at the tire road interface, eliminating the steady bottom wall boundary layer that previously developed upstream of the model. As a result, the flow approaching the car maintains a uniform velocity profile, allowing the effects of wheel rotation and ground movement to be assessed in isolation.

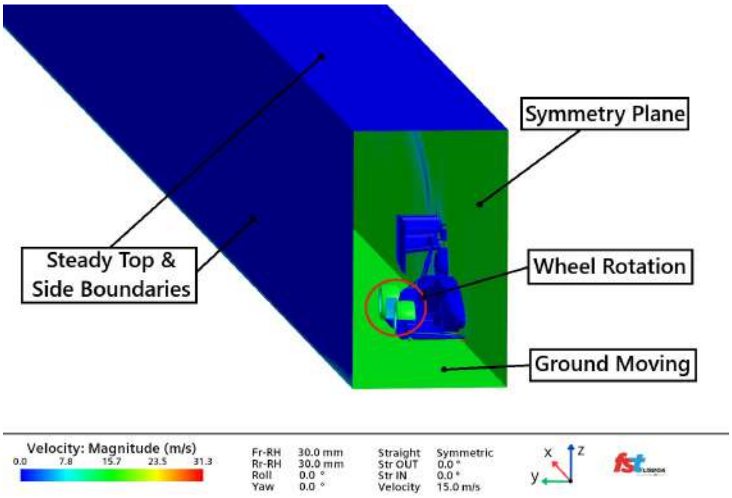

Figure 6.7: Boundary conditions with ground and wheels motion.

The bottom view C_p field for configuration C in Figure 6.8 reveals a pronounced intensification of the suction regions beneath the car once ground and wheel motion are activated. Compared with the previous increased Reynolds setup, the low pressure footprint extends further longitudinally along the floor and laterally across the side elements, while the minimum C_p values deepen in the main wing and near the floor edge vortex generators. The moving ground suppresses boundary layer growth along the floor and primarily upstream of the car, increasing the portion of the flow that remains weakly affected by viscosity as it reaches the underbody. This allows the flow in this region to reproduce more faithfully the behavior observed under real on-track conditions. These mechanisms, primarily induced by the ground motion, enhance the underfloor suction and substantially reinforce the ground effect contribution. The intensified suction beneath the front wing further confirms this behavior, while the steeper pressure gradients observed along the floor and its edges align with the expected aerodynamic response to realistic kinematic boundary conditions: higher local velocities, stronger load coupling between the floor and the lateral diffuser, and an overall increase in downforce without signs of adverse flow separation or significant asymmetry.

The integrated aerodynamic results in Figure 6.9 are consistent with the field level observations. When the motion of the ground and wheels is activated, the lift coefficient increases across all config-

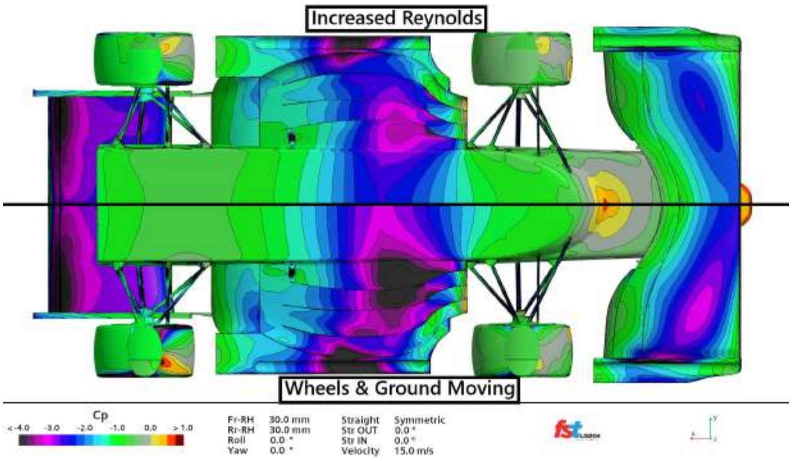

Figure 6.8: Wheel rotation and ground movement effect on pressure coefficient at the bottom of the model for configuration C.

urations relative to the previous state, confirming the reinforcement of ground effect suction observed in the C_p maps. The overall trend reverses and $C_{L_C} > C_{L_B} > C_{L_A}$ becomes pronounced, even lying outside the numerical uncertainty particularly for configurations B and C, which exhibit the strongest sensitivity to the more realistic near ground flow conditions. The additional momentum introduced by this different set of boundary conditions increases the mass flow rate beneath the car, translating directly into higher downforce levels.

The drag response exhibits a configuration dependent behavior. Only configuration C shows a noticeable increase in C_D, attributable to the higher underfloor mass flow and the stronger tire and diffuser associated vorticity accompanying its larger downforce rise. In contrast, configurations A and B display C_D variations that are neutral or slightly negative, suggesting that their incremental pressure drag penalty is compensated by smoother pressure recovery and limited growth in induced and vortex-related losses at this stage.

The aerodynamic balance experiences a modest forward shift, as the front axle gains proportionally more load driven by the intensified suction beneath the front wing and a more momentum-filled underbody stream, resulting in a slight forward migration of the pressure center. The downforce generated by the modified elements increases across all configurations, as expected, maintaining the trend observed in the C_L plot, with configuration C exhibiting the largest increment, consistent with the reinforced suction throughout.

It is important to note that if the enlargement of the computational domain and the increase in inlet distance had been performed prior to activating the ground and wheel motion, the effect of the domain size would not have been properly isolated. Under a stationary ground condition, the incoming boundary layer develops along the floor between the inlet and the car, thickening with distance and reducing the effective flow momentum at the vehicle's leading edge, artificially decreasing the underfloor mass flow and overall downforce. Consequently, the impact observed in such a step would represent a combination of two distinct phenomena: the reduction of blockage due to the enlarged domain and the attenuation of ground effect caused by the thicker upstream boundary layer. By introducing ground and wheel motion

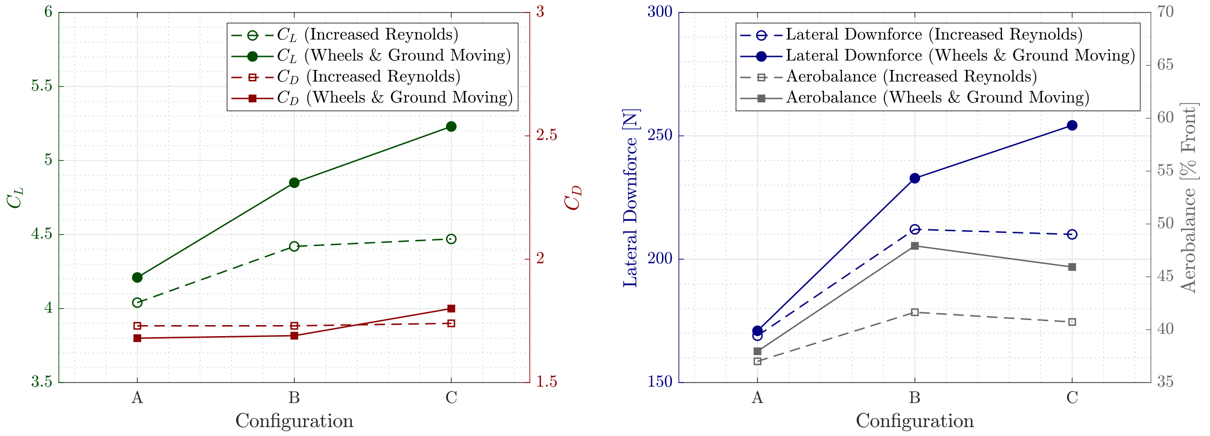

(a) Lift and drag coefficients.

(b) Lateral downforce and aerobalance.

Figure 6.9: Influence of boundary conditions on key aerodynamic parameters for the three configurations.

first, the floor boundary layer is effectively eliminated, as the moving wall enforces $U = U_\infty$. This approach ensures that the subsequent domain enlargement isolates only the blockage effects, allowing for a more accurate assessment of the phenomena governing the transition toward on-track conditions.

6.4 Domain Size

The final transition to numerically simulated on-track conditions involved enlarging the computational domain and relaxing the confinement imposed by the remaining wind tunnel boundaries. The parallelepiped domain was expanded to a $7 \times 10\ \mathrm{m}$ cross section for the half-car simulation, with the top and outer boundaries redefined as symmetry planes. Prism layers were disabled on these surfaces, as no boundary layers are purposefully expected to be resolved there. The inlet was moved upstream to approximately 3 car lengths, while the outlet was kept at about 13 car lengths downstream, as shown in Figure 3.2a. These modifications effectively isolate blockage and wall proximity effects while preserving the same geometry, mesh, operating Reynolds number and wheel and ground movement.

The bottom view C_p field for configuration C in Figure 6.10 shows an attenuation of the suction regions beneath the floor and side elements once the computational domain is enlarged and the inlet distance is extended. Compared with the previous step, the pressure gradients become smoother and the low pressure areas lose some intensity, particularly in the side elements' main wing and in the front wing as well. This reduction in suction confirms that the aerodynamic force amplification previously observed was partly driven by wall confinement effects within the smaller wind tunnel domain. As the boundaries move farther away, the free stream acceleration and artificial sealing effects induced by the no-slip walls disappear, allowing the flow to recover its natural external field expansion. This results in a more realistic pressure distribution consistent with unconfined on-track operation, where blockage is minimal and the mass flow through the underfloor is constrained solely by the car's geometry.

The integrated aerodynamic results in Figure 6.11 corroborate once again these field level observa-

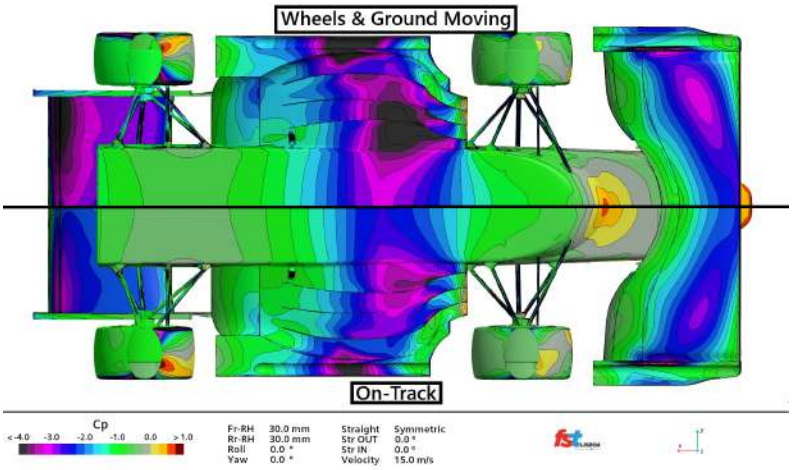

Figure 6.10: Domain size effect on pressure coefficient at the bottom of the model for configuration C.

tions. The lift coefficient decreases for all configurations relative to the confined moving ground state, while maintaining the same configuration ordering. The reduction in C_L is a direct consequence of diminished blockage and reduced local velocity amplification under the floor. The drag coefficient follows a similar trend, modestly decreasing for all configurations, indicating that the removal of confinement lessens both pressure drag and induced drag. Downforce generated by the side elements also drops, reflecting the weaker suction, mainly for configurations B and C and the weaker side vortices once the tunnel walls no longer constrain lateral flow development.

The aerobalance exhibits again a mild forward shift. The decrease in rear loading is proportionally larger than that observed at the front, as the rear seems to lose a significant portion of the loading previously enhanced by the confined environment. The rear wing is affected by the weakened upwash and reduced interaction with the side elements, resulting in a notable loss of downforce contribution. Conversely, the front wing and forward portion of the car overall retain a greater share of their load, leading to the observed forward migration of the pressure center. This redistribution reflects a more balanced and physically representative load breakdown under true on–track conditions.

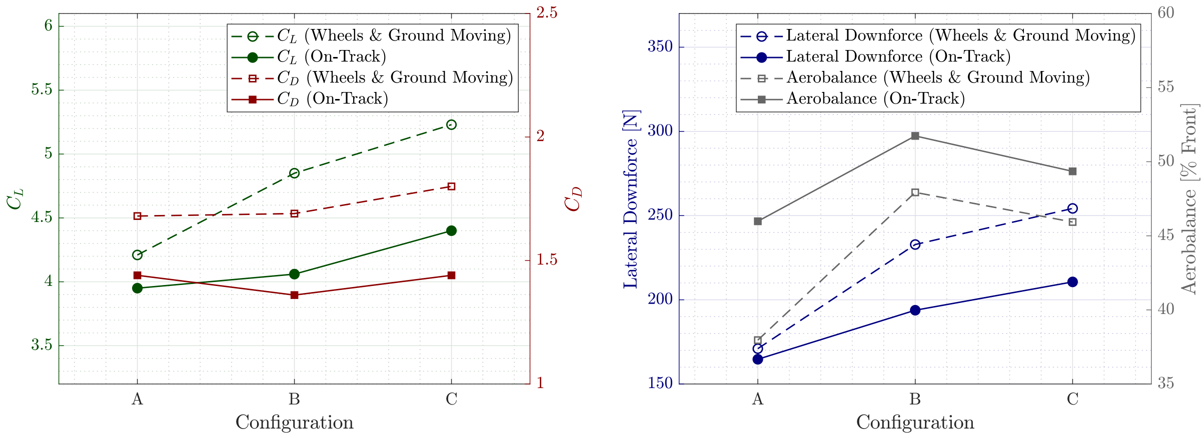

(a) Lift and drag coefficients.

(b) Lateral downforce and aerobalance.

Figure 6.11: Influence of domain size on key aerodynamic parameters for the three configurations.

Comparing the configurations, a clear and consistent performance hierarchy emerges under on-track conditions: the global lift coefficients follow $C_{L_C} > C_{L_B} > C_{L_A}$, the lateral downforce exhibits the same trend, $DF_C > DF_B > DF_A$, and the aerodynamic balance becomes uniformly more front-biased relative to the wheel and ground movement enabled case. Configuration C showed the highest sensitivity to the inclusion of realistic wheel and ground kinematics, its underfloor and side element architecture benefits most from the increased mass flow. Configuration B remains competitive, particularly in loading itself, although its global C_L gain is smaller than configuration C, consistent with previous observations of higher ride height sensitivity. Configuration A exhibits the lowest overall performance, serving primarily as a baseline reference for comparison. A more in-depth analysis comparing each configuration under on-track conditions is presented next.

6.5 Geometry Comparison

The evolution of the aerodynamic coefficients across the simulated scenarios, shown in Figure 6.12, highlights the progressive influence of the modeling refinements on the predicted performance of three configurations. From the initial wind tunnel setup to the final on-track condition, a consistent increase in aerodynamic forces is observed, indicating that the progressive introduction of more realistic boundary conditions enhances overall load generation up to the stage where the domain size is expanded in the on-track simulations. The corresponding evolution of the aerodynamic balance follows a similar trend, progressively shifting forward and indicating a redistribution of aerodynamic loads toward the front axle as the setup converges to real operating conditions.

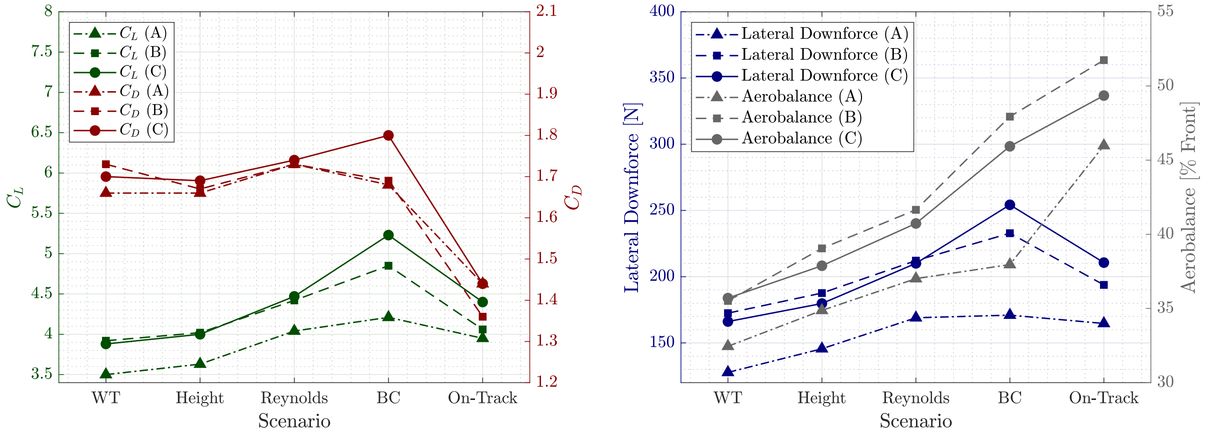

(a) Evolution of lift and drag coefficients.

(b) Evolution of the lateral downforce and aerobalance.

Figure 6.12: Key aerodynamic parameters for the three configurations across the simulated scenarios.

Altogether, these results confirm that each incremental modeling refinement systematically alters the flow field and aerodynamic performance throughout, progressively steering the predictions toward a more representative on-track condition. This also demonstrates that the performance trends obtained under the WT setup used in this study are not equivalent to those observed under on-track operation, making it impossible to directly compare on-track numerical simulations with WT results without introducing additional corrections on the numerical side. For instance, if a configuration were to be selected solely based on the WT numerical results with the goal of maximizing C_L, configuration B might appear preferable, whereas under on-track conditions its performance converges closer to that of configuration A, the baseline, than to configuration C. Similarly, if the objective were to minimize C_D, configuration A could be chosen, however, under on-track conditions, configuration A actually exhibits one of the highest C_D values among the three configurations.

Having completed the transition from the wind tunnel numerical setup to the on-track condition, with each intermediate step isolated and analyzed, the final stage consists of comparing the different side element configurations under on-track conditions. The following analysis presents a direct comparison between configurations A and C, as these represent the two performance extremes within the tested set and exhibit the largest aerodynamic discrepancies.

Starting from the bottom view C_p distribution in Figure 6.13, configuration C immediately exhibits a broader, stronger, and more upstream low pressure footprint along the lower surface of the main wing, while the front and rear wing load levels remain comparable to those of configuration A. This upstream migration of the suction peak anticipates the forward shift in aerodynamic balance later confirmed by the integrated results presented in Table 6.1.

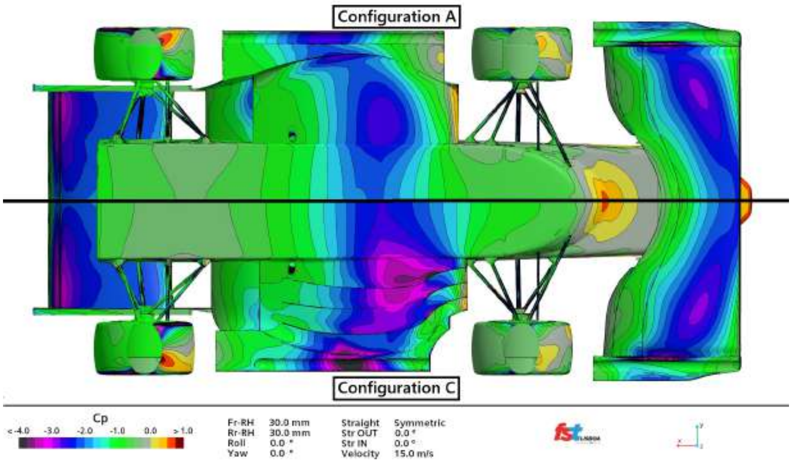

Figure 6.13: Comparison of the pressure coefficient at the bottom of the model for configurations C and A.

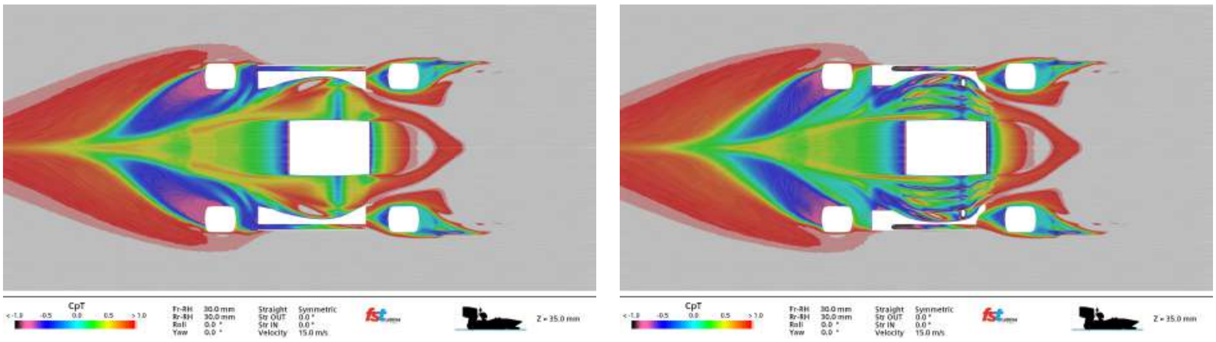

(a) Configuration A.

(b) Configuration C.

Figure 6.14: Total pressure coefficient at horizontal plane $z = 35\ mm$.

The underlying mechanism becomes evident in the total pressure coefficient (C_{p_T}) horizontal slice at $z = 35\ \mathrm{mm}$ shown in Figure 6.14. The extended strakes in configuration C generate multiple compact vortex cores that are effectively confined by the channel like geometry, delaying vortex bursting and directing the available total pressure more efficiently beneath the side wing to accelerate the flow. Conversely, configuration A presents near unity C_{p_T} regions beneath the main wing, clear indicators of unexploited flow potential and inefficient downforce generation capability.

Moving spanwise to the vertical plane intersecting the right side element, $y = 388\ \mathrm{mm}$ in Figure 6.15, both configurations maintain largely attached flow along their lower surfaces. However, configuration C, despite featuring a rounder leading edge and a slightly higher nose-up incidence and overall angle of attack, exhibits a smoother pressure distribution, indicating reduced profile losses for a given sectional loading, whereas configuration A lacks this favorable smoothing effect.

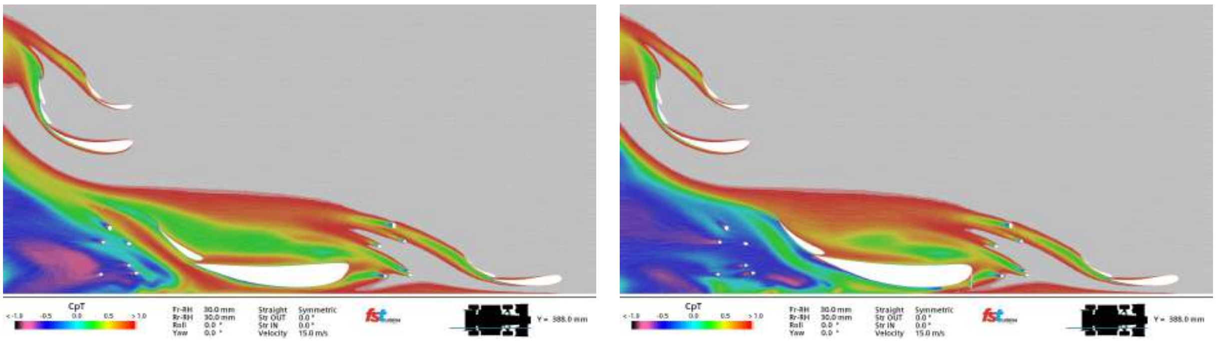

(a) Configuration A.

(b) Configuration C.

Figure 6.15: Total pressure coefficient at vertical plane $y = 388\ mm$.

The transversal plane at $x = 395\ \mathrm{mm}$ in Figure 6.16 illustrates the sectional consequences of these flow features. Configuration C sustains tight, inboard deficit lobes, signatures of strong, coherent vortex cores that actively enhance suction on the lower surface of the main wing, while simultaneously avoiding the small outboard upper surface energy dissipation visible in configuration A. This dissipation subsequently feeds the wake downstream. The vortex structures associated with Configuration C are directly visible in Figure 6.17, which displays the longitudinal vorticity for a transversal plane slightly downstream at $x = 500\ \mathrm{mm}$, where the vortices generated by the strakes and those originating from the tubular vortex generator can be clearly identified.

To further evaluate the impact of this phenomenon, the longitudinal skin friction coefficient and the limiting streamlines along the vehicle's surface, shown in Figure 6.18b, reveal that flow separation occurs on the upper surface of configuration A's main wing, as well as additional separation further downstream on the midplate region, unlike in configuration C. Moreover, Figure 6.18a indicates that despite the considerable increase in suction on the lower surface of configuration C's main wing, the separation that occurs is minor, with the flow reattaching before even reaching the corresponding flap. This confirms that no significant losses arise from the stronger pressure gradients in this configuration.

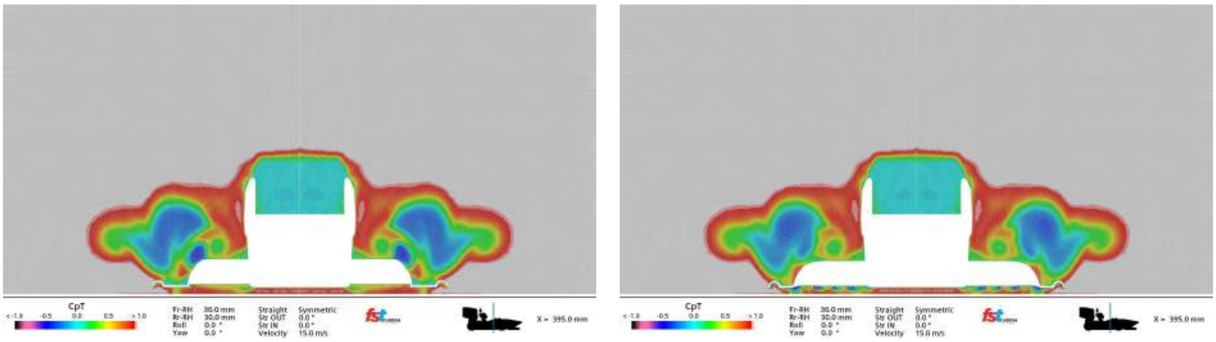

(a) Configuration A.

(b) Configuration C.

Figure 6.16: Total pressure coefficient at transversal plane $x = 395mm$.

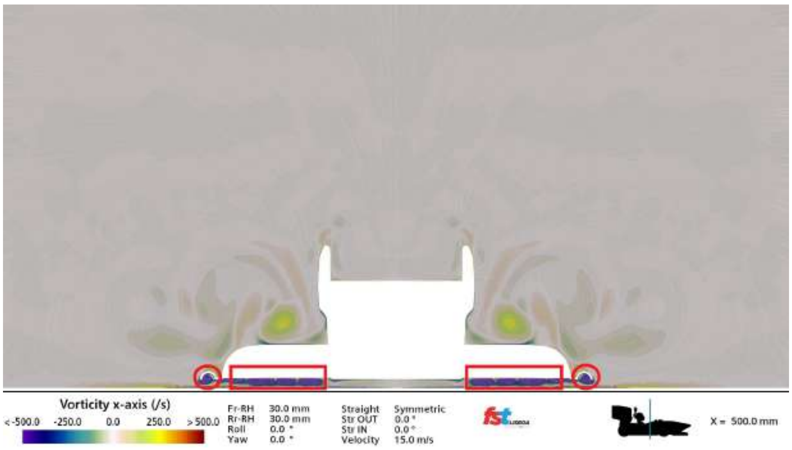

Figure 6.17: Vorticity along x-axis at the transversal plane $x = 500mm$ for configuration C.

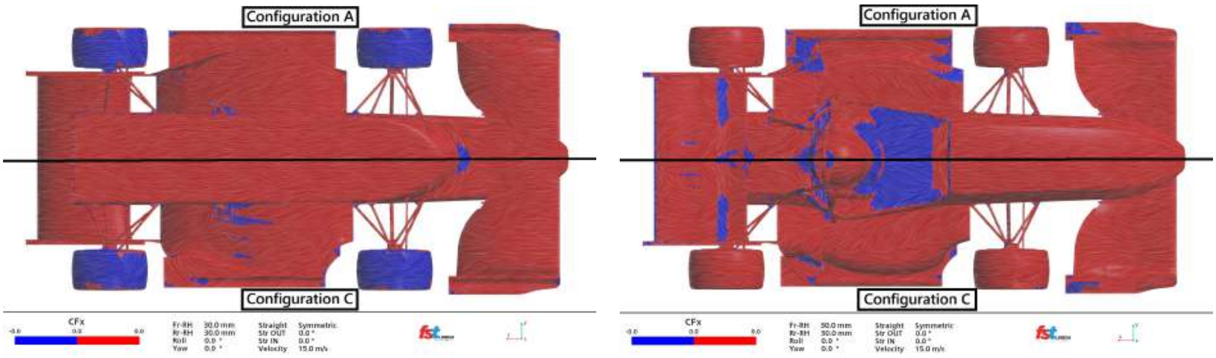

(a) Bottom view.

(b) Top view.

Figure 6.18: Longitudinal pressure coefficient and limiting streamlines along the surface of the car.

Further downstream, at $x = 1325$ mm in Figure 6.19, the difference in wake structure becomes evident: configuration C maintains a compact and stratified footprint, while configuration A exhibits vortex merging and spreading, indicating earlier breakdown and resulting in a wider wake. This behavior demonstrates greater energy dissipation for configuration A. Notably, at the rear wing height, the C_{p_T} patterns of both configurations remain very similar, indicating that configuration C's additional lower surface suction does not significantly disturb the rear wing incoming flow, consistent with the bottom view C_p observations showing preserved rear wing loading.

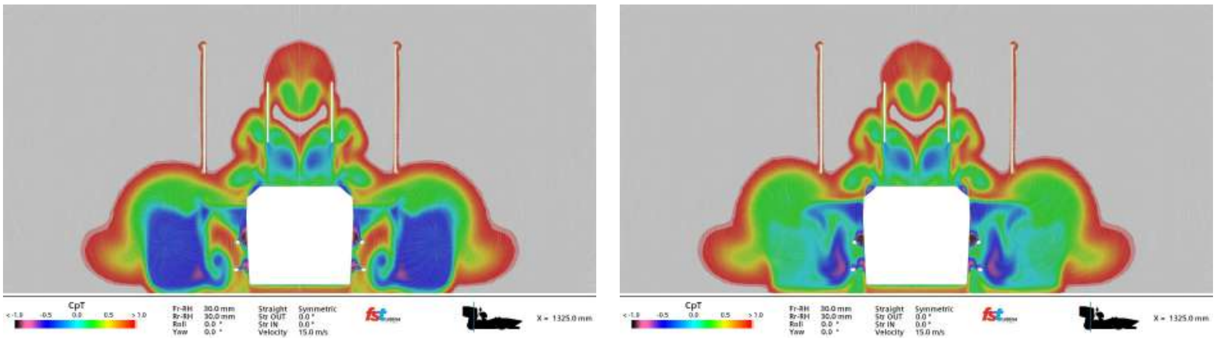

(a) Configuration A.

(b) Configuration C.

Figure 6.19: Total pressure coefficient at transversal plane $x = \ 1325mm$.

Altogether, these field level observations explain the integrated results reported in Table 6.1. The lift coefficient, C_L, increases from 3.95 in configuration A to 4.40 in configuration C, while the drag coefficient, C_D, remains essentially unchanged at 1.44. As a result, the aerodynamic efficiency improves from $C_L/C_D = 2.74$ to 3.05 ($+11.3\%$). The aerodynamic balance shifts forward from 45.98% to 49.35%, consistent with the upstream migration of the suction peak observed in the pressure distributions. Lateral downforce also rises substantially, from 164.7 to 210.6 N ($+27.9\%$), aligning with the flow field evidence that configuration C's channel concept retains and enhances the vortices generated by the strakes, delaying diffusion and producing stronger, more coherent lateral loading while minimizing leakage losses. The tubular vortex generator termination strategy is noteworthy: by interrupting it before the downstream floor edge, configuration C dissipates its circulation upstream in a controlled manner and sheds more cleanly. In contrast, configuration A extends the vortex generator to the floor's trailing edge, promoting an uncontrolled burst that merges with the rear tire wake, transforming potential underfloor suction into wake growth and additional pressure drag.

The mesh convergence estimates presented in Figure 3.9 are relevant to revisit here, as they quantify the numerical uncertainties. These values demonstrate that the gains observed from configuration A to configuration C, namely $+11.4\%$ in C_L and $+27.9\%$ in lateral downforce, lie beyond the corresponding numerical error boundaries, while the near equality in C_D remains consistent with the small drag uncertainty. In other words, the improvements identified are not only qualitatively evident in the flow fields but also quantitatively significant within the estimated numerical accuracy.

Table 6.1: Comparison of key aerodynamic parameters under on-track conditions.

Configuration	C_L	C_D	C_L/C_D	Aerobalance (% Front)	Lat. DF (N)
A	3.95	1.44	2.74	45.98	164.68
B	4.06	1.36	2.98	51.74	193.80
C	4.40	1.44	3.05	49.35	210.62

Chapter 7

Conclusions

7.1 Achievements

The present work aimed to characterize and experimentally evaluate the computational fluid dynamics methodology employed, followed by the comparison of different side element design configurations for the FST14 prototype. A complete 1:3 scale model was designed and manufactured, the conditions ranging from on-track to wind tunnel operation were isolated and systematically assessed, and the wind tunnel campaign was successfully reinstated as a reliable testing tool within the team's workflow.

The numerical campaign began with a thorough mesh convergence study, allowing the definition of a suitable mesh and the quantification of numerical error of approximately 4.29% in C_L, 1.1% in C_D, and 3.2% in side element downforce, establishing confidence bounds for subsequent analyses.

The experimental phase involved manufacturing a modular 1:3 scale model faithful to the FST14 geometry and preparing and calibrating the force balance. The adapted simulations replicated the wind tunnel conditions and were compared with the measured forces and surface pressures. The experimental results were primarily used for qualitative comparison due to the relatively high uncertainties, particularly the force measurements, yet they exhibited consistent aerodynamic trends. Surface pressure distributions showed agreement with the numerical simulations on the upper surface of the main wing across the different configurations, while discrepancies observed on the lower surfaces were primarily attributed to dynamic attitude variations during testing. Flow visualization supported these findings, displaying coherent attachment and separation regions comparable to the predicted streamlines, though some three-dimensional effects were impossible to capture. Altogether, these results reinforced confidence in the numerical methodology for subsequent analyses. Despite successfully reproducing the main experimental trends, the CFD setup would still benefit refinement to improve quantitative accuracy, as certain simplifications and the rigid body assumption limited full replication of the experimental behavior. Nevertheless, the approach proved effective for evaluating geometric modifications and remains a robust tool.

Building on this experimental process, the numerical framework was extended to realistic on-track conditions, progressively incorporating the effects of ride height, geometric scaling, ground and wheel motion, and flow confinement. This systematic approach enabled the isolation of each influencing factor and clarified their relative impact on the vehicle's aerodynamic behavior. Within this framework, the comparison between configurations confirmed the superiority of the improved design, which maintained high aerodynamic efficiency and stable load distribution. The channel based concept implemented in configuration C yielded the most coherent flow structures and the highest efficiency, achieving an 11.4% increase in C_L, maintaining C_D nearly constant, and improving the C_L/C_D ratio by about 11%. The side element contribution to downforce rose by approximately 28%, while the aerodynamic balance shifted forward by roughly 3.4% compared to configuration A.

7.2 Future Work

Although the main objectives of this work were successfully achieved, several aspects remain open for further development. Future research should focus on improving the correlation between experimental and numerical results, increasing measurement accuracy, and extending the aerodynamic development process toward full vehicle integration.

On the experimental side, future testing campaigns should aim to enhance the precision and repeatability of force and pressure measurements. Refining the balance structure, sensors, and calibration procedure, along with expanding the pressure tap network, would significantly improve accuracy. Implementing a moving ground and rotating wheels is strongly recommended to better reproduce on-track conditions, while complementary flow visualization techniques, such as smoke or oil flow, could provide further insight into the three-dimensional flow behavior. Finally, a more rigorous uncertainty quantification, tracing error propagation through the measurement chain and assessing external influences, would increase the reliability of experimental correlations.

In the numerical domain, efforts should aim to further reduce the uncertainties found in the mesh convergence study. Although computational limitations restricted the achievable refinement, several improvements remain possible. Additional local mesh refinement in regions of steep pressure gradients and strong vorticity would improve accuracy without excessive cost, while the use of transitional or hybrid RANS-LES models could enhance prediction quality if sufficient computational resources are available.

Finally, extending the validation framework to on-track testing with the real FST14 car, with load or pressure instrumentation, would further strengthen the link between simulation and real performance, supporting the continued development of a robust, experimentally validated aerodynamic design methodology within FST Lisboa.

Bibliography

[1] F. S. Germany. Competition disciplines. https://www.formulastudent.de/about/disciplines/. Accessed on October 14, 2024.

[2] F. S. Germany. Rules for FSG 2025. https://www.formulastudent.de/fsg/rules/, 2024. Accessed on October 14, 2024.

[3] S. Wordley and J. Saunders. Aerodynamics for formula SAE: Initial design and performance prediction. April 2006. doi: 10.4271/2006-01-0806.

[4] A. F. R. Oliveira. Design, construction, calibration and testing of a wind tunnel force balance. Master's thesis, Instituto Superior Técnico, Universidade de Lisboa, Portugal, 2020.

[5] M. A. M. A. Ferreira. Design of a six-component external wind tunnel balance. Master's thesis, Instituto Superior Técnico, Universidade de Lisboa, Portugal, 2015.

[6] T. P. Rocha. Numerical and experimental study of wing tip endplates of a formula student car. Master's thesis, Instituto Superior Técnico, Universidade de Lisboa, Portugal, 2020.

[7] M. M. Carreira. Aerodynamic mapping of a formula student prototype using numerical simulations and on-track validation. Master's thesis, Instituto Superior Técnico, Universidade de Lisboa, Portugal, 2022.

[8] J. R. M. Pacheco. Wind tunnel testing of a complete formula student vehicle. Master's thesis, Instituto Superior Técnico, Universidade de Lisboa, Portugal, 2022.

[9] L. M. P. Afonso. Aerodynamic design and wind tunnel testing of the rear end of a formula student vehicle. Master's thesis, Instituto Superior Técnico, Universidade de Lisboa, Portugal, 2022.

[10] J. P. L. Morgado. Design and testing of a rear wing for a formula student car. Master's thesis, Faculdade de Ciências - Universidade de Lisboa, Portugal, 2022.

[11] S. Wordley and J. Saunders. Aerodynamics for formula SAE: A numerical, wind tunnel and on-track study. April 2006. doi: 10.4271/2006-01-0808.

[12] E. S. Cole. Design and validation of an aerodynamic system for a formula SAE vehicle using vehicle dynamic simulation and experimentation. Master's thesis, Statler College of Engineering and Mineral Resources, West Virginia University, USA, 2023.

[13] I. Oxyzoglou. *Design and Development of an Aerodynamic Package for an FSAE Race Car*. PhD thesis, University of Thessaly, Greece, 2017.

[14] W. Milliken and D. Milliken. *Race Car Vehicle Dynamics*. SAE International, 1994. ISBN 978-1560915263.

[15] J. Katz. *Race Car Aerodynamics: Designing for Speed*, chapter 5, pages 147–157. Bentley Publishers, 1995. ISBN 978-0837601427.

[16] V. de Brederode. *Aerodinâmica Incompressível: Fundamentos*. IST Press, 2014. ISBN 978-9898481320.

[17] J. Anderson. *Fundamentals of Aerodynamics*. McGraw-Hill Series in Aeronautical and Aerospace Engineering, 2017. ISBN 978-1259129919.

[18] R. H. Sabersky, A. J. Acosta, and E. G. Hauptmann. Fluid flow: A first course in fluid mechanics. 1989. ISBN 978-0024049605.

[19] F. M. White. *Fluid Mechanics*. McGraw-Hill Series in Mechanical Engineering, 2017. ISBN 978-9385965494.

[20] H. Schlichting and E. Truckenbradt. *Aerodynamics of the Airplane*. McGraw-Hill, 1979. ISBN 978-0070553415.

[21] H. Schlichting and K. Gersten. *Boundary-Layer Theory*. January 2017. ISBN 978-3662529171. doi: 10.1007/978-3-662-52919-5.

[22] X. Zhang, W. Toet, and J. Zerihan. Ground Effect Aerodynamics of Race Cars. *Applied Mechanics Reviews*, 59(1):33–49, 2006. doi: 10.1115/1.2110263.

[23] S. McBeath. *Competition Car Aerodynamics: A Practical Handbook - 3rd Edition*. Veloce Publishing Limited, 2017. ISBN 978-1787111028.

[24] M. Nitsche. Vortex dynamics. In J.-P. Françoise, G. L. Naber, and T. S. Tsun, editors, *Encyclopedia of Mathematical Physics*, pages 390–399. Academic Press, Oxford, 2006. ISBN 978-0125126663. doi: https://doi.org/10.1016/B0-12-512666-2/00254-6.

[25] A. Guerrero and R. Castilla. Aerodynamic study of the wake effects on a Formula 1 car. *Energies*, 13(19), 2020. doi: 10.3390/en13195183.

[26] A. Buljac, H. Kozmar, and I. Džijan. Aerodynamic performance of the underbody and wings of an open-wheel race car. *Transactions of FAMENA*, 40:19–34, July 2016. doi: 10.21278/TOF.40202.

[27] A. Bhardwaj. Analysis of ground effect diffuser on a race car to optimize aerodynamic performance. *International Journal of Innovative Science and Research Technology*, 6, May 2021.

[28] L. F. Gonzalez and K. M. Peddie. CFD study on the diffuser of a Formula 3 racecar. 2009. URL `https://api.semanticscholar.org/CorpusID:62890627`.

[29] O. Ehirim, K. Knowles, and A. Saddington. A review of ground-effect diffuser aerodynamics. *Journal of Fluids Engineering*, 141:020801, June 2018. doi: 10.1115/1.4040501.

[30] J. Katz. Aerodynamics in motorsports. *Proceedings of the Institution of Mechanical Engineers, Part P: Journal of Sports Engineering and Technology*, 235:175433711989322, December 2019. doi: 10.1177/1754337119893226.

[31] J. Katz and F. Morey. Aerodynamics of large-scale vortex generator in ground effect. *Journal of Fluids Engineering*, 130, July 2008. doi: 10.1115/1.2948361.

[32] J. Iljaž, L. Škerget, M. Štrakl, and J. Marn. Optimization of SAE formula rear wing. *Strojniški vestnik - Journal of Mechanical Engineering*, 62:263–272, 05 2016. doi: 10.5545/sv-jme.2016.3240.

[33] T. Price and R. Paul. Aerodynamic performance of a low aspect ratio active rear wing package designed for the OSU formula SAE team. January 2022. doi: 10.2514/6.2022-2609.

[34] R. Myose, I. Heron, and M. Papadakis. Gurney flap experiments on airfoils, wings, and reflection plane model. *Journal of Aircraft*, 35:206–211, March 1998. doi: 10.2514/2.2309.

[35] J. Zerihan and X. Zhang. Aerodynamics of Gurney flaps on a wing in ground effect. *American Institute of Aeronautics and Astronautics*, 39:772–780, May 2001. doi: 10.2514/2.1396.

[36] R. Raj, T. Naggari, and N. Prakash. Design and CFD analysis of a rear wing of a motorsport car. *International Journal of Vehicle Structures and Systems*, 14, January 2022. doi: 10.4273/ijvss.14.1.14.

[37] J. Ferziger. Simulation of complex turbulent flows: recent advances and prospects in wind engineering. In S. Murakami, editor, *Computational Wind Engineering 1*, pages 195–212. Elsevier, Oxford, 1993. ISBN 978-0-444-81688-7. doi: https://doi.org/10.1016/B978-0-444-81688-7.50023-1.

[38] P. M. Doran. Chapter 7 - fluid flow. In P. M. Doran, editor, *Bioprocess Engineering Principles (Second Edition)*, pages 201–254. Academic Press, London, second edition, 2013. ISBN 978-0-12-220851-5. doi: https://doi.org/10.1016/B978-0-12-220851-5.00007-1.

[39] N. D. Katopodes. Chapter 8 - turbulent flow. In N. D. Katopodes, editor, *Free-Surface Flow*, pages 566–650. Butterworth-Heinemann, 2019. ISBN 978-0-12-815489-2. doi: https://doi.org/10.1016/B978-0-12-815489-2.00008-3.

[40] J. Jackson and B. Launder. Osborne reynolds and the publication of his papers on turbulent flow. *Annual Review of Fluid Mechanics*, 39:19–35, December 2006. doi: 10.1146/annurev.fluid.39.050905.110241.

[41] C. Fu, M. Uddin, C. Robinson, A. Guzman, and D. Bailey. Turbulence models and model closure coefficients sensitivity of NASCAR racecar RANS CFD aerodynamic predictions. *SAE International Journal of Passenger Cars - Mechanical Systems*, 10:330–344, March 2017. doi: 10.4271/2017-01-1547.

[42] C. Akan. *Surface Mass Transfer in Large Eddy Simulation (LES) of Langmuir Turbulence*. PhD thesis, University of South Florida, USA, 2012.

[43] U. Goldberg. A realizable version of the κ–ω turbulence model. *Studies in Engineering and Technology*, 4:1, January 2017. doi: 10.11114/set.v4i1.1989.

[44] G. Alfonsi. Reynolds-averaged navier-stokes equations for turbulence modeling. *Applied Mechanics Reviews*, 62, July 2009. doi: 10.1115/1.3124648.

[45] OpenFOAM. Turbulence modeling scheme. URL `https://www.cfdsupport.com/openfoam-training-by-cfd-support/node346.html`. Acessed on 22 January, 2025.

[46] F. R. Menter. Zonal two-equation κ–ω turbulence models for aerodynamic flows. In *23rd Fluid Dynamics, Plasmadynamics, and Lasers Conference*, Orlando, Florida, USA, 1993. American Institute of Aeronautics and Astronautics. doi: 10.2514/6.1993-2906.

[47] A. M. Stefanescu. *RANS Turbulence Modelling for Motorsport Applications*. PhD thesis, Faculty of Sciene and Engineering, University of Manchester, UK, 2017.

[48] W. Oberkampf and C. Roy. *Verification and Validation in Scientific Computing*. January 2010. ISBN 9780521113601. doi: 10.1017/CBO9780511760396.

[49] L. Eça. *Aerodinâmica Incompressível: Exercícios*, chapter 7, pages 219–240. 2020. ISBN 978-9898481337.

[50] J. B. Barlow, J. William H. Rae, and A. Pope. *Low-Speed Wind Tunnel Testing 3rd Edition*. John Wiley and Sons. ISBN 0-471-55774-9.

[51] NASA Glenn Research Center. Closed return wind tunnel. URL `https://www.grc.nasa.gov/www/k-12/airplane/tuncret.html`. Accessed on September 19, 2025.

[52] J. G. Leishman. Dynamic similarity. In *Introduction to Aerospace Flight Vehicles*, chapter 17. Embry-Riddle Aeronautical University, 2023. ISBN 979-8-9852614-0-0. doi: https://doi.org/https://doi.org/10.15394/eaglepub.2022.1066.n14.

[53] R. He, H. Sun, X. Gao, and H. Yang. Wind tunnel tests for wind turbines: A state-of-the-art review. *Renewable and Sustainable Energy Reviews*, 166:112675, 2022. ISSN 1364-0321. doi: https://doi.org/10.1016/j.rser.2022.112675.

[54] Simcenter STAR-CCM+ User Guide. Siemens Digital Industries Software, 2022. Version 2210.1.

[55] F. Trivellato and M. Raciti Castelli. On the Courant–Friedrichs–Lewy criterion of rotating grids in 2D vertical-axis wind turbine analysis. *Renewable Energy*, 62:53–62, 2014. doi: https://doi.org/10.1016/j.renene.2013.06.022.

[56] V. Venkatakrishnan. On the accuracy of limiters and convergence to steady state solutions. In *31st Aerospace Sciences Meeting*, Reno, Nevada, USA, January 1993. American Institute of Aeronautics and Astronautics. doi: 10.2514/6.1993-880.

[57] L. Eça and M. Hoekstra. The numerical friction line. *International Journal for Numerical Methods in Fluids*, 61:473–499, 2009.

[58] L. Eça, R. Lopes, S. L. Toxopeus, and M. Kerkvliet. Transition from laminar to turbulent flow. In *Proceedings of the 6th International Symposium on Marine Propulsors*, UK, June 2021. University of Strathclyde.

[59] M. Sosnowski, J. Krzywanski, K. Grabowska, and R. Gnatowska. Polyhedral meshing in numerical analysis of conjugate heat transfer. *EPJ Web of Conferences*, 180, November 2018. doi: 10.1051/epjconf/201818002096.

[60] L. Eça and M. Hoekstra. A procedure for the estimation of the numerical uncertainty of CFD calculations based on grid refinement studies. *Journal of Computational Physics*, 262:104–130, 2014. doi: 10.1016/j.jcp.2014.01.006.

[61] L. Eça, G. Vaz, S. Toxopeus, and M. Hoekstra. Numerical errors in unsteady flow simulations. *Journal of Verification, Validation and Uncertainty Quantification*, 4, May 2019. doi: 10.1115/1.4043975.

[62] L. M. S. Lopes. Experimental study of vortex shedding mitigation in circular cylinders with helical strakes. Master's thesis, Instituto Superior Técnico, Universidade de Lisboa, Portugal, 2025.

[63] A. R. J. Borges. O túnel aerodinâmico do Laboratório Nacional de Engenharia Civil: 1^{a} parte - descrição geral. Technical Report Memória n. 319, Laboratório Nacional de Engenharia Civil (LNEC), Lisboa, 1968.

[64] A. R. J. Borges. O túnel aerodinâmico do LNEC: 2^{a} parte - cálculo e medição da velocidade em vazio. Technical report, Laboratório Nacional de Engenharia Civil (LNEC), Lisboa, 1968.

[65] A. R. J. Borges. O túnel aerodinâmico do lnec: 3^{a} parte - características do escoamento na câmara de experiências. Technical report, Laboratório Nacional de Engenharia Civil (LNEC), Lisboa, 1968.

[66] N. G. R. Center. Viscosity of air - Sutherland's law, 2023. URL `https://www.grc.nasa.gov/www/k-12/airplane/viscosity.html`. Accessed on August 18, 2025.

[67] J. B. Barlow, W. H. Rae, and A. Pope. *Low-Speed Wind Tunnel Testing 3rd Edition*. 1999. ISBN 978-0471557746.

[68] Bambu Lab. Bambu lab - official website. `https://bambulab.com`.

[69] Prusa Research. Original prusa 3D printers - official website. `https://www.prusa3d.com`.

[70] Raise3D Technologies. Raise3D - official website. `https://www.raise3d.com`.

Appendix A

Side Elements Design

Table A.1: Key aerodynamic performance parameters for a selected set of design iterations.

Configuration	Iteration	CL	CD	CL/CD	Aerobalance (% Front)
A	1	3.95	1.44	2.74	45.98
	5	3.88	1.42	2.73	41.61
	7	3.84	1.40	2.74	40.93
	10	3.79	1.39	2.72	42.90
	13	3.69	1.38	2.67	40.82
	15	3.63	1.40	2.59	43.19
	17	3.81	1.46	2.61	46.42
	19	4.00	1.43	2.80	50.89
	22	4.03	1.43	2.82	50.33
	25	4.05	1.39	2.91	50.73
B	28	4.06	1.36	2.99	51.74
	33	4.11	1.38	2.98	46.73
	35	4.07	1.38	2.95	47.78
	39	4.05	1.37	2.96	47.23
	41	4.08	1.39	2.94	47.11
	44	4.19	1.40	2.99	47.13
	48	4.22	1.42	2.97	47.03
	51	4.23	1.47	2.88	51.14
	54	4.23	1.43	2.96	50.61
	59	4.26	1.44	2.96	49.99
	63	4.32	1.47	2.94	49.73
	66	4.35	1.40	3.11	48.65
C	70	4.40	1.44	3.06	49.35
	72	4.37	1.44	3.03	48.63
	74	4.36	1.45	3.01	49.48

Appendix B

Experimental Setup

B.1 New Sensing Bar Manufacturing and Calibration

The state of bar number six upon arrival at the wind tunnel facility is displayed in Figure B.1.

Figure B.1: Bent sensing bar at the working site.

To ensure optimal compatibility with the remaining sensing bars and to minimize the introduction of new sources of error, the manufacturing process strictly adhered to the procedures outlined by Oliveira [4]. A bar with identical dimensions as the previous one: an inner diameter of $7\,\mathrm{mm}$, an outer diameter of $10\,\mathrm{mm}$, and a length of approximately $385\,\mathrm{mm}$, was machined at the Laboratório de Técnicas Oficinais (LTO) using a lathe, as displayed in Figure B.2. The same material, aluminum AL 6063-T6, was utilized for the replacement bar. Subsequently, the middle section of the newly fabricated bar was machined to reduce its outer diameter to $9\,\mathrm{mm}$ over a length of approximately $100\,\mathrm{mm}$. This section was designated for the installation of new strain gauges, which were the same as previously installed on the other sensing bars to ensure consistency.

The marking of the strain gauge positions and their bonding onto the new sensing bar are shown in Figures B.3 and B.3.

The wire outputs of the strain gauges were then welded to the same cables the previous sensing bar was connected to and isolated with isolating tape, as shown in Figure B.5

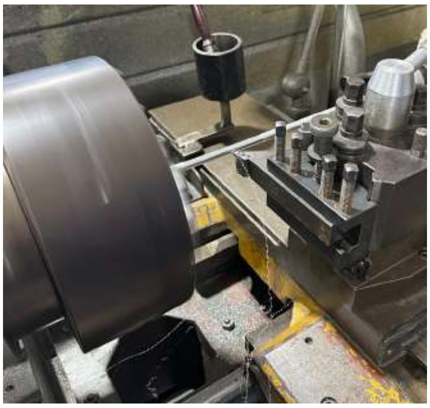

Figure B.2: Machining of the new sensing bar at LTO's lathe.

Figure B.3: Marking of the strain gauge's positions.

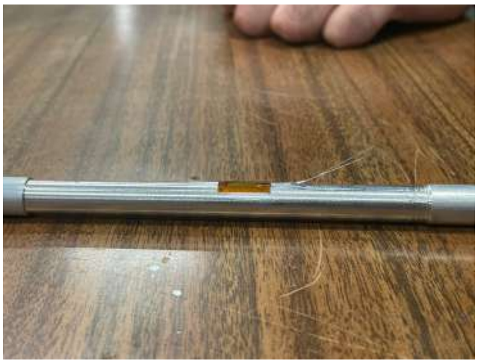

Figure B.4: First strain gauge glued to the new sensing bar.

Figure B.5: Strain gauges welded to the respective cables.

Once manufactured, the new sensing bar underwent individual calibration. This process was carried out by following the procedure described in [4]. Figure B.8 presents the averaged strain response of the sensing bar throughout each loading sequence, and the corresponding linear regression equation and R^2. The calibration procedure involved applying a sequential loading process to the sensing bar while recording the corresponding strain response and the time at which each weight increment is introduced. The predefined load sequence consists of inserting 10N weights up to a total of 70N.

The experimental setup used for this procedure is shown in Figure B.6. It is based on the structure developed by Ferreira [5] for the force balance calibration process, with temporary adaptations to accommodate the calibration of a single sensing bar, as illustrated in Figure B.7.

Figure B.6: Tensile test setup for the bar calibration.

Figure B.7: Loaded tensile test setup.

The averaged strain response for the loading sequence and the resulting linear regression is shown in Figure B.8.

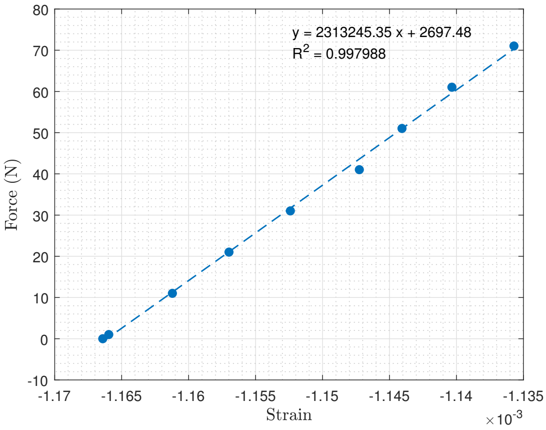

Figure B.8: Force for averaged strain for bar 6.

B.2 Force Balance Calibration

As an additional example, the calibration apparatus configured for a load case of $-F_x$ is shown in Figure B.9.

Figure B.9: Calibration apparatus with $-F_x$ load case ready.

The calibration load cases are shown in Figures B.10 and B.11.

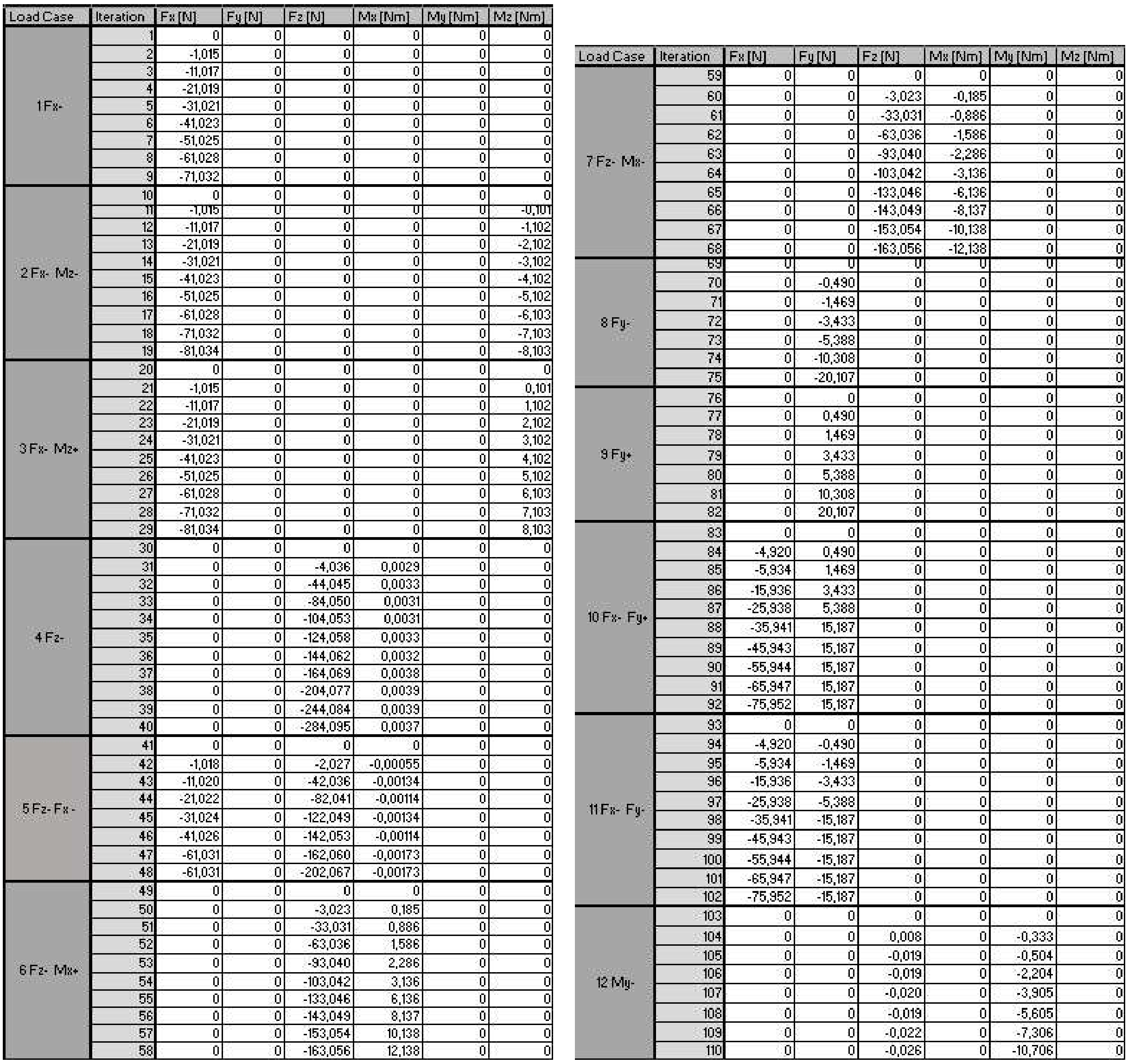

Load Case	Iteration	Fx [N]	Fy [N]	Fz [N]	Mx [Nm]	My [Nm]	Mz [Nm]
1 Fx-	1	0	0	0	0	0	0
	2	-1,015	0	0	0	0	0
	3	-11,017	0	0	0	0	0
	4	-21,019	0	0	0	0	0
	5	-31,021	0	0	0	0	0
	6	-41,023	0	0	0	0	0
	7	-51,025	0	0	0	0	0
	8	-61,028	0	0	0	0	0
	9	-71,032	0	0	0	0	0
2 Fx- Mz-	10	0	0	0	0	0	0
	11	-1,015	0	0	0	0	-0,101
	12	-11,017	0	0	0	0	-1,102
	13	-21,019	0	0	0	0	-2,102
	14	-31,021	0	0	0	0	-3,102
	15	-41,023	0	0	0	0	-4,102
	16	-51,025	0	0	0	0	-5,102
	17	-61,028	0	0	0	0	-6,103
	18	-71,032	0	0	0	0	-7,103
	19	-81,034	0	0	0	0	-8,103
3 Fx- Mz+	20	0	0	0	0	0	0
	21	-1,015	0	0	0	0	0,101
	22	-11,017	0	0	0	0	1,102
	23	-21,019	0	0	0	0	2,102
	24	-31,021	0	0	0	0	3,102
	25	-41,023	0	0	0	0	4,102
	26	-51,025	0	0	0	0	5,102
	27	-61,028	0	0	0	0	6,103
	28	-71,032	0	0	0	0	7,103
	29	-81,034	0	0	0	0	8,103
4 Fz-	30	0	0	0	0	0	0
	31	0	0	-4,036	0,0029	0	0
	32	0	0	-44,045	0,0033	0	0
	33	0	0	-84,050	0,0031	0	0
	34	0	0	-104,053	0,0031	0	0
	35	0	0	-124,058	0,0033	0	0
	36	0	0	-144,062	0,0032	0	0
	37	0	0	-164,069	0,0038	0	0
	38	0	0	-204,077	0,0039	0	0
	39	0	0	-244,084	0,0039	0	0
	40	0	0	-284,095	0,0037	0	0
5 Fz- Fx -	41	0	0	0	0	0	0
	42	-1,018	0	-2,027	-0,00055	0	0
	43	-11,020	0	-42,036	-0,00134	0	0
	44	-21,022	0	-82,041	-0,00114	0	0
	45	-31,024	0	-122,049	-0,00134	0	0
	46	-41,026	0	-142,053	-0,00114	0	0
	47	-61,031	0	-162,060	-0,00173	0	0
	48	-61,031	0	-202,067	-0,00173	0	0
6 Fz- Mx+	49	0	0	0	0	0	0
	50	0	0	-3,023	0,185	0	0
	51	0	0	-33,031	0,886	0	0
	52	0	0	-63,036	1,586	0	0
	53	0	0	-93,040	2,286	0	0
	54	0	0	-103,042	3,136	0	0
	55	0	0	-133,046	6,136	0	0
	56	0	0	-143,049	8,137	0	0
	57	0	0	-153,054	10,138	0	0
	58	0	0	-163,056	12,138	0	0

(a) Load combinations 1-6.

Load Case	Iteration	Fx [N]	Fy [N]	Fz [N]	Mx [Nm]	My [Nm]	Mz [Nm]
7 Fz- Mx-	59	0	0	0	0	0	0
	60	0	0	-3,023	-0,185	0	0
	61	0	0	-33,031	-0,886	0	0
	62	0	0	-63,036	-1,586	0	0
	63	0	0	-93,040	-2,286	0	0
	64	0	0	-103,042	-3,136	0	0
	65	0	0	-133,046	-6,136	0	0
	66	0	0	-143,049	-8,137	0	0
	67	0	0	-153,054	-10,138	0	0
	68	0	0	-163,056	-12,138	0	0
8 Fy-	69	0	0	0	0	0	0
	70	0	-0,490	0	0	0	0
	71	0	-1,469	0	0	0	0
	72	0	-3,433	0	0	0	0
	73	0	-5,388	0	0	0	0
	74	0	-10,308	0	0	0	0
	75	0	-20,107	0	0	0	0
9 Fy+	76	0	0	0	0	0	0
	77	0	0,490	0	0	0	0
	78	0	1,469	0	0	0	0
	79	0	3,433	0	0	0	0
	80	0	5,388	0	0	0	0
	81	0	10,308	0	0	0	0
	82	0	20,107	0	0	0	0
10 Fx- Fy+	83	0	0	0	0	0	0
	84	-4,920	0,490	0	0	0	0
	85	-5,934	1,469	0	0	0	0
	86	-15,936	3,433	0	0	0	0
	87	-25,938	5,388	0	0	0	0
	88	-35,941	15,187	0	0	0	0
	89	-45,943	15,187	0	0	0	0
	90	-55,944	15,187	0	0	0	0
	91	-65,947	15,187	0	0	0	0
	92	-75,952	15,187	0	0	0	0
11 Fx- Fy-	93	0	0	0	0	0	0
	94	-4,920	-0,490	0	0	0	0
	95	-5,934	-1,469	0	0	0	0
	96	-15,936	-3,433	0	0	0	0
	97	-25,938	-5,388	0	0	0	0
	98	-35,941	-15,187	0	0	0	0
	99	-45,943	-15,187	0	0	0	0
	100	-55,944	-15,187	0	0	0	0
	101	-65,947	-15,187	0	0	0	0
	102	-75,952	-15,187	0	0	0	0
12 My-	103	0	0	0	0	0	0
	104	0	0	0,008	0	-0,333	0
	105	0	0	-0,019	0	-0,504	0
	106	0	0	-0,019	0	-2,204	0
	107	0	0	-0,020	0	-3,905	0
	108	0	0	-0,019	0	-5,605	0
	109	0	0	-0,022	0	-7,306	0
	110	0	0	-0,026	0	-10,706	0

(b) Load combinations 7-12.

Figure B.10: Force balance calibrations load combinations 1-13.

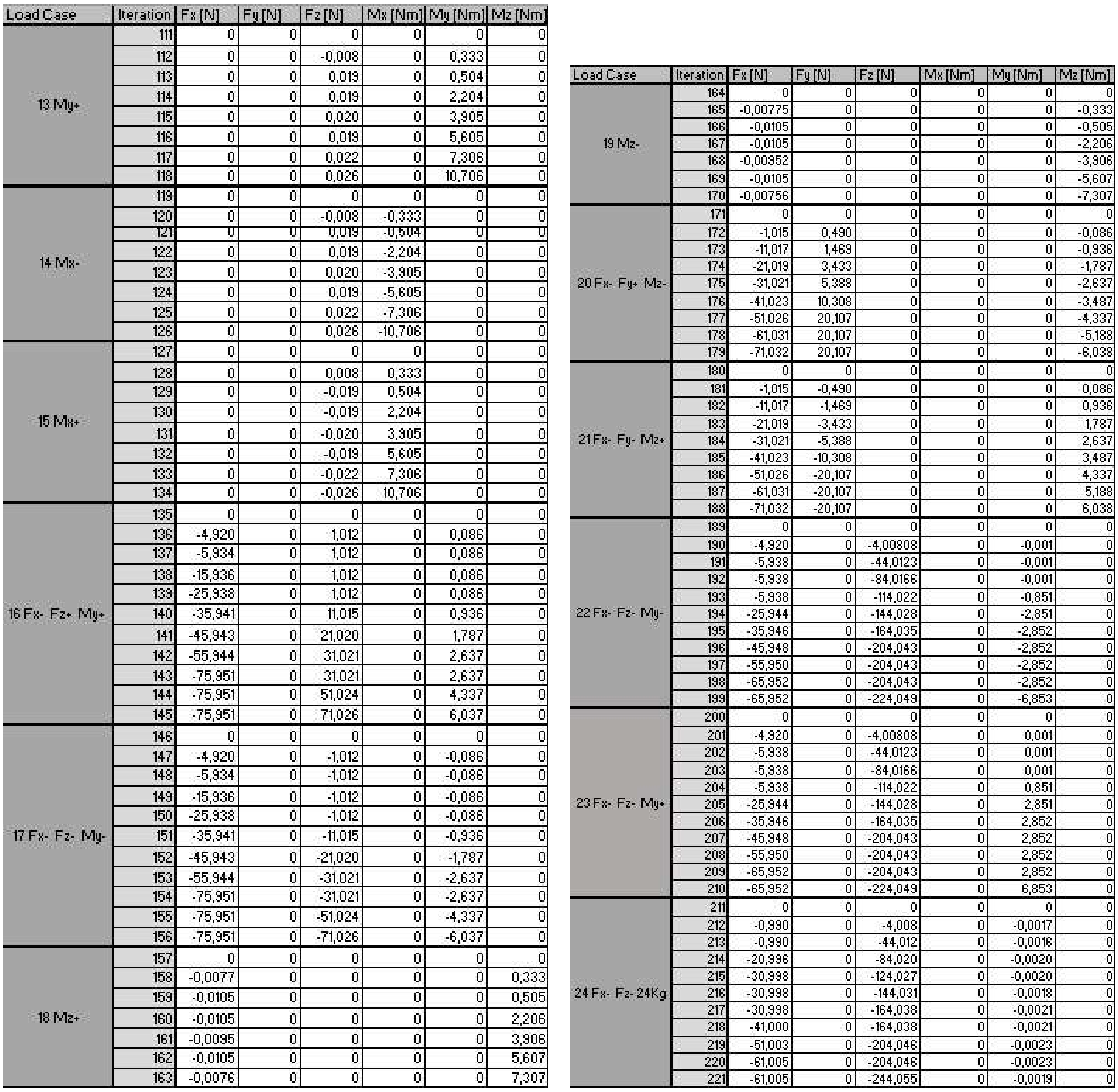

Load Case	Iteration	Fx [N]	Fy [N]	Fz [N]	Mx [Nm]	My [Nm]	Mz [Nm]
13 My+	111	0	0	0	0	0	0
	112	0	0	-0,008	0	0,333	0
	113	0	0	0,019	0	0,504	0
	114	0	0	0,019	0	2,204	0
	115	0	0	0,020	0	3,905	0
	116	0	0	0,019	0	5,605	0
	117	0	0	0,022	0	7,306	0
	118	0	0	0,026	0	10,706	0
14 Mx-	119	0	0	0	0	0	0
	120	0	0	-0,008	-0,333	0	0
	121	0	0	0,019	-0,504	0	0
	122	0	0	0,019	-2,204	0	0
	123	0	0	0,020	-3,905	0	0
	124	0	0	0,019	-5,605	0	0
	125	0	0	0,022	-7,306	0	0
	126	0	0	0,026	-10,706	0	0
15 Mx+	127	0	0	0	0	0	0
	128	0	0	0,008	0,333	0	0
	129	0	0	-0,019	0,504	0	0
	130	0	0	-0,019	2,204	0	0
	131	0	0	-0,020	3,905	0	0
	132	0	0	-0,019	5,605	0	0
	133	0	0	-0,022	7,306	0	0
	134	0	0	-0,026	10,706	0	0
16 Fx- Fz+ My+	135	0	0	0	0	0	0
	136	-4,920	0	1,012	0	0,086	0
	137	-5,934	0	1,012	0	0,086	0
	138	-15,936	0	1,012	0	0,086	0
	139	-25,938	0	1,012	0	0,086	0
	140	-35,941	0	11,015	0	0,936	0
	141	-45,943	0	21,020	0	1,787	0
	142	-55,944	0	31,021	0	2,637	0
	143	-75,951	0	31,021	0	2,637	0
	144	-75,951	0	51,024	0	4,337	0
	145	-75,951	0	71,026	0	6,037	0
17 Fx- Fz- My-	146	0	0	0	0	0	0
	147	-4,920	0	-1,012	0	-0,086	0
	148	-5,934	0	-1,012	0	-0,086	0
	149	-15,936	0	-1,012	0	-0,086	0
	150	-25,938	0	-1,012	0	-0,086	0
	151	-35,941	0	-11,015	0	-0,936	0
	152	-45,943	0	-21,020	0	-1,787	0
	153	-55,944	0	-31,021	0	-2,637	0
	154	-75,951	0	-31,021	0	-2,637	0
	155	-75,951	0	-51,024	0	-4,337	0
	156	-75,951	0	-71,026	0	-6,037	0
18 Mz+	157	0	0	0	0	0	0
	158	-0,0077	0	0	0	0	0,333
	159	-0,0105	0	0	0	0	0,505
	160	-0,0105	0	0	0	0	2,206
	161	-0,0095	0	0	0	0	3,906
	162	-0,0105	0	0	0	0	5,607
	163	-0,0076	0	0	0	0	7,307

(a) Load combinations 13-18.

Load Case	Iteration	Fx [N]	Fy [N]	Fz [N]	Mx [Nm]	My [Nm]	Mz [Nm]
19 Mz-	164	0	0	0	0	0	0
	165	-0,00775	0	0	0	0	-0,333
	166	-0,0105	0	0	0	0	-0,505
	167	-0,0105	0	0	0	0	-2,206
	168	-0,00952	0	0	0	0	-3,906
	169	-0,0105	0	0	0	0	-5,607
	170	-0,00756	0	0	0	0	-7,307
20 Fx- Fy+ Mz-	171	0	0	0	0	0	0
	172	-1,015	0,490	0	0	0	-0,086
	173	-11,017	1,469	0	0	0	-0,936
	174	-21,019	3,433	0	0	0	-1,787
	175	-31,021	5,388	0	0	0	-2,637
	176	-41,023	10,308	0	0	0	-3,487
	177	-51,026	20,107	0	0	0	-4,337
	178	-61,031	20,107	0	0	0	-5,188
	179	-71,032	20,107	0	0	0	-6,038
21 Fx- Fy- Mz+	180	0	0	0	0	0	0
	181	-1,015	-0,490	0	0	0	0,086
	182	-11,017	-1,469	0	0	0	0,936
	183	-21,019	-3,433	0	0	0	1,787
	184	-31,021	-5,388	0	0	0	2,637
	185	-41,023	-10,308	0	0	0	3,487
	186	-51,026	-20,107	0	0	0	4,337
	187	-61,031	-20,107	0	0	0	5,188
	188	-71,032	-20,107	0	0	0	6,038
22 Fx- Fz- My-	189	0	0	0	0	0	0
	190	-4,920	0	-4,00808	0	-0,001	0
	191	-5,938	0	-44,0123	0	-0,001	0
	192	-5,938	0	-84,0166	0	-0,001	0
	193	-5,938	0	-114,022	0	-0,851	0
	194	-25,944	0	-144,028	0	-2,851	0
	195	-35,946	0	-164,035	0	-2,852	0
	196	-45,948	0	-204,043	0	-2,852	0
	197	-55,950	0	-204,043	0	-2,852	0
	198	-65,952	0	-204,043	0	-2,852	0
	199	-65,952	0	-224,049	0	-6,853	0
23 Fx- Fz- My+	200	0	0	0	0	0	0
	201	-4,920	0	-4,00808	0	0,001	0
	202	-5,938	0	-44,0123	0	0,001	0
	203	-5,938	0	-84,0166	0	0,001	0
	204	-5,938	0	-114,022	0	0,851	0
	205	-25,944	0	-144,028	0	2,851	0
	206	-35,946	0	-164,035	0	2,852	0
	207	-45,948	0	-204,043	0	2,852	0
	208	-55,950	0	-204,043	0	2,852	0
	209	-65,952	0	-204,043	0	2,852	0
	210	-65,952	0	-224,049	0	6,853	0
24 Fx- Fz- 24Kg	211	0	0	0	0	0	0
	212	-0,990	0	-4,008	0	-0,0017	0
	213	-0,990	0	-44,012	0	-0,0016	0
	214	-20,996	0	-84,020	0	-0,0020	0
	215	-30,998	0	-124,027	0	-0,0020	0
	216	-30,998	0	-144,031	0	-0,0018	0
	217	-30,998	0	-164,038	0	-0,0021	0
	218	-41,000	0	-164,038	0	-0,0021	0
	219	-51,003	0	-204,046	0	-0,0023	0
	220	-61,005	0	-204,046	0	-0,0023	0
	221	-61,005	0	-244,055	0	-0,0019	0

(b) Load combinations 19-24.

Figure B.11: Force balance calibrations load combinations 14-24.

The correlation between the resultant forces, $R = (F_x, F_y, F_z, M_x, M_y, M_z)$, and the corresponding relative axial forces measured by each bar, $(r_1, r_2, r_3, r_4, r_5, r_6)$, is presented in Figure B.12.

$$\begin{bmatrix} F_x \\ F_y \\ F_z \\ M_x \\ M_y \\ M_z \end{bmatrix} = \mathbf{C} \begin{bmatrix} r_1 \\ r_2 \\ r_3 \\ r_4 \\ r_5 \\ r_6 \\ r_1^2 \\ r_1 r_2 \\ r_1 r_3 \\ r_1 r_4 \\ r_1 r_5 \\ r_1 r_6 \\ r_2^2 \\ r_2 r_3 \\ r_2 r_4 \\ r_2 r_5 \\ r_2 r_6 \\ r_3^2 \\ r_3 r_4 \\ r_3 r_5 \\ r_3 r_6 \\ r_4^2 \\ r_4 r_5 \\ r_4 r_6 \\ r_5^2 \\ r_5 r_6 \\ r_6^2 \end{bmatrix}, \quad \mathbf{C} = \begin{bmatrix} -9.54748 & -188.43402 & 193.88032 & -77.72369 & 34.45458 & 66.64144 \\ -119.49161 & -130.82218 & 97.14037 & -57.70082 & 48.21079 & 10.86865 \\ 60.85149 & 324.07248 & -277.87112 & 120.02427 & -46.14358 & -48.45382 \\ -9.73543 & 566.53305 & -888.74097 & 197.95739 & -15.06601 & -92.17297 \\ 5.14175 & -315.30584 & 484.71008 & -107.29063 & 0.09060 & 37.13057 \\ 68.26577 & -33.92526 & 65.25263 & 9.80697 & -38.46279 & -32.38469 \\ 0.00444 & 0.03201 & -0.03982 & 0.01193 & -0.00522 & -0.00719 \\ 0.00171 & 0.02463 & -0.05116 & 0.00927 & -0.00080 & -0.00031 \\ 0.01214 & -0.05041 & 0.09134 & -0.01652 & -0.00033 & 0.00480 \\ 0.01507 & -0.06889 & 0.15900 & -0.01609 & -0.01899 & -0.01324 \\ -0.02012 & 0.05425 & -0.11424 & 0.01466 & 0.01336 & 0.00382 \\ -0.01331 & -0.03096 & 0.03507 & -0.01328 & 0.00711 & 0.00610 \\ 0.00153 & 0.00582 & -0.00033 & 0.00080 & 0.00070 & 0.00247 \\ 0.00063 & 0.00964 & -0.01810 & 0.00571 & -0.00080 & -0.00378 \\ 0.05413 & 0.04204 & 0.02469 & 0.01491 & -0.02327 & -0.00315 \\ -0.01015 & -0.02157 & 0.01125 & -0.00655 & 0.00480 & 0.00126 \\ -0.01070 & -0.03658 & 0.03867 & -0.01228 & 0.00279 & -0.00209 \\ -0.01762 & -0.01815 & -0.00100 & -0.00837 & 0.00463 & 0.00090 \\ -0.04712 & -0.03813 & -0.05173 & -0.02035 & 0.03194 & 0.02358 \\ 0.02768 & 0.00426 & 0.03018 & 0.00583 & -0.01554 & -0.00972 \\ 0.00757 & 0.05696 & -0.04667 & 0.01876 & -0.00414 & -0.00036 \\ -0.05223 & -0.15836 & 0.17751 & -0.05217 & 0.02129 & 0.01641 \\ 0.05555 & 0.12973 & -0.11933 & 0.04097 & -0.02003 & -0.00934 \\ 0.00296 & 0.07411 & -0.14668 & 0.02023 & 0.00978 & 0.00836 \\ -0.01240 & -0.02647 & 0.02202 & -0.00790 & 0.00393 & 0.00104 \\ -0.01088 & -0.03033 & 0.05317 & -0.01010 & -0.00022 & -0.00165 \\ 0.00958 & 0.00052 & 0.00449 & 0.00209 & -0.00433 & -0.00212 \end{bmatrix}$$

Figure B.12: Force balance coefficient matrix $\mathbf{C}$.

Appendix C

Wind Tunnel Testing

C.1 Formula Student Scaled Model

The pressure tap layout followed the coordinate mapping presented in Table C.1.

Table C.1: Pressure tap position layout including chordwise positions and corresponding spanwise locations expressed as a percentage of the car half width, w.

Spanwise	y (mm)	$\lvert y\rvert/(w/2)$ $(\%)$
y_1	89	38
y_2	117	49
y_3	-102	43
y_4	-129	55
Chordwise x/c $(\%)$: 5, 15, 30, 50, 65, 80		

Regarding the mounting system of the scaled FS car model to the force balance employed in this study, a $4\ \mathrm{mm}$ thick aluminum sheet was installed on the interior surface of the lower part of the monocoque. The sheet was shaped to occupy as much of the available area as possible in this region. Its purpose is to distribute the applied loads and prevent the local model material from being crushed. This sheet is secured to the model using four M6 fasteners. Next, two extruded aluminum L-shaped brackets were positioned on either side of the intended support arm location inside the monocoque. Each bracket is fastened on top of the aluminum sheet with a single M6 fastener. The balance support arm then passes through an opening in the bottom portion of the monocoque. After the attachment is completed, this opening is filled with additional parts to minimize flow disturbance. Finally, the support arm, the two brackets, and an insert are clamped together with a single M8 bolt. To further strengthen the assembly, the insert was made with a material reinforced with carbon fiber to prevent deformation of the support arm tabs when tightening. Additionally, transparent tape was applied to the wind tunnel floor to seal the gap created by the opening through which the support arm enters the test section, ensuring that no further leakage disturbs the flow during testing. Figure C.1 illustrates the designed mounting system and its corresponding components.

Figure C.1: Model attachment feature.

Since the attachment point of the model to the balance support arm is expected to be located at its pressure center, while high aerodynamic loads are expected at both ends of the model, the monocoque would be subjected to significant bending loads. To address this, additional tab components reinforced with carbon fiber were introduced between each section of the monocoque. This design resulted in four extra reinforcement parts, ensuring the structural integrity of the model under the expected loading conditions.

Regarding the adjustability of the car model, this was achieved by inserting $2\ \mathrm{mm}$ thick large washers beneath the L-shaped brackets on top of the aluminum sheet, thereby increasing the ground clearance by $2\ \mathrm{mm}$ each time when applied symmetrically on both sides of the mounting system. This feature is actually shown in Figure C.1, where two washers were inserted per side. When washers are applied asymmetrically, the model's pitch can also be adjusted, although this option is not recommended and should only be used when strictly necessary. It is important to note that the mounting system reuses the existing support arm from [4], which originally included a pitch control component at its top tip. However, this part was removed in the present setup to allow the mounting system to be inside the model.

Concerning the printing settings and their consistency, all components belonging to the same assembly were printed using identical parameters, for example, the different parts of the front wing or the side diffuser. The first set of prints focused on the front wing assembly, with the initial trials serving to test and define printing parameters by evaluating surface quality, stiffness, and production time, as well as verifying fitting tolerances. For instance, the aerodynamic package was printed with an emphasis on achieving a smooth surface finish while maintaining adequate stiffness. Nonetheless, each aerodynamic assembly required slightly different settings, primarily due to varying structural requirements and geometrical characteristics. Table C.2 presents an average for the printing parameters used for most of the components and also specifically for the different sections of the monocoque, provided here as two representative examples.

Relating to fitting tests, several surface offset values were explored during the initial trials. Ultimately, an offset of $0.15\ \mathrm{mm}$ was selected for inserting threaded rods into printed components, as well as for holes designed to accommodate fasteners with nominal diameters. An offset of $0.3\ \mathrm{mm}$ was adopted for connections mainly involving the aluminum suspension arms with the respective connectors. Additionally, an offset of $0.2\ \mathrm{mm}$ was defined for cases where two printed parts were to be slotted together or for boss-pocket fittings. These boss-pocket fittings constituted the primary connection mechanism between sections of the same assemblies, such as the monocoque segments, the front wing elements, or the rear wing sections.

Figure C.2: Rear wing assembly test.

Some of the printing parameters used in the manufacturing of the FST14 scaled model are presented in Table C.2.

Table C.2: 3D printing settings.

Print settings	Aero	Mono
Quality		
Layer height	0.12 mm	0.24 mm
Initial layer height	0.20 mm	0.30 mm
Wall line width	0.42 mm	0.42 mm
Infill line width	0.45 mm	0.45 mm
Walls		
Wall line count	4	4
Top/Bottom		
Top and bottom layers	5	4
Infill		
Type	Gyroid	Gyroid
Sparse density	25%	20%
Support		
Structure	Tree	Tree
Brim line count	10	10
Support interface	Enable	Enable
Support roof	Enable	Enable
Top distance	0.10 mm	0.10 mm
Z distance	0.10 mm	0.10 mm
Travel		
Avoid supports	Enable	Enable
Build plate adhesion		
Type	Brim	Brim
Brim line count	10	15